La Rivista del Nuovo Cimento (2023) 46:619–692
https://doi.org/10.1007/s40766-023-00049-2

REVIEW PAPER

The search for neutrinoless double-beta decay

Juan José Gómez-Cadenas[1,2] · Justo Martín-Albo[3] · Javier Menéndez[4,5] · Mauro Mezzetto[6] · Francesc Monrabal[1,2] · Michel Sorel[3]

Received: 1 September 2023 / Accepted: 7 October 2023 / Published online: 9 January 2024
© The Author(s) 2023

This article is a revised version of https://doi.org/10.1393/ncr/i2012-10074-9.

Change summary Major revision, updated and expanded.

Change details The paper follows closely the structure of the 2012 review, with the same sections: Introduction, Massive Neutrinos, Neutrinoless Double Beta Decay, Nuclear Matrix elements, Ingredients for bb0nu experiments, Neutrinoless Double Beta Decay experiments and conclusions. This update includes:
1. A full revision of the text, using a more consistent notation and updating many figures to make them more precise or attractive.
2. A full update of all experimental results.
3. The chapter on NMEs have been written from scratch (this is the contribution of our new author, Javier Menéndez).
4. The chapter on "ingredients" have been largely re-written.
5. The chapter on experiments includes all new results and projected results from major collaborations.
6. The introduction and conclusions have been updated.
The introduction (Sect. 1) has been updated to reflect the progress in the field during the last decade. In particular, it includes references to all the new major results of the last 10 years.
Sections 2 and 3 have been updated primarily to reflect the recent experimental progress in neutrino flavour oscillation results, cosmic microwave background and galaxy survey data, direct searches for neutrino mass and lepton number violating processes, and finally in double beta decay results. Several particle physics theory concepts have also been clarified.
Section 4 has been almost completely re-written and, in addition to update the main results of conventional models, now discusses recent nuclear theory advances like the short-range contribution to the neutrinoless doble-beta decay nuclear matrix element and ab initio nuclear many-body calculations of beta and double-beta decay matrix elements.
Section 5 has been updated with the objective of explaining in a more didactic way the impact of different parameters to the bb experiments sensitivity. The discussion on background sources and mitigation have been extended. Finally, most of the plots have been updated to the recent landscape with also improved quality.
Section 6 has been entirely rewritten and now briefly reviews the main experimental efforts towards the exploration of neutrinoless double beta decay half-lives up to 1.E28 years.
Section 7 has been updated to reflect progress in the last decade.

✉ Juan José Gómez-Cadenas
jjgomezcadenas@dipc.org

Extended author information available on the last page of the article

Abstract

Neutrinos are the only particles in the Standard Model that could be Majorana fermions, that is, completely neutral fermions that are their own antiparticles. The most sensitive known experimental method to verify whether neutrinos are Majorana particles is the search for neutrinoless double-beta decay. The last 2 decades have witnessed the development of a vigorous program of neutrinoless double-beta decay experiments, spanning several isotopes and developing different strategies to handle the backgrounds masking a possible signal. In addition, remarkable progress has been made in the understanding of the nuclear matrix elements of neutrinoless double-beta decay, thus reducing a substantial part of the theoretical uncertainties affecting the particle–physics interpretation of the process. On the other hand, the negative results by several experiments, combined with the hints that the neutrino mass ordering could be normal, may imply very long lifetimes for the neutrinoless double-beta decay process. In this report, we review the main aspects of such process, the recent progress on theoretical ideas and the experimental state of the art. We then consider the experimental challenges to be addressed to increase the sensitivity to detect the process in the likely case that lifetimes are much longer than currently explored, and discuss a selection of the most promising experimental efforts.

Keywords Neutrinos · Majorana · Double-beta decay · Nuclear matrix elements

Contents

1 Introduction . . . 621
2 Massive neutrinos . . . 623
  2.1 Current knowledge of neutrino mass and mixing . . . 623
  2.2 The origin of neutrino mass: Dirac versus Majorana neutrinos . . . 627
  2.3 The see-saw mechanism . . . 631
  2.4 Leptogenesis . . . 634
  2.5 Lepton number violating processes . . . 635
3 Neutrinoless double-beta decay . . . 636
  3.1 Double-beta decay modes . . . 636
  3.2 The black box theorem . . . 641
  3.3 The standard neutrinoless double-beta decay mechanism: light Majorana neutrino exchange . 642
  3.4 Alternative neutrinoless double-beta decay mechanisms . . . 644
4 Nuclear matrix elements . . . 646
  4.1 Nuclear matrix elements: long- and short-range parts . . . 646
    4.1.1 Long-range nuclear matrix elements . . . 649
    4.1.2 Short-range nuclear matrix elements . . . 650
  4.2 Different nuclear structure approaches . . . 652
    4.2.1 Tests of nuclear structure calculations and g_A quenching . . . 652
    4.2.2 Ab initio methods . . . 653
    4.2.3 Many-body approaches for heavy nuclei . . . 654
  4.3 Nuclear matrix elements with theoretical uncertainties . . . 656
5 Ingredients for $\beta\beta0\nu$-decay experiments . . . 657
  5.1 Background sources . . . 659
  5.2 Background mitigation . . . 661
  5.3 Sensitivity of a $\beta\beta0\nu$ experiment . . . 663
    5.3.1 Minimizing υ_1: molar mass, $Q_{\beta\beta}$ and NMEs . . . 664
    5.3.2 Minimizing υ_2: isotope mass . . . 666

    5.3.3 Minimizing υ_2: energy resolution 666
    5.3.4 Minimizing υ_2: background index 666
    5.3.5 Detection efficiency 668
6 The past, present, and future of $\beta\beta0\nu$-decay searches 668
  6.1 High-purity germanium detectors 669
  6.2 Bolometers 671
  6.3 Xenon time projection chambers 673
  6.4 Loaded liquid scintillator 676
7 Conclusions 677
References 680

1 Introduction

Double-beta ($\beta\beta$) decay is a very rare nuclear transition in which a nucleus with Z protons decays into a nucleus with $Z + 2$ protons and the same mass number A. The decay can occur only if the mass of the initial nucleus is larger than the one of the final nucleus, and the transition to the $Z + 1$ state is forbidden or highly suppressed. There are 35 naturally occurring isotopes that can undergo $\beta\beta$. Two decay modes are usually considered: (i) the standard two-neutrino mode ($\beta\beta2\nu$), consisting of two simultaneous beta decays, ${}^{\mathrm{A}}_{\mathrm{Z}}\mathrm{X} \rightarrow {}^{\mathrm{A}}_{\mathrm{Z+2}}\mathrm{X}' + 2\,e^- + 2\,\overline{\nu}$, which has been observed in several isotopes with typical half-lives in the range of 10^{18}–10^{21} years; and (ii) the neutrinoless mode ($\beta\beta0\nu$), ${}^{\mathrm{A}}_{\mathrm{Z}}\mathrm{X} \rightarrow {}^{\mathrm{A}}_{\mathrm{Z+2}}\mathrm{X}' + 2\,e^-$, a hypothetical rare decay, which violates lepton-number conservation, and is, therefore, forbidden in the Standard Model (SM).

The $\beta\beta0\nu$ process cannot occur unless neutrinos are Majorana particles. If ν is a field describing a neutrino, stating that the neutrino is a Majorana particle is equivalent to saying that the charge-conjugated field (that is, a field with all charges reversed) also describes the same particle: $\nu \equiv \nu^c$. If such Majorana condition is not fulfilled, we speak instead of Dirac neutrinos.

The theoretical implications of experimentally establishing $\beta\beta0\nu$ decay would, therefore, be profound. In a broad sense, Majorana neutrinos would constitute a new form of matter, given that no Majorana elementary fermions have been observed so far.[1] Also, the observation of $\beta\beta0\nu$ decay would prove that total lepton number is not conserved in physical phenomena, a fact that could be linked to the cosmic asymmetry between matter and antimatter. Finally, Majorana neutrinos would mean that a new physics scale must exist and is accessible in an indirect way through neutrino masses.

In addition to theoretical prejudice in favor of Majorana neutrinos, there are other reasons to hope that experimental observation of $\beta\beta0\nu$ decay is at hand. Neutrinos are now known to be massive particles thanks to neutrino oscillation experiments. If $\beta\beta0\nu$ decay is mediated by the standard light Majorana neutrino exchange mechanism, a non-zero neutrino mass would almost certainly translate into a non-zero $\beta\beta0\nu$ rate. While neutrino oscillation phenomenology is not enough *per se* to provide a firm prediction for what such a rate should be, it does give us hope that a sufficiently fast one to be observable may be realized in nature.

The importance of massive Majorana neutrinos has triggered a new generation of $\beta\beta0\nu$-decay experiments spanning several isotopes and a rich selection of experimental techniques. Five of them have published lower limits[2] on the half-life of the $\beta\beta0\nu$ process ($T^{0\nu}_{1/2}$) that exceed 10^{25} years, increasing the sensitivity of previous experiments by at least an order of magnitude. GERDA[3] and the Majorana Demonstrator[4] (source isotope ^{76}Ge) found $T^{0\nu}_{1/2} > 1.8 \times 10^{26}$ yr [2] and $T^{0\nu}_{1/2} > 8.3 \times 10^{25}$ yr [3], respectively; CUORE[5] (source isotope ^{130}Te) obtained $T^{0\nu}_{1/2} > 2.2 \times 10^{25}$ yr [4]; EXO-200[6] and KamLAND-Zen[7] (source isotope ^{136}Xe) set limits of $T^{0\nu}_{1/2} > 3.5 \times 10^{25}$ yr [5] and $T^{0\nu}_{1/2} > 2.3 \times 10^{26}$ yr [6], respectively.

---

[1] Majorana-like collective excitations have instead been observed in certain superconducting materials [1].

In addition, the CUPID demonstrators proved the feasibility of scintillating bolometer detectors, which are currently envisioned as the successors of conventional bolometers (such as those used by CUORE) and have set lower limits to the $\beta\beta0\nu$ process for two relevant isotopes. For ^{100}Mo, CUPID-Mo set a limit of $T^{0\nu}_{1/2} > 1.8 \times 10^{24}$ yr [7], and for ^{82}Se, CUPID-0 found $T^{0\nu}_{1/2} > 4.6 \times 10^{24}$ yr [8].

Also, during the last five years, NEXT[8] has successfully demonstrated, through the operation of the NEXT-White demonstrator, the suitability for $\beta\beta0\nu$-decay searches of the technology based on electroluminescent high-pressure xenon gas chambers (HPXeEL). In spite of the small mass of NEXT-White (3.5 kg of ^{136}Xe in the fiducial region), the detector has carried out a search for $\beta\beta0\nu$ events, setting a limit of $T^{0\nu}_{1/2} > 1.3 \times 10^{24}$ yr [9]. NEXT-100, currently under commissioning at the Laboratorio Subterráneo de Canfranc (LSC), deploys a much larger mass of ^{136}Xe and will reach a sensitivity comparable to that of EXO-200.

It is important to remark that, in spite of the much increased sensitivity of the experiments discussed above, the resulting limits on the effective neutrino mass (see Sect. 3 for a detailed discussion) are relatively modest. For example, the limit set by GERDA translates into $m_{\beta\beta} < 79$–180 meV. The push to explore smaller neutrino masses has resulted in a major experimental effort to build detectors which will deploy, typically, one order of magnitude larger masses than their previous incarnations, while, at the same time, reducing the background in the region of interest (ROI) by the same amount. In the process, GERDA and the Majorana Demonstrator have joined into a single collaboration, LEGEND,[9] whose first phase, LEGEND-200, has already started data taking. CUORE has mutated into CUPID,[10] EXO-200 has inspired the nEXO[11] proposal, which aims to scale up the LXe technology from about 200 kg to 5 tons, and the NEXT collaboration intends to follow up NEXT-100 with NEXT-HD, a ton-scale HPXeEL, and is actively researching the possibility to build a detector (dubbed NEXT-BOLD) capable of detecting the single Ba^{2+} ion emitted in the decay as a mean to drastically suppress backgrounds. Also, the large scintillating calorimeters, KamLAND-Zen and SNO+,[12] are proposing upgrades that are both larger and able to control the background better. In addition, a host of R&D proposals is being developed (see, for example, [10] and references therein).

---

[2] Unless otherwise stated, all limits in this review are at 90% CL.

[3] https://www.mpi-hd.mpg.de/gerda/.

[4] https://sanfordlab.org/experiment/majorana-demonstrator.

[5] https://cuore.lngs.infn.it/en.

[6] https://www-project.slac.stanford.edu/exo/.

[7] https://www.ipmu.jp/en/research-activities/research-program/kamland.

[8] https://next.ific.uv.es/next/.

[9] https://legend-exp.org.

[10] https://www.lngs.infn.it/en/pages/cupid-en.

[11] https://nexo.llnl.gov.

Here, we review the state of the art of this exciting and rapidly changing field. The organization of the paper is as follows. The introductory material is covered in Sects. 2 and 3. The key particle physics concepts involving massive Majorana neutrinos and neutrinoless double-beta decay are laid out here. The current experimental knowledge on neutrino masses, lepton number violating processes in general, and $\beta\beta0\nu$ in particular, is also described in Sects. 2 and 3. Sections 4–6 cover more advanced topics. The theoretical aspects of the nuclear physics of $\beta\beta0\nu$ are discussed in Sect. 4. Sections 5 and 6 deal with experimental aspects of $\beta\beta0\nu$, and can be read without knowledge of Sect. 4. An attempt at a pedagogical discussion of experimental ingredients affecting $\beta\beta0\nu$ searches is made in Sect. 5. Section 6 adds a description of selected past, present, and future experiments.

2 Massive neutrinos

2.1 Current knowledge of neutrino mass and mixing

Neutrinos are the lightest known elementary fermions. They do not carry electric or color charge, and are observable only via weak interactions. In the Standard Model of elementary particles, neutrinos are paired with charged leptons in weak isodoublets. Experimentally, we know that only three light—that is, of mass smaller than $m_Z/2$, where m_Z is the mass of the Z boson—*active* neutrino families exist.

Neutrino oscillation experiments at the turn of the millennium unambiguously demonstrated that neutrinos are massive particles [11–13]. Because of the interferometric nature of neutrino oscillations, such experiments can only measure squared-mass differences and not the absolute neutrino mass scale. Solar and reactor experiments have measured one mass difference, the so-called *solar mass splitting*, to be: $\Delta m^2_{21} \equiv m^2_2 - m^2_1 = (7.41^{+0.21}_{-0.20}) \times 10^{-5}\ \mathrm{eV}^2$. Atmospheric and accelerator-based experiments have measured a different mass splitting, the so-called *atmospheric mass splitting*, to be: $|\Delta m^2_{31}| \equiv |m^2_3 - m^2_1| = (2.511^{+0.028}_{-0.027}) \times 10^{-3}\ \mathrm{eV}^2 \gg \Delta m^2_{21}$. In the standard three-neutrino paradigm, those are the only two independent mass splittings available. The best-fit values and 1σ ranges quoted above were obtained from a recent global three-neutrino fit [14]. Similar results are obtained in other global analyses [15, 16].

The observation of neutrino flavor oscillations also implies that the neutrino states participating in the weak interactions (*flavor eigenstates*) are different from the neutrino states controlling free particle evolution (*mass eigenstates*). In other words, the three weak eigenstates $|\nu_\alpha\rangle,\ \alpha = e, \mu, \tau$, can be expressed as a linear combination of the three mass eigenstates $|\nu_i\rangle,\ i = 1, 2, 3$

---

[12] https://snoplus.phy.queensu.ca.

$$|\nu_\alpha\rangle = \sum_i U^*_{\alpha i} |\nu_i\rangle, \tag{1}$$

where U is a 3×3 unitary *neutrino mixing matrix* different from unity. Equation (1) implies the violation of the individual lepton flavors L_α, but not necessarily the violation of the total lepton number $L \equiv \sum_\alpha L_\alpha = L_e + L_\mu + L_\tau$. The neutrino mixing matrix is usually parametrized in terms of 3 Euler angles $(\theta_{12},\ \theta_{13},\ \theta_{23})$ and 3 phases $(\delta,\ \alpha_{21},\ \alpha_{31})$; see, for example, [17]. If the massive neutrinos are *Dirac particles* (see Sect. 2.2), only the *Dirac phase* δ is physical and can be responsible for CP violation in the lepton sector. If the massive neutrinos are *Majorana particles* (Sect. 2.2), the two additional *Majorana phases* $(\alpha_{21},\ \alpha_{31})$ are also potentially observable.

Neutrino oscillation experiments have measured with few-percent level accuracy the flavor content of the neutrino mass states participating in neutrino mixing. Atmospheric and accelerator-based neutrino oscillation experiments are mostly driven by $\nu_\mu \to \nu_\tau$ oscillations, with a sub-leading yet well-established $\nu_\mu \to \nu_e$ oscillation component. They have, therefore, measured the muon and tau flavor contents of the ν_3 mass state to be large and similar among them $(|U_{\mu 3}|^2 \simeq |U_{\tau 3}|^2 \simeq 0.5)$, and that such mass state has little electron flavor content $(|U_{e3}|^2 \simeq 0.02)$. On the other hand, solar and reactor neutrino oscillation experiments are consistent with $\nu_e \to \nu_\mu$ and $\nu_e \to \nu_\tau$ transitions. They have measured $|U_{e2}|^2 \simeq 0.3$. The remaining elements of the leptonic mixing matrix can be derived assuming unitarity. More precisely, according to [14], the 3σ ranges in the magnitude of the elements of the three-flavor leptonic mixing matrix under the assumption that the matrix U is unitary are the following:

$$|U|_{3\sigma} = \begin{pmatrix} 0.803 \to 0.845 & 0.514 \to 0.578 & 0.143 \to 0.155 \\ 0.244 \to 0.498 & 0.502 \to 0.693 & 0.632 \to 0.768 \\ 0.272 \to 0.517 & 0.473 \to 0.672 & 0.623 \to 0.761 \end{pmatrix}. \tag{2}$$

The three outstanding unknowns of the three-neutrino mixing framework that are potentially observable in the current and future neutrino oscillation experiments are: the neutrino mass ordering ($m_3 > m_1$ or vice versa), the dominant flavor of the ν_3 state ($|U_{\mu 3}|^2 > |U_{\tau 3}|^2$, or vice versa[13]), and whether CP violation is violated in the neutrino sector ($\delta \neq 0, \pi$ or not).

Concerning the neutrino mass ordering, current neutrino oscillation results cannot yet differentiate between two possibilities, usually referred to as *normal* and *inverted orderings*. In the former, the gap between the two lightest mass eigenstates corresponds to the small mass difference (Δm^2_{21}), while in the second case, the gap between the two lightest states corresponds to the large mass difference (Δm^2_{31}). While we do not know at present whether ν_3 is heavier or lighter than ν_1, we do know that ν_2 is heavier than ν_1, thanks to matter effects affecting the propagation of neutrinos inside the Sun. The exploitation of the same type of matter effect in accelerator-based

---

[13] This is often called the θ_{23} octant unknown, given that $|U_{\mu 3}|^2 > |U_{\tau 3}|^2$ implies $\theta_{23} > \pi/4$, while $|U_{\mu 3}|^2 < |U_{\tau 3}|^2$ implies $\theta_{23} < \pi/4$.

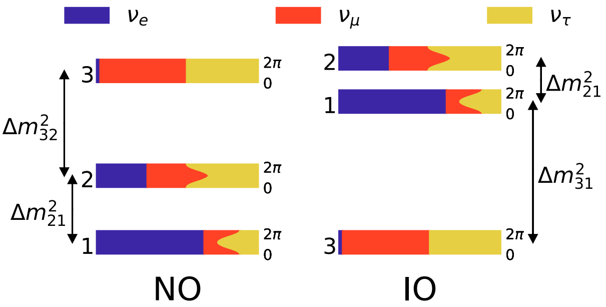

Fig. 1 Probability of finding a certain neutrino flavor in each neutrino mass eigenstate as the CP-violating phase, δ, is varied. The left and right panels show the normal (NO) and inverted (IO) mass orderings, respectively. Neutrino masses increase from bottom to top. The electron, muon, and tau flavor content of each neutrino mass eigenstate is shown via the blue, red, and yellow fractions, respectively. Reproduced from [18]

and atmospheric neutrino experiments should allow us to experimentally establish the neutrino mass ordering in the relatively near future. Future long-baseline neutrino oscillation experiments should also be able to resolve the $|U_{\mu 3}|^2 > |U_{\tau 3}|^2$ (ϑ_{23} octant) unknown, and to measure leptonic CP violation, provided that the true value of δ is sufficiently different from 0 and π. An independent approach to resolve the neutrino mass ordering, one that does not rely on matter effects is being pursued in medium-baseline reactor antineutrino experiments. In this case, the oscillation interference between the Δm^2_{31} and Δm^2_{32} mass splittings is exploited.

The current knowledge on neutrino masses and mixings provided by neutrino oscillation experiments is summarized in Fig. 1. The diagram shows the two possible mass orderings that are compatible with neutrino oscillation data, with increasing neutrino masses from bottom to top. In addition, the electron, muon, and tau flavor content of each mass eigenstate is also shown.

The absolute value of the neutrino mass scale can instead be probed via neutrinoless double-beta decay searches, cosmological observations, and beta decay experiments. Only upper bounds on the neutrino mass, of order ~ 1 eV, currently exist. Constraints on the lightest neutrino mass coming from neutrinoless double-beta decay will be discussed in Sect. 3.3. In the following, we briefly summarize cosmological and beta decay constraints.

Primordial neutrinos have a profound impact on cosmology, since they affect both the expansion history of the Universe and the growth of perturbations (see, for instance, reference [19]). Cosmological observations can probe the sum of the three-neutrino masses

$$m_{\text{cosmo}} \equiv \sum_{i=1}^{3} m_i . \tag{3}$$

Cosmological data are currently compatible with massless neutrinos. Several upper limit values on m_{cosmo} can be found in the literature, depending on the details of the cosmological datasets and of the cosmological model that were used in the analysis. A

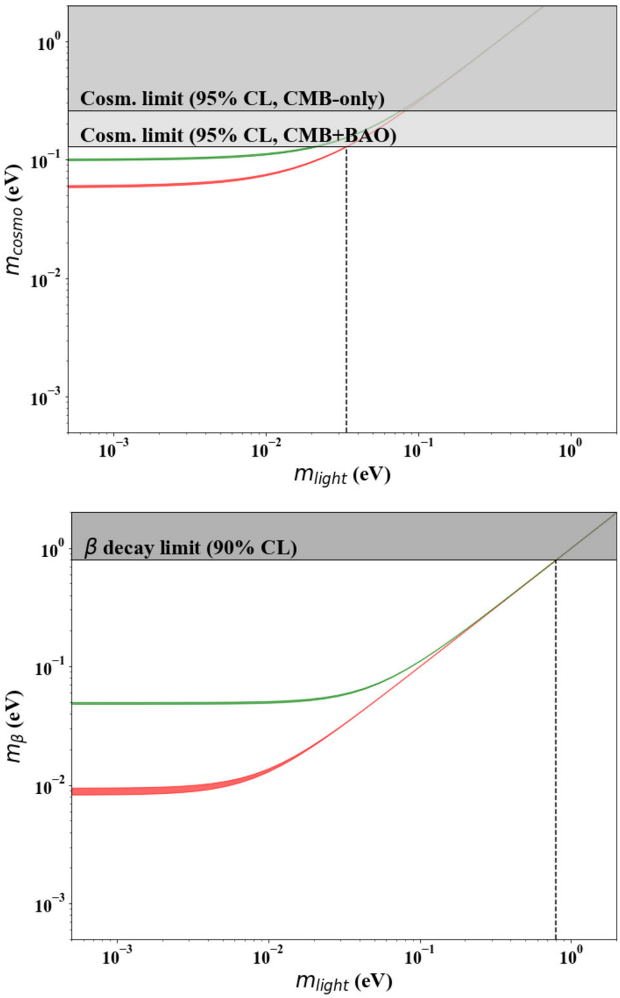

Fig. 2 Constraints on the lightest neutrino mass m_{light} coming from cosmological (upper panel) and β decay (lower panel) experiments. The red and green bands correspond to the normal and inverted orderings, respectively. The m_{cosmo} and m_{β} upper bounds in the top and bottom panels are from [21, 22], respectively. They translate into the m_{light} upper limits shown via the vertical dashed lines

conservative upper limit of $m_{\text{cosmo}} < 0.13$ eV at 95% confidence level is obtained when Cosmic Microwave Background (CMB) temperature measurements from the Planck satellite [20] are combined with the most recent Baryon Acoustic Oscillation (BAO) measurements from the Sloan Digital Sky Survey (SDSS) galaxy surveys including eBOSS [21], in the framework of a Lambda Cold Dark Matter (ΛCDM) model with dark energy whose equation of state is fixed to -1. Even the use of Planck CMB temperature and polarization data alone yields a very robust, and competitive, limit $m_{\text{cosmo}} < 0.26$ eV at 95% CL [20]. The relationship between m_{cosmo}, defined in Eq. (3), and the lightest neutrino mass m_{light}—that is, m_1 (m_3) in the case of normal (inverted) ordering—is shown in the top panel of Fig. 2. The two bands correspond to the normal and inverted orderings, respectively. The width of the bands is given by the 3σ ranges in the mass oscillation parameters Δm^2_{21} and Δm^2_{31} [14]. The horizontal band in the top panel of Fig. 2 is the upper limit on m_{cosmo}. The $m_{\text{cosmo}} < 0.13$ eV upper bound translates into a limit of $m_{\text{light}} \lesssim 0.034$ eV at 95% CL in the normal-ordering case, as shown by the vertical dashed line in the top panel of Fig. 2, and into an even stricter m_{light} bound in the inverted ordering case.

The neutrino mass scale can also be probed in laboratory-based experiments (see, for example, [23]). The differential electron energy spectrum in nuclear β decay experiments is generally a superposition of spectra corresponding to the different neutrino mass eigenstates with masses m_i that contribute to the electron flavor. Since the energy resolution of current experiments cannot resolve the tiny mass differences Δm_{ij} of the three light-neutrino mass eigenstates, effectively the mass combination probed is given by

$$m^2_\beta \simeq \sum_{i=1}^{3} |U_{ei}|^2 m^2_i. \tag{4}$$

The relationship between m_β in Eq. (4) and m_{light} is shown in the bottom panel of Fig. 2. Again, the results of a recent global fit to neutrino oscillation data [14] are used to determine the 3σ bands for both the normal and inverted orderings. From the experimental point of view, the region of interest for the study of neutrino properties is located near the β endpoint. The most sensitive searches conducted so far are based on the decay of tritium, via ${}^3\text{H} \rightarrow {}^3\text{He}^+ e^- \bar{\nu}_e$, mostly because of the very low β endpoint energy of this element (18.6 keV). As for cosmology, β decay searches of neutrino mass have so far yielded negative results. The horizontal band in the bottom panel of Fig. 2 comes from the KATRIN experiment bound, $m_\beta < 0.8$ eV at 90% CL [22]. The resulting constraint on m_{light} is less stringent than the cosmological one, $m_{\text{light}} \lesssim 0.8$ eV at 90% CL.

2.2 The origin of neutrino mass: Dirac versus Majorana neutrinos

Are neutrinos their own antiparticles? If the answer is no, we speak of *Dirac neutrinos*. If the answer is yes, we speak of *Majorana neutrinos*. Both possibilities exist for the neutrino, being electrically neutral and not carrying any other charge-like conserved quantum number. Whether neutrinos are Majorana or Dirac particles depends on the nature of the physics that give them mass, given that the two characters are physically indistinguishable for massless neutrinos.

In the Standard Model, only the negative chirality component Ψ_L of a fermion field $\Psi = \Psi_R + \Psi_L$ is involved in the weak interactions. A negative (positive) chirality field $\Psi_{L(R)}$ is a field that obeys the relations $P_{L(R)}\Psi_{L(R)} = \Psi_{L(R)}$ and $P_{R(L)}\Psi_{L(R)} = 0$, where $P_L = (1 - \gamma_5)/2$ and $P_R = (1 + \gamma_5)/2$ are the positive and negative chiral projection operators.

For massless neutrinos (see, for example, [24]), only the negative chirality neutrino field ν_L is needed in the theory, regardless of the Dirac/Majorana nature of the neutrino discussed below, since neutrinos only participate in the weak interactions. This field describes *negative helicity* neutrino states $|\nu_L\rangle$ and *positive helicity* antineutrino states.[14] The positive and negative helicity states are eigenstates of the helicity operator $h \equiv \vec{\sigma} \cdot \hat{p}$ with eigenvalues $\pm 1/2$, respectively, where $\vec{\sigma}$ is the neutrino spin and $\hat{p}$ the neutrino momentum direction. The fact that ν_L annihilates particles of negative helicity, and creates antiparticles with positive helicity, is not inconsistent with Lorentz invariance, given that the helicity is the same in any reference frame for a fermion traveling at the speed of light. In the Standard Model with massless neutrinos, positive helicity neutrinos and negative helicity antineutrinos do not exist. As a consequence, and since a negative helicity state transforms into a positive helicity state under the parity transformation, the chiral nature of the weak interaction (differentiating negative from positive chirality) implies that parity is maximally violated in the weak interactions.

For relativistic neutrinos of non-zero mass m, the neutrino field participating in the weak interactions has still negative chirality, ν_L, but there are sub-leading corrections to the particle annihilation/creation rules described above. The state $|\nu_L\rangle$ that is annihilated by the negative chirality field ν_L is now a linear superposition of the $-1/2$ and $+1/2$ helicity states. The $+1/2$ helicity state enters into the superposition with a coefficient $\propto m/E$, where E is the neutrino energy, and is therefore highly suppressed.

Neutrino mass terms can be added to the Standard Model Lagrangian in two ways (see, for example, [25]). The first way is in direct analogy to the Dirac masses of quarks and charged leptons, by adding the positive chirality component ν_R of the Dirac neutrino field, describing predominantly positive helicity neutrino states and predominantly negative helicity antineutrino states that do not participate in the weak interactions

$$- \mathcal{L}_D = m_D(\overline{\nu_L}\nu_R + \overline{\nu_R}\nu_L), \tag{5}$$

where $m_D = yv/\sqrt{2} > 0$, y is a dimensionless Yukawa coupling coefficient and $v/\sqrt{2}$ is the vacuum expectation value of the neutral Higgs field after electroweak symmetry breaking. In Eq. (5), ν_L and ν_R are, respectively, the negative and positive chirality components of the neutrino field ν. The chiral spinors ν_L and ν_R have only two independent components each, leading to the four independent components in the spinor ν. This is different from the case of massless neutrinos, where only the two-component spinor ν_L was needed.

The second way in which neutrino mass terms can be added to the Standard Model Lagrangian is unique to neutrinos. Majorana first realized [26] that, for neutral particles, one can remove two of the four degrees of freedom in a massive Dirac spinor by imposing the *Majorana condition*

$$\nu^c = \nu, \tag{6}$$

---

[14] As customarily done, we use the subscript "L" to denote both negative helicity states $|\nu_L\rangle$ and negative chirality fields ν_L, since the terms left-handed helicity states and left-handed chirality fields are also commonly used. Similarly, we denote positive helicity states and positive chirality fields with the subscript "R", as in "right-handed".

where $\nu^c = C\bar{\nu}^T = C(\gamma^0)^T\nu^*$ is the CP conjugate of the field ν, C is the charge-conjugation operator, $(\nu_L)^c = (\nu^c)_R$ has positive chirality, and $(\nu_R)^c = (\nu^c)_L$ has negative chirality. This result can be obtained by decomposing both the left-hand and right-hand sides of Eq. (6) into their chiral components, yielding

$$\nu_R = (\nu_L)^c \tag{7}$$

and therefore proving that the positive chirality component of the Majorana neutrino field ν_R is not independent of, but obtained from, its negative chirality counterpart ν_L. By substituting Eq. (7) into the mass term in Eq. (5), we obtain a *Majorana mass term*

$$-\mathcal{L}_L = \frac{1}{2}m_L(\overline{\nu_L}(\nu_L)^c + \overline{(\nu_L)^c}\nu_L), \tag{8}$$

where m_L is a free parameter with dimensions of mass. This Lagrangian mass term implies the existence of a weak isospin triplet scalar (a Higgs triplet), with a neutral component acquiring a non-vanishing vacuum expectation value after electroweak symmetry breaking. Equation (8) represents a mass term constructed from negative chirality neutrino fields alone, and we therefore call it a *negative chirality Majorana mass term*. If positive chirality fields also exist and are independent of negative chirality ones, this is not the only possibility. In this case, we may also construct a second Majorana mass term, a *positive chirality Majorana mass term*

$$-\mathcal{L}_R = \frac{1}{2}m_R(\overline{\nu_R}(\nu_R)^c + \overline{(\nu_R)^c}\nu_R). \tag{9}$$

In the Standard Model, right-handed fermion fields such as ν_R are weak isospin singlets. As a consequence, and in contrast with m_D or m_L, the mass parameter m_R is therefore not connected to a Higgs vacuum expectation value, and could be arbitrarily high. All three mass terms in Eqs. (5), (8) and (9) convert negative chirality states into positive chirality ones.[15] Chirality is, therefore, not a conserved quantity, regardless of the Dirac/Majorana nature of neutrinos. Furthermore, the Majorana mass terms in Eqs. (8) and (9) convert particles into their own antiparticles. As stated previously, they are therefore forbidden for all electrically charged fermions because of charge conservation. But not only: processes involving Majorana mass terms violate the Standard Model total lepton number $L \equiv L_e + L_\mu + L_\tau$ by two units ($|\Delta L| = 2$), which is not a good quantum number anymore.

Which of the mass terms allowed in theory, among $\mathcal{L}_D$, $\mathcal{L}_L$ and $\mathcal{L}_R$ in Eqs. (5), (8), and (9) exist in nature? What are the numerical values of the corresponding coupling constants m_D, m_L, m_R? These questions can in principle be answered experimentally. Majorana and Dirac massive neutrinos will in fact have different Standard Model interactions. Let us consider for now an instructive, albeit unrealistic, scattering experiment; see Fig. 3.

---

[15] This is because the charge conjugate of a field with a given chirality, such as the ones appearing in Eqs. 8 and 9, always has the opposite chirality.

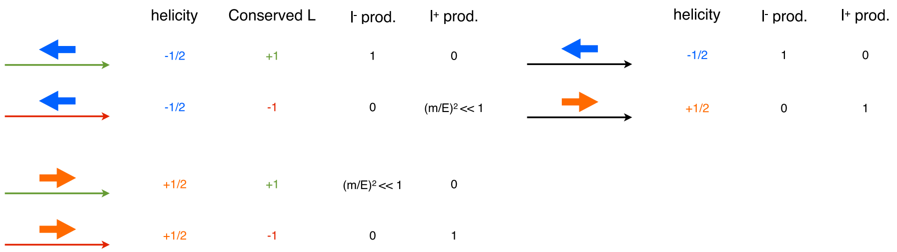

	helicity	Conserved L	l⁻ prod.	l⁺ prod.
⬅ →	-1/2	+1	1	0
⬅ →	-1/2	-1	0	$(m/E)^2 \ll 1$
➡ →	+1/2	+1	$(m/E)^2 \ll 1$	0
➡ →	+1/2	-1	0	1

	helicity	l⁻ prod.	l⁺ prod.
⬅ →	-1/2	1	0
➡ →	+1/2	0	1

Fig. 3 The difference between Dirac (left) and Majorana (right) massive neutrinos in a scattering experiment. See text for details. Adapted from [27]

In the Dirac case, Standard Model interactions conserve lepton number L, with $L(\nu) = L(l^-) = -L(\bar{\nu}) = -L(l^+) = +1$, where $l^{\pm}$ indicates charged leptons. Particles are then identified as neutrinos or antineutrinos in accordance with the process through which they are produced. Charged-current interactions of Dirac neutrinos (as opposed to antineutrinos) produce only l^- and carry a well-defined lepton number $L = -1$, and vice versa. As shown in Fig. 3, for Dirac neutrinos, we would thus have four mass-degenerate states: for each of the two available helicity states,[16] two distinct particle/antiparticle states characterized by a different L value would be available. Standard Model interactions of neutrino (as opposed to antineutrino) states of positive helicity would have, however, much weaker l^--producing interactions with matter compared to neutrino states of negative helicity, as indicated by the coefficients in Fig. 3. On the other hand, we have seen that in the Majorana case, L is not conserved. We would only have two mass-degenerate states, defined by the two available helicity states; see Fig. 3.

Given these differences between Dirac and Majorana massive neutrinos, can we establish which of the two possibilities is realized in Nature via a scattering experiment? In practice, no. The reason is that l^- production from positive helicity Dirac neutrinos (and l^+ production from negative helicity Dirac antineutrinos) is expected to be highly suppressed in the ultra-relativistic limit, and cannot be experimentally observed. Experimentally, all we know is that the neutral particle produced in association with a l^+ produces, when interacting, a l^-. In the Dirac case, lepton number conservation is assumed, and such neutral particle is identified as the neutrino, with $L = -1$. In the Majorana case, such neutral particle is instead identified as the negative helicity state, interacting differently from its positive helicity counterpart. Both interpretations are viable, and what happens when a neutrino interacts can be understood without invoking a conserved lepton number [28].

Interestingly, the possible observation of the scattering of non-relativistic neutrinos has attracted recent attention. In the non-relativistic case, the difference between Majorana and Dirac neutrinos would become pronounced. The only source of non-relativistic neutrinos known in Nature is the Cosmic Neutrino Background (CNB). Strong indirect evidence for CNB neutrinos exists from cosmological probes, although the CNB has never been directly detected thus far. The neutrino capture on beta-

---

[16] As mentioned above, the weak interaction is maximally parity violating, and therefore, the two helicity states are distinguishable.

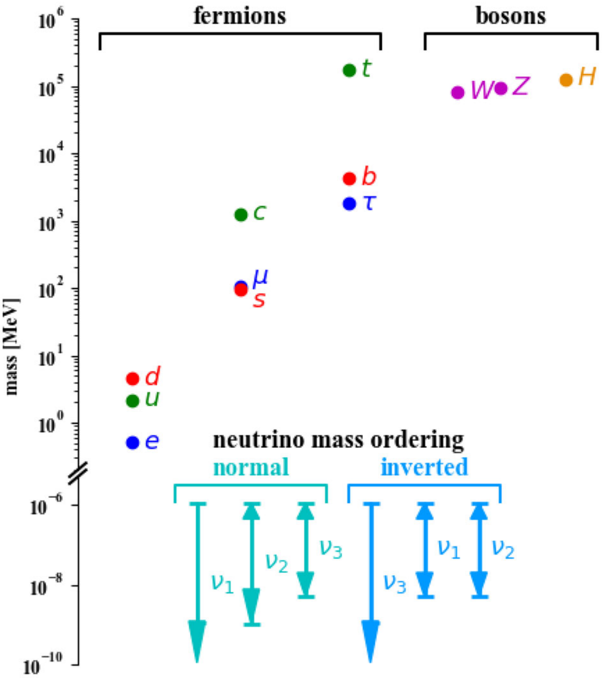

Fig. 4 Hierarchical structure of elementary particle masses. Only upper bounds for neutrino masses exist. Both normal and inverted neutrino mass ordering scenarios are shown. Mass values are taken from [17]

decaying nuclei, such as tritium ($\nu + {}^3\text{H} \rightarrow {}^3\text{He} + \text{e}^-$) and first proposed by Weinberg [29], is being explored by the PTOLEMY Collaboration for the CNB detection [30]. The observation of such a process with sufficient event statistics would provide information on the Dirac/Majorana nature of neutrinos, considering that the capture rate for Majorana neutrinos can be up to a factor of two larger than the one for Dirac neutrinos [31].

2.3 The see-saw mechanism

Neutrino masses, although not measured yet, are known to be small, of the order of 1 eV or less; see Sect. 2.1. Such mass values are much smaller than the masses of all other elementary fermions; see Fig. 4. The explanation of neutrino masses via Dirac mass terms alone require neutrino Yukawa couplings of the order of 10^{-12} or less. The current theoretical prejudice is that neutrino Yukawa couplings with $y_\nu \ll 1$ and $y_\nu \ll y_l$ are unnatural, if not unlikely.

The so-called *see-saw mechanism* provides a way to accommodate neutrino masses that is considered more natural. The simplest realization of the see-saw model is to add both a Dirac mass term and a positive chirality mass term to the Lagrangian, as given by Eqs. (5) and (9), respectively, for each of the three neutrino flavors. This is sometimes called the *type I see-saw mechanism*, where we take $m_L = 0$, $m_D \neq 0$, and $m_R \neq 0$. In this case, the neutrino mass terms can be recast in the matrix form

$$-\mathcal{L}_{\text{D+R}} = \frac{1}{2}\,\overline{(\mathcal{N}_L)^c}\,M\,\mathcal{N}_L + \text{h.c.}, \tag{10}$$

where the matrix M has the form

$$M = \begin{pmatrix} 0 & m_{\text{D}} \\ m_{\text{D}} & m_R \end{pmatrix}, \tag{11}$$

and the negative chirality vector $\mathcal{N}_L$ is

$$\mathcal{N}_L = \begin{pmatrix} \nu_L \\ (\nu_R)^c \end{pmatrix}. \tag{12}$$

The chiral fields ν_L and ν_R do not have a definite mass, since they are coupled by the Dirac mass term. To find the fields ν_{1L} and N_{1L} with definite masses m_1 and M_1, respectively, it is necessary to diagonalize the mass matrix in Eq. (10). In other words, it is necessary to find a unitary mixing matrix $\mathcal{U}$, such that

$$\mathcal{U}^T\,M\,\mathcal{U} = \begin{pmatrix} m_1 & 0 \\ 0 & M_1 \end{pmatrix}, \tag{13}$$

where

$$\mathcal{N}_L = \mathcal{U}\,n_L, \qquad \text{with} \qquad n_L = \begin{pmatrix} \nu_{1L} \\ N_{1L} \end{pmatrix}. \tag{14}$$

For each neutrino flavor, two fields of definite chirality and definite mass are therefore obtained, and the diagonalized mass terms can be written as

$$-\mathcal{L}_{D+R} = \frac{1}{2}\left(m_1\,\overline{(\nu_{1L})^c}\,\nu_{1L} + M_1\,\overline{(N_{1L})^c}\,N_{1L}\right) + \text{h.c.} \tag{15}$$

Both terms in Eq. (15) have the same form as the pure negative chirality Majorana mass term in Eq. (8). In other words, both mass eigenfields ν_{1L} and N_{1L} are equal to their CP-conjugate fields, and thus, both describe Majorana particles. The insertion of a Dirac mass term and a positive chirality Majorana mass term in the Lagrangian for massive neutrinos has resulted in Majorana particles.

Since the positive chirality fields are electroweak singlets in the Standard Model, the Majorana mass of the neutrino described by such field, m_R, may be orders of magnitude larger than the electroweak scale. In the so-called *see-saw limit*, we assume that neutrino Yukawa couplings are of the order of the charged fermion couplings, and that $m_R \gg m_D$ is of the order of some high mass scale where new physics responsible for neutrino masses is supposed to reside. In this approximation, the see-saw mechanism naturally yields a small mass eigenvalue $m_1 \simeq m_D^2/m_R \ll m_D$ for a predominantly negative helicity neutrino mass state, and a large mass eigenvalue

$M_1 \simeq m_R$ for a predominantly positive helicity (and therefore sterile) neutrino mass state. A very heavy N_1 corresponds to a very light ν_1 and vice versa, as in a see-saw.

The see-saw mechanism presented above can easily be generalized from the one-family case that we discussed to three-neutrino species, yielding the three light neutrinos ν_i we are familiar with, and three heavy neutrinos N_i, with $i = 1, 2, 3$ [25]. In this case, the neutrino mass matrix in Eq. 10 is a 6×6 mass matrix of the form

$$M = \begin{pmatrix} 0 & \left(M^{\mathrm{D}}\right)^T \\ M^{\mathrm{D}} & M^R \end{pmatrix}, \tag{16}$$

where M^D and M^R are now 3×3 complex matrices, and the six-component vector of negative chirality fields has the form

$$N_L = \begin{pmatrix} \nu_L \\ (\nu_R)^c \end{pmatrix}, \quad \text{with} \quad \nu_L = \begin{pmatrix} \nu_{eL} \\ \nu_{\mu L} \\ \nu_{\tau L} \end{pmatrix} \quad \text{and} \quad (\nu_R)^c = \begin{pmatrix} (\nu_{s_1 R})^c \\ (\nu_{s_2 R})^c \\ (\nu_{s_3 R})^c \end{pmatrix}. \tag{17}$$

In Eq. 17, the subscripts $e,\ \mu,\ \tau$ label the active neutrino flavors, while the subscripts $s_1,\ s_2,\ s_3$ indicate sterile states that do not participate in the weak interactions. The mass matrix is diagonalized via a 6×6 mixing matrix $\mathcal{V}$ analogous to $\mathcal{U}$ in Eq. 13, where the three negative chirality fields and the three positive chirality fields are now expressed in terms of the negative chirality components of 6 massive neutrino fields $\nu_{iL},\ i = 1, \ldots, 6$. In the see-saw limit where the eigenvalues of M^R are much larger than those of M^D, the 6×6 mass matrix in Eq. 16 can be written in block-diagonal form $M \simeq \mathrm{diag}(M_{\mathrm{light}}, M_{\mathrm{heavy}})$, where the two 3×3 mass matrices of the light and heavy neutrino sectors are practically decoupled, and given by $M_{\mathrm{light}} \simeq -(M^D)^T (M^R)^{-1} M^D$ and $M_{\mathrm{heavy}} \simeq M^R$, respectively.

For the low-energy phenomenology, it is sufficient to consider only M_{light}, sometimes called the *neutrino mass matrix* m_ν, that is the 3×3 matrix in the flavor basis which is diagonalized by the matrix U

$$U^T\, M_{\mathrm{light}}\, U = \mathrm{diag}(m_1, m_2, m_3)\,, \tag{18}$$

where the *neutrino mixing matrix* U appearing in Eq. (18) is the same matrix defined in Eq. (1), and $m_1,\ m_2,\ m_3$ are three light-neutrino mass eigenvalues discussed in Sect. 2.1.

An important assumption in the simplest realization of the see-saw mechanism described above is that $m_L = 0$. This assumption is not arbitrary, and directly follows from enforcing the gauge symmetries of the Standard Model; see for example [25].

There exist other realizations of the see-saw mechanism, which differ from the Type-I mechanism in the nature of the new heavy degrees of freedom that are added to the Standard Model. While three gauge-singlet fermions are introduced in Type-I, Type-II, and Type-III, see-saw models add one gauge-triplet scalar and three gauge-triplet fermions, respectively.

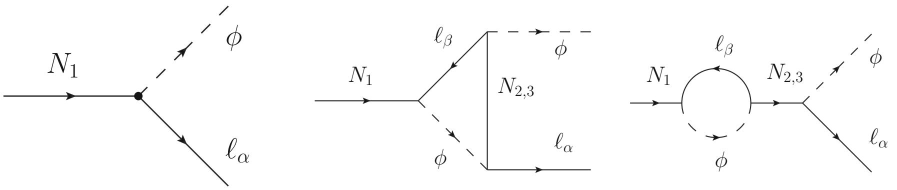

Fig. 5 Feynman diagrams that contribute to the lepton number asymmetry through the decays of the heavy Majorana neutrino N_1 into the Higgs ϕ plus leptons l_α. The asymmetry is generated via the interference of the tree-level diagram (left) with the one-loop vertex correction (center) and the self-energy (right) diagrams (adapted from [32])

2.4 Leptogenesis

Inflationary models of the Universe predict matter and antimatter to be equally abundant at the very hot beginning, given that any potential initial asymmetry would have been diluted away by inflation. However, the observable Universe today is almost entirely made of matter! This matter dominance today is consistent with the small level of baryon asymmetry that is inferred from BBN and CMB observations, given that annihilation of matter with antimatter would have left us in a matter-dominated Universe today. The baryon asymmetry has been precisely measured [17, 20]

$$\eta \equiv \frac{n_B - n_{\bar{B}}}{n_\gamma} = 274 \times 10^{-10}\Omega_b h^2 = (6.12 \pm 0.04) \times 10^{-10}, \tag{19}$$

where n_B, $n_{\bar{B}}$, n_γ are the number densities of baryons, antibaryons, and photons, $\Omega_b h^2 = (0.0224 \pm 0.0001)$ is the fraction of the critical energy density carried by baryons, and $h \equiv H_0/100\,\mathrm{km}\cdot\mathrm{s}^{-1}\cdot\mathrm{Mpc}^{-1} = (0.674 \pm 0.005)$ is the Hubble parameter, where H_0 is the Hubble constant today.

What caused this matter–antimatter asymmetry in the early Universe? The baryon asymmetry could have been induced by a lepton asymmetry: *leptogenesis* (see, for example, [32, 33]). If neutrinos are Majorana particles, the decays of the heavy Majorana neutrinos into leptons l_α plus Higgs particles ϕ in the early Universe provide an ideal scenario for leptogenesis. Heavy Majorana neutrinos are their own antiparticles, so they can decay to both $l_\alpha\phi$ and $\bar{l_\alpha}\bar{\phi}$ final states. If there is an asymmetry in the two decay rates, a net lepton asymmetry will be produced. Figure 5 shows the processes that would contribute to a net lepton asymmetry in the presence of heavy Majorana neutrino decays, in the simplest case where the asymmetry is dominated by the decay of the lightest among the three heavy neutrinos, N_1. Finally, this lepton asymmetry can be efficiently converted into a baryon asymmetry via the so-called *sphaleron processes* (see [32, 33] for details).

In more detail, for leptogenesis to occur, three conditions must be met. These conditions directly follow from the ingredients that are required to dynamically generate a baryon asymmetry (*Sakharov's conditions* [34]):

1. Presence of lepton number violating processes;

2. Beyond-SM sources of CP violation[17];
3. Departure from thermal equilibrium, so that the inverse processes do not wash out the generated lepton asymmetry.

The decay of heavy Majorana neutrinos can provide all of these conditions, namely

1. Total lepton number is violated in these decays;
2. CP can be violated in these decays, provided that there is more than one heavy Majorana field;
3. Departure from thermal equilibrium is obtained if the decay rate is slower than the expansion rate of the Universe at the time of decoupling, occurring for $T \sim M_1$, where T is the temperature of the Universe's thermal bath, and M_1 is the mass of the lightest among the three heavy neutrinos.

To be fully successful, any theory of leptogenesis must be able to explain the observed magnitude of baryon asymmetry given in Eq. (19). Leptogenesis via heavy Majorana neutrino decays is in principle able to do this. In this case, the asymmetry in lepton flavor α produced in the decay of N_1, defined as

$$\varepsilon_{\alpha\alpha} \equiv \frac{\Gamma(N_1 \to \phi l_\alpha) - \Gamma(N_1 \to \bar{\phi}\bar{l}_\alpha)}{\Gamma(N_1 \to \phi l) + \Gamma(N_1 \to \bar{\phi}\bar{l})} \tag{20}$$

should be of order $|\varepsilon_{\alpha\alpha}| > 10^{-7}$ [33], where the factors Γ in Eq. (20) stand for the decay rates into the corresponding N_1 decay final states. It is at present unclear whether there is a direct connection between the high-energy CP-violating processes responsible for the asymmetry in the early Universe of Eq. (20), and the low-energy CP-violating processes that may potentially affect laboratory-based experiments. Nonetheless, the discovery of CP violation in the lepton sector via neutrino oscillations on the one hand, and the discovery of the Majorana nature of neutrinos via neutrinoless double-beta decay on the other, would undoubtedly strengthen the case for leptogenesis as a source of the baryon asymmetry of the Universe.

2.5 Lepton number violating processes

We have seen that Majorana mass terms induce lepton number violating processes of the type $|\Delta L| = 2$. The Majorana nature of the heavy neutrino needed for leptogenesis, discussed in Sect. 2.4, implies lepton number violating processes. However, this decay is unobservable in a laboratory-based experiment, given the tremendous energies needed for the production of such a heavy neutrino.[18] A number of more promising lepton number violating processes have been proposed to probe the Majorana nature of neutrinos. The best-known example is $\beta\beta0\nu$, the subject of this review and introduced in Sect. 3. We anticipate that $\beta\beta0\nu$ is considered the most promising probe of the Majorana nature of neutrinos. However, and because of neutrino mixing, the phenomenology associated with $|\Delta L| = 2$ processes is very rich. The basic process with $|\Delta L| = 2$ is mediated by [36]

---

[17] CP violation is allowed by the Standard Model and has been measured; however, the magnitude of such CP-violating effects is far too small to provide the necessary amount of leptogenesis.

[18] For strongly hierarchical heavy neutrino masses, a lower bound on the right-handed neutrino mass from leptogenesis of order 10^9 GeV is obtained [35].

$$W^- W^- \to l_\alpha^- l_\beta^-, \tag{21}$$

and we can categorize such processes according to the lepton flavors (α, β) involved. Assuming no lepton flavor violating contributions other than light Majorana neutrino exchange, the matrix element for the generic $|\Delta L| = 2$ process in Eq. (21) is proportional to the element (α, β) of the *neutrino mass matrix*

$$(m_\nu)_{\alpha\beta} \equiv \left(U^* \mathrm{diag}(m_1, m_2, m_3) U^\dagger\right)_{\alpha\beta} = \sum_{i=1}^{3} U_{\alpha i}^* U_{\beta i}^* m_i, \tag{22}$$

where $m_\nu = M^{\text{light}}$ is the matrix appearing in Eq. (18), $U_{\alpha i}$ are the elements of the 3×3 neutrino mixing matrix appearing in Eq. 1, and m_i are the three light-neutrino masses. In a sense, this effective neutrino mass definition provides a metric to compare the sensitivity of various $|\Delta L| = 2$ processes. The processes with the most competitive constraints on $|\Delta L| = 2$ processes involving the flavors (α, β) are reported in Table 1.

As is apparent in Table 1, indeed, the constraint on the effective Majorana mass m_{ee} coming from $\beta\beta0\nu$ searches outperforms by several orders of magnitude other searches involving a different flavor combination (α, β). The most important reason behind this is of statistical nature. While it is possible to amass macroscopic quantities of a $\beta\beta$ emitter to study $\beta\beta0\nu$ decay [as we will see, even $\mathcal{O}(1$ ton) of isotope is in the cards of several experiments], this is not the case for the other experimental techniques listed in Table 1. Nevertheless, it is important to keep exploring lepton flavor violating processes other than $\beta\beta0\nu$ for two reasons. First, it is in principle possible that phase cancelations are such that $m_{ee} \ll m_{\alpha\beta}$ with $(\alpha, \beta) \neq (e, e)$, making the search for $\beta\beta0\nu$ much less favorable than others because of Nature's choice of neutrino masses and mixings. Second, this effort may lead to the identification of an even most promising experimental probe of lepton flavor violation in the future.

3 Neutrinoless double-beta decay

3.1 Double-beta decay modes

Double-beta decay is a rare nuclear transition in which a nucleus with Z protons decays into a nucleus with $Z + 2$ protons and the same mass number A. The decay can occur only if the atomic mass of the initial nucleus is larger than the one of the final nucleus, and both more than the one of the intermediate nucleus, as shown in Fig. 6. Such a condition is fulfilled by 35 nuclides in nature because of the nuclear pairing force (see Sect. 4.2), ensuring that nuclei with even Z and N are more bound than the odd–odd nuclei with the same $A = Z + N$.

Table 1 Current bounds on effective neutrino masses from total lepton number violating processes, organized according to the flavors involved

Flavors	Method	Experimental bound	Mass bound (eV)
(e, e)	$\beta\beta0\nu$	$T_{1/2}(^{136}\mathrm{Xe} \rightarrow ^{136}\mathrm{Ba} + 2e^-) > 2.3 \times 10^{26}$ yr	$\|m_{ee}\| < (3.6 - 15.6) \times 10^{-2}$
(e, μ)	$\mu^- \rightarrow e^+$	$\Gamma(\mathrm{Ti} + \mu^- \rightarrow e^+ + \mathrm{Ca_{gs}})\ /\ \Gamma(\mathrm{Ti} + \mu^- \mathrm{capture}) < 1.7 \times 10^{-12}$	$\|m_{e\mu}\| < 1.7 \times 10^7$
(e, τ)	τ decays	$\Gamma(\tau^- \rightarrow e^+\pi^-\pi^-)\ /\ \Gamma_{\mathrm{tot}} < 2.0 \times 10^{-8}$	$\|m_{e\tau}\| < 1.2 \times 10^{12}$
(μ, μ)	K decays	$\Gamma(K^+ \rightarrow \pi^-\mu^+\mu^+)\ /\ \Gamma_{\mathrm{tot}} < 4.2 \times 10^{-11}$	$\|m_{\mu\mu}\| < 5.7 \times 10^7$
(μ, τ)	τ decays	$\Gamma(\tau^- \rightarrow \mu^+\pi^-\pi^-)\ /\ \Gamma_{\mathrm{tot}} < 3.9 \times 10^{-8}$	$\|m_{e\tau}\| < 2.2 \times 10^{12}$
(τ, τ)	None	None	None

Numbers taken (or derived) from [17, 36]

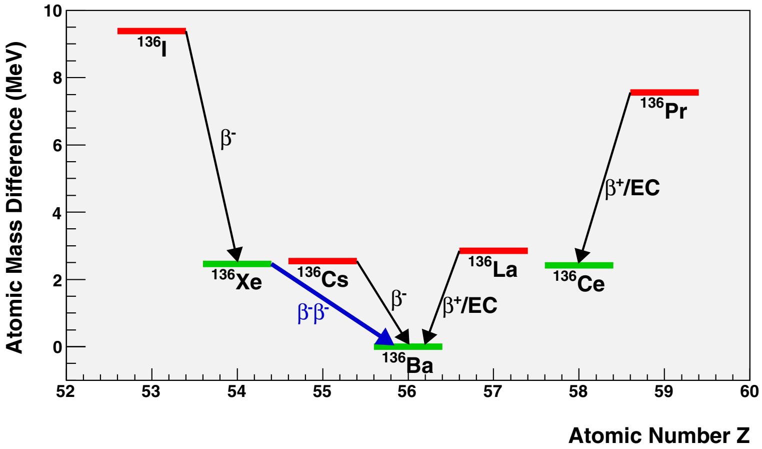

Fig. 6 Atomic masses of isotopes with $A = 136$ given as differences with respect to the most bound isotope, ^{136}Ba. The red (green) levels indicate odd–odd (even–even) nuclei. The arrows β^-, β^+, $\beta^-\beta^-$ indicate nuclear decays accompanied by electron, positron, and double-electron emission, respectively. The arrows EC indicate electron capture transitions

The standard decay mode ($\beta\beta2\nu$) consisting of two simultaneous beta decays

$$(Z, A) \rightarrow (Z+2, A) + 2\,e^- + 2\,\overline{\nu}_e \tag{23}$$

was first considered by Maria Goeppert-Mayer in 1935 [37]. Total lepton number is conserved in this mode, and the process is allowed in the Standard Model of particle physics. This process was first detected in 1950 using geochemical techniques [38]. The first direct observation of $\beta\beta2\nu$ events, in ^{82}Se and using a time projection chamber, did not happen until 1987 [39, 40]. Since then, it has been repeatedly observed in several nuclides. Typical lifetimes are of the order of 10^{19}–10^{21} years, among the longest ever observed among radioactive decay processes,[19]. For a list of $\beta\beta2\nu$ half-lives measured in several isotopes, see Table 2 [42]. The longest half-life in Table 2 is the one for ^{136}Xe, which was measured for the first time only in 2011 [43].

The neutrinoless mode ($\beta\beta0\nu$)

$$(Z, A) \rightarrow (Z+2, A) + 2\,e^- \tag{24}$$

was first proposed by W. H. Furry in 1939 [72] as a method to test Majorana's theory [26] applied to neutrinos. In contrast to the two-neutrino mode, the neutrinoless mode violates total lepton number conservation and is therefore forbidden in the Standard Model. Its existence is linked to that of Majorana neutrinos (see Sect. 3.2). No convincing experimental evidence of the decay exists to date.

The two modes of the $\beta\beta$ decay have some common and some distinct features [73]. The common ones are as follows:

---

[19] To our knowledge, only the closely related two-neutrino double-electron capture process of ^{124}Xe with a half-life of $(1.8 \times 0.5) \times 10^{22}$ yr [41] has been measured directly to have a longer half-life than the $\beta\beta2\nu$ processes in Table 2.

Table 2 Current best direct measurements of the half-life of $\beta\beta 2\nu$ processes

Isotope	$T_{1/2}^{2\nu}$ (year)	Experiments
^{48}Ca	$(5.3^{+1.2}_{-0.8}) \times 10^{19}$	Irvine TPC [44], TGV [45], NEMO-3 [46]
^{76}Ge	$(1.88 \pm 0.08) \times 10^{21}$	HEIDELBERG-MOSCOW [47], GERDA [48]
^{82}Se	$(0.87 \pm ^{+0.02}_{-0.01}) \times 10^{20}$	NEMO-3 [49], CUPID-0 [50], Irvine TPC [51], NEMO-2 [52]
^{96}Zr	$(2.3 \pm 0.2) \times 10^{19}$	NEMO-2 [53], NEMO-3 [54]
^{100}Mo	$(7.06^{+0.15}_{-0.13}) \times 10^{18}$	NEMO-3 [55], CUPID-Mo [56], NEMO-2 [57], Irvine TPC [58], ZnMoO$_4$ bolometers [59]
^{116}Cd	$(2.69 \pm 0.09) \times 10^{19}$	NEMO-3 [60], Aurora [61], ELEGANT [62], Solotvina [63], NEMO-2 [64]
^{130}Te	$(7.91 \pm 0.21) \times 10^{20}$	CUORE-0 [65], CUORE [66], CUORICINO [67], NEMO-3 [68]
^{136}Xe	$(2.18 \pm 0.05) \times 10^{21}$	EXO-200 [69], KamLAND-Zen [70]
^{150}Nd	$(9.34 \pm 0.65) \times 10^{18}$	NEMO-3 [71]

The values reported are taken from the averaging procedure described in [42]

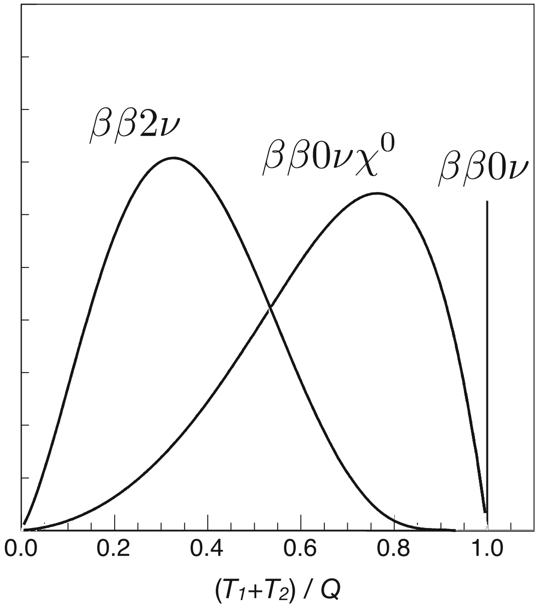

Fig. 7 Spectra for the sum kinetic energy $T_1 + T_2$ of the two electrons, for different $\beta\beta$ modes: $\beta\beta2\nu$, $\beta\beta0\nu$, and $\beta\beta$ decay with Majoron emission

- The leptons carry essentially all the available energy, and the nuclear recoil is negligible.
- The transition involves the 0^+ ground state of the initial nucleus and, in almost all cases, the 0^+ ground state of the final nucleus. For some isotopes, it is energetically possible to have a transition to an excited 0^+ or to a 2^+ final state,[20] even though they are suppressed because of the smaller phase space available.
- Both processes are second-order weak processes, i.e., their rate is proportional to G_F^4, where G_F is the Fermi constant. They are, therefore, inherently slow. Phase-space considerations alone would give preference to the $\beta\beta0\nu$ mode, which is, however, forbidden by total lepton number conservation.

The distinct features are:

- In the $\beta\beta2\nu$ mode, the sum electron kinetic energy $T_1 + T_2$ spectrum is continuous and peaked below $Q_{\beta\beta}/2$, where $Q_{\beta\beta}$ is the Q-value of the reaction. In the $\beta\beta0\nu$ mode, since no light particles other than the electrons are emitted and given that nuclear recoil energy is negligible, the $T_1 + T_2$ spectrum is a mono-energetic line at $Q_{\beta\beta}$, smeared only by the detector resolution. This is illustrated in Fig. 7.
- The $\beta\beta2\nu$ mode probes momentum transfers of order $\mathcal{O}(Q_{\beta\beta}) \simeq \mathcal{O}(1\,\text{MeV})$, while the $\beta\beta0\nu$ reaction probes much higher momentum transfers of order $\mathcal{O}(m_\pi) \simeq \mathcal{O}(100\,\text{MeV})$.

In addition to the two basic decay modes described above, several decay modes involving the emission of a light neutral boson, the Majoron (χ^0), have been proposed in extensions of the Standard Model; see Sect. 3.4.

---

[20] The transition to an excited 0^+ final state has been observed for both ^{100}Mo [74–80] and ^{150}Nd [81–83].

While, in the following, we will focus on $\beta\beta0\nu$ as defined in Eq. (24), there are three closely related lepton number violating processes that can be investigated:

$$\beta^+\beta^+0\nu: \quad (Z, A) \rightarrow (Z-2, A) + 2\,e^+ \tag{25}$$

$$\beta^+\mathrm{EC}0\nu: e^- + (Z, A) \rightarrow (Z-2, A) + e^+ \tag{26}$$

$$\mathrm{ECEC}0\nu: \quad 2\,e^- + (Z, A) \rightarrow (Z-2, A)^*. \tag{27}$$

Such processes are called *double positron emission*, *single positron emission plus single-electron capture* (EC), and *double-electron capture*, respectively. All three involve transitions where the nuclear charge decreases (as opposed to increasing, as in $\beta\beta0\nu$) by two units. From the theoretical point of view, the physics probed by $\beta^+\beta^+0\nu$, $\beta^+\mathrm{EC}0\nu$ and $\mathrm{ECEC}0\nu$ is identical to the one probed by $\beta\beta0\nu$. From the experimental point of view, however, $\beta^+\beta^+0\nu$ and $\beta^+\mathrm{EC}0\nu$ are less favorable than $\beta\beta0\nu$ because of the smaller phase space available. On the other hand, the process $\mathrm{ECEC}0\nu$ is gaining some attention recently as a promising (but still much less developed) alternative to $\beta\beta0\nu$, since a resonant enhancement of its rate can in principle occur [84].

In the following, the neutrinoless mode $\beta\beta0\nu$ is discussed in more detail, from both the theoretical and experimental point of views.

3.2 The black box theorem

In general, in theories beyond the Standard Model, there may be several sources of total lepton number violation which can lead to $\beta\beta0\nu$. Nevertheless, as it was first pointed out in reference [85], irrespective of the mechanism, $\beta\beta0\nu$ necessarily implies Majorana neutrinos. This is called the *black box* (or Schechter–Valle) theorem. The reason is that any $\Delta L \neq 0$ diagram contributing to the decay would also contribute to the (e, e) entry of the Majorana neutrino mass matrix, $(m_\nu)_{ee}$. This is shown in Fig. 8, where a $\bar{\nu}_e - \nu_e$ transition, that is a non-zero $(m_\nu)_{ee}$, is induced as a consequence of any $\Delta L \neq 0$ operator responsible for $\beta\beta0\nu$.

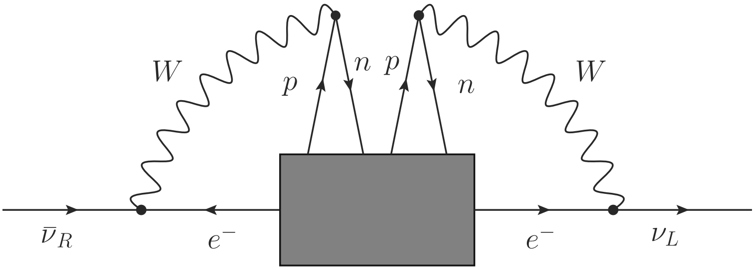

Fig. 8 Diagram showing how any neutrinoless double-beta decay process induces a $\bar{\nu}$-to-ν transition, that is, an effective Majorana mass term. This is the so-called *black box theorem* [85]

Fig. 9 The standard mechanism for $\beta\beta0\nu$ decay, based on light Majorana neutrino exchange

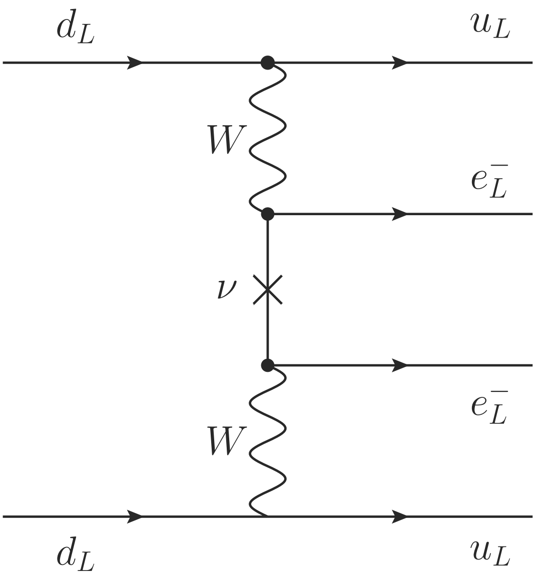

From a quantitative point of view, however, the diagram in Fig. 8 corresponds to a tiny (of order $\mathcal{O}(10^{-28}$ eV)) mass generated at the four-loop level, and is far too small to explain the neutrino mass splittings observed in neutrino oscillation experiments [86]. Other, unknown, Majorana and/or Dirac mass contributions must exist. As a consequence, therefore, the black box theorem says nothing about the physics mechanism dominating a $\beta\beta0\nu$ rate that is large enough to be observable. The dominant mechanism leading to $\beta\beta0\nu$ could then either be directly connected to neutrino oscillations phenomenology, or only indirectly connected or not connected at all to it [87]. The former case is realized in the standard $\beta\beta0\nu$ mechanism of light-neutrino exchange, discussed in Sect. 3.3. The latter case involves alternative $\beta\beta0\nu$ mechanisms, briefly outlined in Sect. 3.4.

3.3 The standard neutrinoless double-beta decay mechanism: light Majorana neutrino exchange

Neutrinoless double-beta decay can arise from a diagram (Fig. 9) in which the parent nucleus emits a pair of virtual W bosons, and then, these W exchange a Majorana neutrino to produce the outgoing electrons. The rate is non-zero only for massive, Majorana neutrinos. The reason is that the exchanged neutrino in Fig. 9 can be seen as emitted (in association with an electron) with almost total positive helicity. Only its small, $\mathcal{O}(m/E)$, negative helicity component is absorbed in the other vertex by the Standard Model electroweak current. Considering that the amplitude is in this case a sum over the contributions of the three light neutrino mass states ν_i, and that is also proportional to U_{ei}^2, we conclude that the modulus of the amplitude for the $\beta\beta0\nu$ process must be proportional in this case to the *effective neutrino Majorana mass*

$$m_{\beta\beta} \equiv |\sum_{i=1}^{3} m_i U_{ei}^2|. \tag{28}$$

In other words, the effective neutrino Majorana mass corresponds to the modulus of the (e, e) element of the neutrino mass matrix of Eq. (22), $m_{\beta\beta} \equiv |(m_\nu)_{ee}|$.

In the case where light Majorana neutrino exchange is the dominant contribution to $\beta\beta0\nu$, the inverse of the half-life for the process can be written as [88]

$$\frac{1}{T_{1/2}^{0\nu}} = G^{0\nu}(Q, Z)\,|M^{0\nu}|^2\,m_{\beta\beta}^2, \tag{29}$$

where $G^{0\nu}(Q, Z)$ is a phase-space factor that depends on the transition Q-value and on the nuclear charge Z, and $M^{0\nu}$ is the nuclear matrix element (NME). The phase-space factor can be calculated analytically, in principle, with reasonable accuracy.[21] The NME is evaluated using nuclear models, although with considerable uncertainty (see Sect. 4). In other words, the value of the effective neutrino Majorana mass $m_{\beta\beta}$ in Eq. (28) can be inferred from a non-zero $\beta\beta0\nu$ rate measurement, albeit with some nuclear physics uncertainties. Conversely, if a given experiment does not observe the $\beta\beta0\nu$ process, the result can be interpreted in terms of an upper bound on $m_{\beta\beta}$.

If light Majorana neutrino exchange is the dominant mechanism for $\beta\beta0\nu$, it is clear from Eq. (28) that $\beta\beta0\nu$ is in this case directly connected to neutrino oscillations phenomenology, and that it also provides direct information on the absolute neutrino mass scale, as cosmology and β decay experiments do (see Sect. 2.1). The relationship between $m_{\beta\beta}$ and the actual neutrino masses m_i is affected by:

1. the uncertainties in the measured oscillation parameters;
2. the unknown neutrino mass ordering (normal or inverted);
3. the unknown phases in the neutrino mixing matrix (both Dirac and Majorana).

For example, the relationship between $m_{\beta\beta}$ and the lightest neutrino mass m_{light} (which is equal to m_1 or m_3 in the normal and inverted mass ordering cases, respectively) is illustrated in Fig. 10. This graphical representation was first proposed in [89]. The width of the two bands is due to items 1 and 3 above, where the uncertainties in the measured oscillation parameters (item 1) are taken as 3σ ranges from a recent global oscillation fit [14]. Figure 10 also shows a 90% confidence level upper bound on $m_{\beta\beta}$ from current $\beta\beta0\nu$ data ($m_{\beta\beta} < 0.036{-}0.156$ eV). As can be seen from Fig. 10, current $\beta\beta0\nu$ data provide a constraint on the absolute mass scale m_{light} that is more competitive than the current one from β decay experiments, although less competitive as the cosmological one.

In Figs. 2 and 10, we have shown only upper bounds on various neutrino mass combinations, coming from current data. The detection of positive results for absolute neutrino mass scale observables would open up the possibility to further explore neutrino properties and lepton number violating processes. We give three examples in the following. First, the successful determination of both m_β in Eq. (4) and $m_{\beta\beta}$ in Eq. (28)

---

[21] An accurate description of the effect of the nuclear Coulomb field on the decay electron wave-functions is, however, required.

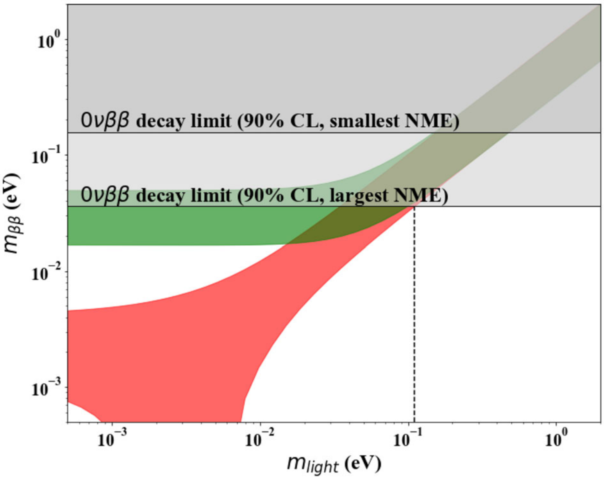

Fig. 10 The effective neutrino Majorana mass $m_{\beta\beta}$ as a function of the lightest neutrino mass, m_{light}. The red (green) band corresponds to the normal (inverted) ordering, respectively, in which case m_{light} is equal to m_1 (m_3). The horizontally excluded region comes from $\beta\beta0\nu$ constraints

via β and $\beta\beta0\nu$ decay experiments, respectively, can in principle be used to determine or constrain the phases α_i [90]. Second, measurements of m_β or m_{cosmo} in Eq. (3) may yield a constraint on m_{light} that is inconsistent with a $m_{\beta\beta}$ upper limit. In this case, the non-observation of $\beta\beta0\nu$ would suggest that neutrinos are Dirac particles. Third, measurements of m_β or m_{cosmo} may yield a constraint on m_{light} that is inconsistent with a measured non-zero $m_{\beta\beta}$. This scenario would demonstrate that additional lepton number violating physics, other than light Majorana neutrino exchange, is at play in the $\beta\beta0\nu$ process. We briefly describe some of these possible $\beta\beta0\nu$ alternative mechanisms in the following.

3.4 Alternative neutrinoless double-beta decay mechanisms

A number of alternative $\beta\beta0\nu$ mechanisms have been proposed. For an excellent and complete discussion of those, we refer the reader to [87]. The realization of $\beta\beta0\nu$ can differ from the standard mechanism in one or several aspects:

- The Lorentz structure of the currents. Positive chirality currents mediated by a W_R boson can arise, for example, in left–right symmetric theories. A possible diagram involving positive chirality current interactions of heavy Majorana neutrinos N_i is shown in Fig. 11a.
- The mass scale of the exchanged virtual particles. One example would be the presence of "sterile" (that is, described by positive chirality fields) neutrinos, either light or heavy, in the neutrino propagator of Fig. 9, in addition to the three light, active, neutrinos we are familiar with. Another example would be the exchange of heavy supersymmetric particles, as in Fig. 11b.

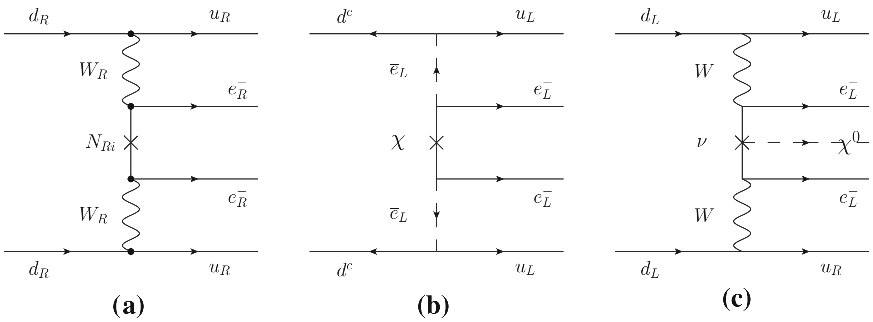

Fig. 11 Examples of non-standard mechanism for $\beta\beta0\nu$: **a** heavy neutrino exchange with positive chirality currents [91]; **b** neutralino exchange in R-parity violating supersymmetry [92]; **c** Majoron emission [93]

- The number of particles in the final state. A popular example involves decay modes where additional Majorons, that are very light or massless particles which can couple to neutrinos, are produced in association with the two electrons (see Fig. 11c).

In non-standard $\beta\beta0\nu$ mechanisms, the scale of the lepton number violating physics is often larger than the characteristic nuclear Fermi momentum scale $\mathcal{O}(100\ \text{MeV})$, in which case one speaks of *short-range* processes. This is the case when the $\beta\beta0\nu$ process is mediated by heavy particles. It is in contrast to the standard $\beta\beta0\nu$ mechanism of light Majorana neutrino exchange, in which case the neutrino is very light compared to this momentum transfer scale, resulting in a *long-range* process. Non-standard and long-range $\beta\beta0\nu$ processes are, however, also possible.

In general, several contributions to the total $\beta\beta0\nu$ amplitude can add coherently, allowing for interference effects. Neutrinoless double-beta decay observables alone may be able to identify the dominant mechanism responsible for $\beta\beta0\nu$. We give three examples. First, if Majorons are also emitted in association with the two electrons, energy conservation alone requires the electron kinetic energy sum $T_1 + T_2$ to be a continuous spectrum with $Q_{\beta\beta}$ as endpoint. This spectrum is potentially distinguishable from the $\beta\beta2\nu$ one (see Fig. 7), provided that the Majoron-neutrino coupling constant is large enough. Second, if positive chirality current contributions dominate the $\beta\beta0\nu$ rate, electrons will be emitted predominantly as positive helicity states. As a consequence, both the energy and angular correlation of the two emitted electrons will be different from the ones of the standard $\beta\beta0\nu$ mechanism. A detector capable of reconstructing individual electron tracks may, therefore, be able to distinguish this type of non-standard $\beta\beta0\nu$ mechanism from light Majorana neutrino exchange (see, for example, [94]). Third, the combined observation of $\beta\beta0\nu$ decays to both ground and excited states of the daughter isotope may also shed light on the $\beta\beta0\nu$ mechanism. Neutrinoless double-beta decays to excited states are, however, harder to search for, given the lower reaction Q-values and hence lower predicted rates. On the other hand, their experimental signature would be very characteristic, with typically one or two gamma rays emitted in coincidence with the two decay electrons.

4 Nuclear matrix elements

The $\beta\beta0\nu$ decay half-life has been introduced in Eq. (29) for a decay mediated by the exchange of light neutrinos. We recover the standard definition of the nuclear matrix element (NME) by factoring out the hadron coupling, g_A [95, 96]

$$T_{1/2}^{-1} = G^{0\nu}\,(Q, Z)\; g_A^4\, \left|M_{\rm light}^{0\nu}\right|^2\, m_{\beta\beta}^2\,, \tag{30}$$

where $M_{\rm light}^{0\nu}$ emphasizes that this NME only corresponds to the many-body part and to light-neutrino exchange.[22] As discussed in Sect. 3, the half-life necessarily depends on an unknown parameter that describes the mechanism beyond the standard model of particle physics responsible for the violation of lepton number in the decay, that is, for the creation of matter without antimatter. In the light-neutrino exchange scenario, this parameter is $m_{\beta\beta}$, as illustrated in Eqs. (29) and (30). Therefore, as discussed in Sect. 3.3, to gain information on new physics after the $\beta\beta0\nu$-decay discovery, the remaining components of the half-life must be reliably known. Moreover, a good knowledge of these parts allows one to estimate the reach, in terms of the parameter space explored, of experimental proposals targeting a given half-life sensitivity [97].

The components of the $\beta\beta0\nu$-decay rate within the standard model of particle physics in Eq. (30) cover the atomic physics related to the emitted electrons—through the phase-space factor of the transition, $G^{0\nu}\,(Q, Z)$—and the structure of the initial and final nuclear states—through the NME, $M_{\rm light}^{0\nu}$. In addition, g_A represents the hadron coupling of the interaction to nucleons (protons or neutrons), which are the degrees of freedom used by many-body methods to calculate the NMEs. Nonetheless, Eq. (30) is a simplification in the sense that various components contribute to $M_{\rm light}^{0\nu}$, and they appear associated with different couplings at the nucleon level, not only g_A. These aspects are explained in detail in Sect. 4.1.

Phase-space factors are quite accurately known for all relevant nuclei used in $\beta\beta0\nu$ decay experiments [98, 99]. Figure 12 shows the corresponding values for the light-neutrino exchange mechanism. In contrast, despite recent progress, NMEs and some of their associated hadron couplings are still poorly known. In the remaining of this section, we discuss the structure of the NMEs to be calculated as well as their corresponding couplings. Further, we briefly detail the many-body methods used to calculate NMEs and how to test the quality of the calculations. Finally, we review the status of NME predictions, including efforts to quantify their theoretical uncertainties.

4.1 Nuclear matrix elements: long- and short-range parts

The $\beta\beta0\nu$ decay of a nucleus is a second-order process. Therefore, the standard derivation of the $\beta\beta0\nu$ decay half-life builds on the one-body weak currents [88, 95, 100]. For leptons, the current reads

---

[22] In Eq. 30, the term $G^{0\nu}$ is expressed in $\mathrm{yr}^{-1}\cdot\mathrm{eV}^{-1}$ units. Alternatively, this equation is often written dividing $m_{\beta\beta}^2$ by the electron mass squared. In the latter case, $G^{0\nu}$ would have yr^{-1} units.

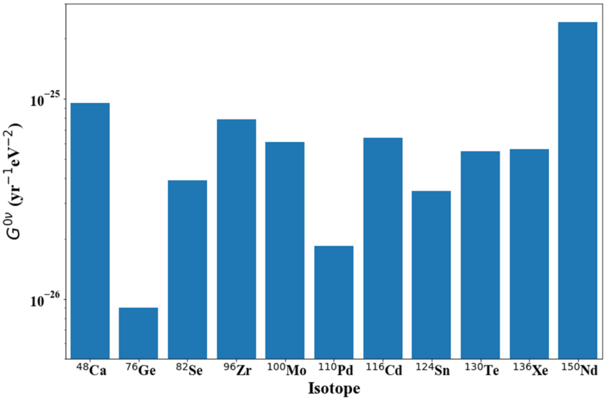

Fig. 12 Phase-space factors, $G^{0\nu}$, appearing in Eq. (30), for all 11 double-beta emitters with $Q_{\beta\beta} > 2$ MeV. Values taken from [98]

$$j_{L\mu} = \bar{e}\gamma_\mu (1 - \gamma_5)\, \nu_{eL}, \qquad \nu_{eL} = \sum_i U_{ei} \nu_{iL}, \tag{31}$$

while for hadrons, it is

$$J_L^{\mu\dagger} = \langle p|\, \tau^- \left[g_V(p^2)\gamma^\mu + i g_M(p^2) \frac{\sigma^{\mu\nu}}{2m_N} p_\nu - g_A(p^2)\gamma^\mu\gamma_5 - g_P(p^2) p^\mu \gamma_5 \right] |n\rangle, \tag{32}$$

with vector, magnetic, axial-vector, and pseudoscalar contributions. Nucleons in nuclei are non-relativistic, and therefore, the one-nucleon current can be expanded to

$$\begin{aligned} J^0_{L,1} &= \left[g_V\left(p^2\right)\right] \tau_1^-, \\ \boldsymbol{J}_{L,1} &= \left[g_A\left(p^2\right)\boldsymbol{\sigma}_1 - g_P\left(p^2\right)\frac{\boldsymbol{p}\,(\boldsymbol{p}\cdot\boldsymbol{\sigma}_1)}{p^2 + m_\pi^2} + i g_M\left(p^2\right)\frac{\boldsymbol{\sigma}_1 \times \boldsymbol{p}}{2m_N}\right] \tau_1^-, \end{aligned} \tag{33}$$

where the vector coupling $g_V(0) = 1$ is responsible for Fermi-type β decays and the axial coupling $g_A(0) = 1.27$ drives Gamow–Teller β decays. For $\beta\beta0\nu$ decay, it is important to take into account the momentum transfer dependence of these couplings, usually parameterized as a dipole, $g_{A/V}\left(p^2\right) = g_{A/V}(0)/(1 + p^2/\Lambda^2_{A/V})^2$, with $\Lambda_{A/V} \simeq 1$ GeV. The pseudoscalar term is also quite relevant, because its coupling, assuming the Goldberger–Treiman relation, is $g_P\left(p^2\right) = g_A(p^2)$ neglecting corrections of about 1%. The smallest contribution comes from the magnetic coupling term, with $g_M(0) = 4.71$. This term is usually regularized also with a dipole with parameter Λ_V.

However, nucleons are composite particles of quarks and gluons, the fundamental degrees of freedom of the underlying theory of the strong force, quantum chromodynamics (QCD). Therefore, two-nucleon currents are needed to complement the one-nucleon one in Eq. (33). Two-body currents introduce the coupling of an external

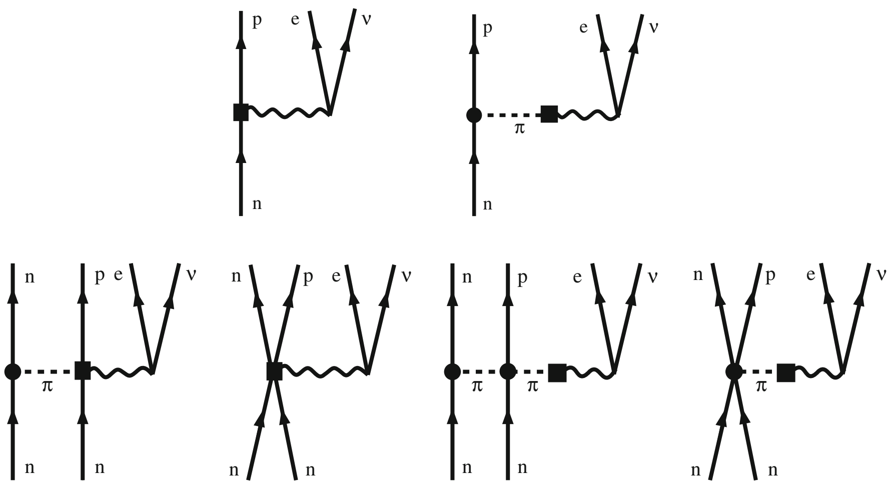

Fig. 13 Diagrams for one-nucleon weak-interaction currents (top) and leading two-nucleon weak-interaction currents (bottom). Solid lines represent nucleons, dashed lines indicate pions, and wavy lines the mediator (W boson). In all cases, only one nucleon (n) turns into a proton (p). The currents with mediator coupling to the pion involve finite momentum transfer, and they are negligible for β decay but contribute to $\beta\beta0\nu$ decay

probe to two interacting nucleons. Even though they have been recognized for several decades, the relevant two-nucleon diagrams and the value of the corresponding couplings remained with large uncertainties [101, 102], until recently.

A key step forward arrived with the development of chiral effective field theory (EFT), an effective theory of QCD valid at nuclear structure energies and momenta of the scale of the pion mass, m_π [103]. Chiral EFT provides a systematic expansion of nuclear forces [104, 105] in terms of nucleons interacting via pion exchanges—the physics included explicitly in the EFT—and contact interactions—which encode the unresolved high-energy physics. Likewise, chiral EFT provides an expansion for the interaction of nucleons with external probes, in particular via the vector and axial currents that enter the weak interaction. Chiral EFT currents also involve pion exchanges and contact interactions. The top diagrams in Fig. 13 show the leading one-nucleon currents, which include the leading g_V and g_A terms (top left diagrams) and the g_P one (top right diagram). These three contributions appear at leading order in chiral EFT. This is consistent with their similar importance for processes with $p \sim m_\pi$ in Eq. (33). The magnetic term appears at higher order in chiral EFT, which explains why this term is numerically smaller than the rest in Eq. (33).

In addition, chiral EFT predicts the leading two-nucleon diagrams that correct one-nucleon currents, indicated in the bottom part of Fig. 13. For $\beta\beta0\nu$ decay, the leading two-nucleon current is the axial one, given by [106–108]

$$\boldsymbol{J}_{A,12} = -\frac{g_A}{F_\pi^2}\,[\tau_1 \times \tau_2]^- \left[c_4\left(1 - \frac{\boldsymbol{p}}{p^2 + m_\pi^2}\,\boldsymbol{p}\cdot\right)(\boldsymbol{\sigma}_1 \times \boldsymbol{k}_2) + \frac{c_6}{4}(\boldsymbol{\sigma}_1 \times \boldsymbol{p})\right]\frac{\boldsymbol{\sigma}_2 \cdot \boldsymbol{k}_2}{m_\pi^2 + k_2^2}$$

$$
\begin{aligned}
&-\frac{2g_A}{F_\pi^2}\,\tau_2^-\left[c_3\Big(1-\frac{\boldsymbol{p}}{p^2+m_\pi^2}\,\boldsymbol{p}\cdot\Big)\,\boldsymbol{k}_2+2c_1m_\pi^2\,\frac{\boldsymbol{p}}{p^2+m_\pi^2}\right]\frac{\boldsymbol{\sigma}_2\cdot\boldsymbol{k}_2}{m_\pi^2+k_2^2}\\
&-2d_1\,\tau_1^-\Big(1-\frac{\boldsymbol{p}}{p^2+m_\pi^2}\,\boldsymbol{p}\cdot\Big)\boldsymbol{\sigma}_1+(1\longleftrightarrow 2)\\
&-2d_2(\tau_1\times\tau_2)^-(\boldsymbol{\sigma}_1\times\boldsymbol{\sigma}_2)\Big(1-\cdot\,\boldsymbol{p}\,\frac{\boldsymbol{p}}{p^2+m_\pi^2}\Big),
\end{aligned}
\tag{34}
$$

where the final and initial momenta of the nucleons are $\boldsymbol{k}_i=\boldsymbol{p}_i'-\boldsymbol{p}_i$, $\boldsymbol{p}=-\boldsymbol{k}_1-\boldsymbol{k}_2$, and c_i and d_i are couplings of the EFT that need to be determined by fitting to data or from lattice QCD calculations. The terms proportional to the c_i's correspond to the pion-exchange nucleon diagrams in Fig. 13, while those with short-range nucleon interactions enter with the d_i's. Since the chiral EFT couplings also drive nuclear forces, once these are fit, the two-nucleon current in Eq. (34) is entirely predicted. In $\beta\beta0\nu$, a complication arises, because the product of two-body currents leads, in general, to a four-body operator hard to handle in many-body calculations. A simple approximation but accurate in β decays [109] consists in normal-ordering the two-nucleon current with respect to a Fermi gas reference state with density ρ_F. As a result, one obtains an effective one-nucleon current [110], which just modifies the axial and pseudoscalar terms in Eq. (33) with corrections $\delta g_A(p^2, c_i, d_i, \rho_F)$ and $\delta g_P(p^2, c_i, d_i, \rho_F)$ dependent on the chiral EFT couplings [111]. So far, calculations which include two-body currents in $\beta\beta0\nu$ decay do so by assuming this approximation.

Once the weak currents are known, the standard procedure follows second-order perturbation theory to obtain the $\beta\beta0\nu$-decay rate [88]. This way, one arrives to the long-range part of the nuclear matrix element, presented in Sect. 4.1.1. However, this approach misses a relevant contribution only recognized recently [112], independent to the ones in Eqs. (33) or (34). In fact, a chiral EFT analysis shows that, without this additional term, which can be understood as the contribution of high-energy light neutrinos, the decay amplitude is not renormalizable due to the divergences induced by the long-range neutrino potential [112]. This additional term of the nuclear matrix element is introduced in Sect. 4.1.2.

4.1.1 Long-range nuclear matrix elements

Thus, there are two contributions to the $\beta\beta0\nu$-decay rate. First, the usual long-range part [95]

$$
\begin{aligned}
\sqrt{\Gamma_{0\nu\beta\beta}} =& m_{\beta\beta}\cdot\frac{g_A^2}{R}\cdot\int d\boldsymbol{x}\int d\boldsymbol{y}\; L^{\mu\rho}(\boldsymbol{x},\boldsymbol{y})\\
&\int d\boldsymbol{p}\, e^{i\boldsymbol{p}(\boldsymbol{x}-\boldsymbol{y})}\cdot\frac{R}{g_A^2}\sum_{n,m}\left\langle 0_f^+\right|\frac{J_{L,n}^{\mu\dagger}(\boldsymbol{x})\;J_{L,m}^{\rho\dagger}(\boldsymbol{y})}{p^2}\left|0_i^+\right\rangle,
\end{aligned}
\tag{35}
$$

where $R=1.2A^{1/3}$ and g_A^2 are factorized out for convenience, and $L^{\mu\rho}$ represents the electron currents. The second line in Eq. (35) defines the usual long-range NME, which can be written as

$$M^{0\nu}_{\text{long}} = \frac{R}{g_A^2} \langle 0_f^+ | \sum_{n.m} \tau_m^- \tau_n^- \frac{2}{\pi} \int \left[j_0(pr)\, h_F\left(p^2\right) \mathbb{I} + j_0(pr)\, h_{GT}\left(p^2\right) \boldsymbol{\sigma}_n \cdot \boldsymbol{\sigma}_m \right.$$
$$\left. + j_2(pr)\, h_T\left(p^2\right) S_{nm} \right] dp\, |0_i^+\rangle, \tag{36}$$

with Fermi (F), Gamow–Teller (GT) and tensor (T) spin structures, $S_{nm} = 3(\hat{r}\cdot\boldsymbol{\sigma}_n)(\hat{r}\cdot\boldsymbol{\sigma}_m) - \boldsymbol{\sigma}_n\cdot\boldsymbol{\sigma}_n$, $j_l(pr)$ spherical Bessel functions and $r = |\boldsymbol{r}_n - \boldsymbol{r}_m|$. The $h_{\text{spin}}(p^2)$ functions for the long-range NME are

$$\begin{aligned}
h_F\left(p^2\right) &= g_V^2\left(p^2\right),\\
h_{GT}\left(p^2\right) &= g_A^2\left(p^2\right)\left[1 - \frac{2}{3}\frac{p^2}{p^2+m_\pi^2} + \frac{1}{3}\frac{p^4}{\left(p^2+m_\pi^2\right)^2}\right] + g_M^2\left(p^2\right)\frac{p^2}{6m_N^2},\\
h_T\left(p^2\right) &= g_A^2\left(p^2\right)\left[\frac{2}{3}\frac{p^2}{p^2+m_\pi^2} - \frac{1}{3}\frac{p^4}{(p^2+m_\pi^2)^2}\right] + g_M^2\left(p^2\right)\frac{p^2}{12m_N^2}.
\end{aligned} \tag{37}$$

The approximate effect of two-nucleon currents using a normal-ordering approximation can be obtained by modifying the above functions with the corrections $\delta g_A(p^2, c_i, d_i, \rho_F)$ and $\delta g_P(p^2, c_i, d_i, \rho_F)$.

4.1.2 Short-range nuclear matrix elements

Second, there is a short-range contribution to the light-neutrino exchange NME, with similar form as Eq. (35) but without the neutrino propagator, $1/p^2$. This term does not stem from the product of two currents. It leads to a short-range NME with Fermi-type spin form [113]

$$M^{0\nu}_{\text{short}} = \frac{R}{g_A^2}\left\langle 0_f^+ | \sum_{n.m} \tau_m^- \tau_n^- \frac{2}{\pi} \int j_0(pr)\, h_S(p)\, p^2\, dp\, \mathbb{I}\, |0_i^+ \right\rangle, \tag{38}$$

where the function $h_S(p)$ is

$$h_S(p) = 2\, g_\nu^{\text{NN}} f(p/\Lambda_S), \tag{39}$$

with g_ν^{NN} the corresponding hadronic coupling for this term, and $f(p/\Lambda)$ a function with regulator Λ_S. Notice that g_ν^{NN} enters linearly in Eq. (39), in contrast to any other couplings in Eq. (37). This indicates that the short-range NME cannot be expressed as a product of two currents. Also, the p^2 dependence in Eq. (38) illustrates the short-range nature of this NME contribution. Overall, the NME for light-neutrino exchange in Eq. (30) is

$$M^{0\nu}_{\text{light}} = M^{0\nu}_{\text{long}} + M^{0\nu}_{\text{short}}\,. \tag{40}$$

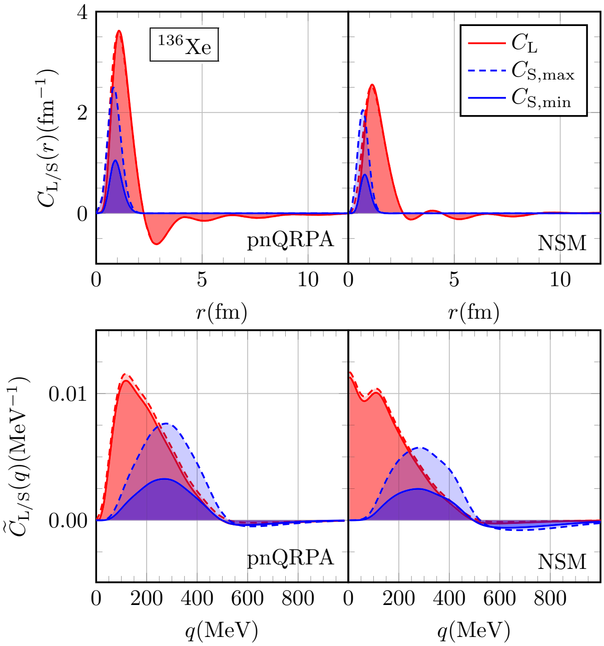

Fig. 14 Radial (top panels) and momentum (bottom panels) distributions of the two components of the $\beta\beta0\nu$-decay NME in Eq. (40), calculated for ^{136}Xe. Red (blue) regions represent the long-range (short-range) NME parts. The left panels show results for the QRPA, and right panels for the nuclear shell model (NSM). Figure with results from Ref. [119]

While the two components in Eq. (40) can be defined real, they add or cancel in the total NME according to their relative sign. From the many-body point of view, the signs of the two components are opposite, since the long-range part is dominated by the Gamow–Teller term, and the short-range part is Fermi like. In addition, one should take into account the relative sign corresponding to the dominant hadronic couplings of each component, g_A and g_ν^NN.

Unlike other hadron couplings, g_ν^NN cannot be obtained from experiment, because this would involve data on a $2n \to 2p+2e$ decay, or an equivalent process. In principle, the value of the coupling could be extracted from lattice QCD calculations, and efforts in this direction are in progress [114, 115]. For the time being, approximate QCD results based on dispersion relations [116, 117] and large number of colors [118] give consistent values for g_ν^NN with a reasonable $\sim 30\%$ uncertainty. Another strategy is to approximate g_ν^NN from the charge-symmetry breaking term of nuclear Hamiltonians [113]. This assumes that the two underlying couplings leading to g_ν^NN are the same, as only one of them can be constrained from charge-symmetry breaking. Nonetheless, all these determinations indicate that g_ν^NN carries the opposite sign than g_A, therefore, leading to an increased $\beta\beta0\nu$ rate when the two terms in (40) are combined.

Figure 14 shows the radial and momentum distributions of the long- and short-range NMEs for the decay of ^{136}Xe, calculated by the nuclear shell model and quasiparticle random-phase approximation (QRPA) methods fixing g_ν^{NN} from the charge-symmetry breaking of various Hamiltonians. The NME distributions satisfy

$$M^{0\nu}_{\mathrm{long/short}} = \int C_{L/S}(r)\, dr\,, \tag{41}$$

$$M^{0\nu}_{\mathrm{long/short}} = \int \widetilde{C}_{L/S}(p)\, dp\,. \tag{42}$$

The upper panels in Fig. 14 highlight that the short-range NME distributions, in blue, actually receive contributions from two decaying nucleons at shorter relative distances than the long-range NME ones, shown in red. Consistently, the lower panels in Fig. 14 reveal that the short-range NME are dominated by larger momentum transfers. Moreover, Fig. 14 shows that while the short-range NME is generally smaller than the long-range one, it is a sizeable correction, as expected by chiral EFT.

4.2 Different nuclear structure approaches

The nuclear structure of the initial and final nuclei in the $\beta\beta0\nu$ decay plays a relevant role in the value of the NMEs. This is because the relevant momentum transfers in $\beta\beta0\nu$ decay are of the order $p \sim 200$ MeV—see Fig. 14—comparable to the Fermi momentum, which sets the typical scale of the momenta of nucleons in nuclei. Therefore, a good description of the initial and final nuclei is a necessary condition to get reliable NMEs.

4.2.1 Tests of nuclear structure calculations and g_A quenching

All nuclear many-body methods used to study $\beta\beta0\nu$ decay make a significant effort to describe with high quality the structure of the initial and final nuclei. In particular, the low-energy spectrum and electromagnetic transitions are typically well described in shell model [120–125], energy-density functional theory [126], interacting boson model [127] and QRPA [128] calculations, and the standard approaches used to calculate NMEs. More recently, *ab initio* or first principles methods, discussed in detail in Sect. 4.2.2, have also produced NMEs. In medium-mass nuclei, ab initio methods can match the nuclear structure description of the more phenomenological approaches [129–131], while heavier systems are more challenging [131]. Nuclear structure data are very useful to improve many-body calculations, and therefore NME predictions. Notable examples are nucleon-removal and -addition [132–134] and charge-exchange [135] reactions involving initial and final $\beta\beta$ nuclei. Novel nuclear structure data keep testing calculations. For instance, a recent measurement of the low-energy spectrum of ^{136}Cs favors particular shell-model Hamiltonians [136]. In addition, correlation between $\beta\beta0\nu$-decay and other observables can provide insights to the $\beta\beta0\nu$-decay NMEs: good theoretical correlations have been found with double Gamow–Teller [137–139], second-order electromagnetic [139, 140], and $\beta\beta2\nu$-decay matrix elements [141].

However, most calculations systematically overestimate β-decay Gamow–Teller matrix elements. This puzzle is sometimes coined as g_A *quenching*, because matrix elements enter the half-life multiplied by the coupling g_A

$$\left(T^{\beta}_{1/2}\right)^{-1} = G_{\beta}\left(g_A\, M^{\beta}_{GT}\right)^{2}\,, \tag{43}$$

and the disagreement could also be solved by a reduced g_A value. Fortunately, a simple correction to the β-decay matrix elements suffices to reach good agreement with data. In shell-model calculations for nuclei with mass number $A \sim 10-50$, the matrix-element reduction is captured by constant *quenching* factors $q \sim 0.7-0.8$ [142–144]. Once this factor is known from β decays, calculated Gamow–Teller strength distributions agree well with measured values from charge-exchange reactions. Moreover, shell-model half-life predictions for the $\beta\beta2\nu$ decay of ^{48}Ca [145, 146] and the 2ν double-electron capture of ^{124}Xe [147] anticipated the subsequent measured values [41, 44]. The interacting boson model and QRPA also overestimate Gamow–Teller matrix elements [148, 149]. The latter, however, by an amount depending on the strength of the proton-neutron pairing interaction used.

Nonetheless, the phenomenological quenching correction, while useful, does not pinpoint the origin of the deficiency in the many-body calculations. A proper answer is given by ab initio methods. These approaches describe the low-energy properties of light systems with $A \lesssim 14$ extremely well, including β-decay half-lives without any adjustments [109, 150]. There are two main aspects that ab initio methods incorporate, but others do not: first, additional nuclear correlations due to the more sophisticated many-body approach; second, two-nucleon currents, introduced in Sect. 4.1. In $A \lesssim 14$ nuclei, nuclear correlations are the main aspect to describe well β decays [150, 151], while in heavier systems with $A \sim 50-100$ [109], both nuclear correlations and two-nucleon currents are needed to reproduce data without any quenching factor. Due to their ability to capture complex correlations and the successful description of β decays, ab initio methods promise reliable $\beta\beta0\nu$ NMEs.

4.2.2 Ab initio methods

Ab initio or first principles nuclear structure studies have experienced an exponential boost over the last decade [152, 153]. In contrast to other many-body approaches which have some phenomenological components, ab initio methods consider all nucleons in the nucleus and use unadjusted nuclear Hamiltonians—in most cases derived from chiral EFT. Moreover, the calculations are systematically improvable and the convergence of the results can be checked explicitly.

Since $\beta\beta0\nu$ searches focus on relatively heavy isotopes, ab initio methods like quantum Monte Carlo or the no-core shell model, whose computational cost scales exponentially with the number of nucleons, are limited to benchmark NMEs in light nuclei not relevant for experiments [129, 154, 155]. Nonetheless, benchmarks are key to test other approaches suitable for heavier systems.

Three ab initio methods have been used to study the $\beta\beta0\nu$ decay of ^{48}Ca. Two of them are versions of the in-medium similarity renormalization group (IMSRG), which is based on unitary transformations that bring the many-body Schrödinger equation to a more convenient form [156]. Operators such as the $\beta\beta0\nu$-decay one transform consistently, a feature missed by other many-body methods because of their phenomenological character. The first ab initio NME calculation used the in-medium generalized coordinate method (IM-GCM) [129]. This variant considers various reference states, as the initial and final $\beta\beta 0\nu$ decay nuclei are different, and then includes additional nuclear correlations, exploring deformation or proton–nucleon pairing via the GCM.

The second is the related valence-space IMSRG (VS-IMSRG) method, which performs IMSRG transformations that decouple a valence space from the core and high-energy orbitals of the full space [157]. That is, the VS-IMSRG transforms the many-body problem into one that can be solved with standard nuclear shell-model techniques, with the advantage that it provides an unadjusted nuclear Hamiltonian and a consistent $\beta\beta 0\nu$-decay operator.

The third is the coupled clusters (CC) approach, which adds singles (one-particle–one-hole like), doubles (two-particle–two-hole), or triples correlations on top of a reference state, which needs to be a reasonable approximation to the nucleus of study [158]. Only recently, the CC has been extended to deformed nuclei such as ^{48}Ti, because the breaking of rotational symmetry is computationally expensive [130].

The IM-GCM, VS-IMSRG, and coupled clusters long-range NMEs for ^{48}Ca agree within the uncertainties of each many-body method (green bands in Fig. 15). Moreover, because of the connection to the shell model, the VS-IMSRG predicts NMEs for most relevant $\beta\beta$ nuclei; see Figs. 15 and 16. For these results, the theoretical uncertainties are dominated by the use of various chiral EFT Hamiltonians. Unlike β-decay calculations, ab initio $\beta\beta 0\nu$-decay NMEs do not include two-nucleon currents yet, because they are more challenging to implement for finite momentum transfer.

4.2.3 Many-body approaches for heavy nuclei

Among other methods, the nuclear shell model is one of the main workhorses of nuclear structure [175–177]. It solves the many-body problem in a configuration space around the Fermi surface, using Hamiltonians with a phenomenological component—in contrast to the VS-IMSRG. Two strategies quantify shell-model NME uncertainties. First, a statistical variation of all elements of shell-model Hamiltonians to obtain NME density distributions for ^{48}Ca and ^{136}Xe [171, 172] (gray bars in Fig. 15). Second, systematic calculations in dozens of nuclei exploiting the correlation between $\beta\beta 0\nu$ and $\beta\beta 2\nu$ NMEs, and $\beta\beta 2\nu$ data [141] (black bars in Fig. 15, which include normal-ordered two-body currents). The two $\beta\beta 0\nu$ NME extend the range of previous shell-model NMEs (gray symbols).

A hybrid approach can introduce into the shell model additional correlations captured by more sophisticated ab initio calculations. In particular, the generalized contact formalism [178] combines the short-range correlations captured by the quantum Monte Carlo approach with the shell model [173]. As a result, NMEs are reduced (brown bars in Fig. 15) by a larger amount than previous short-range correlations' parameterization [179].

The QRPA works in a larger configuration space than the nuclear shell model, albeit with limited nuclear correlations. Most calculations use a spherical QRPA on top of G-matrices [163, 164], but they can accommodate deformation [166] or energy-density

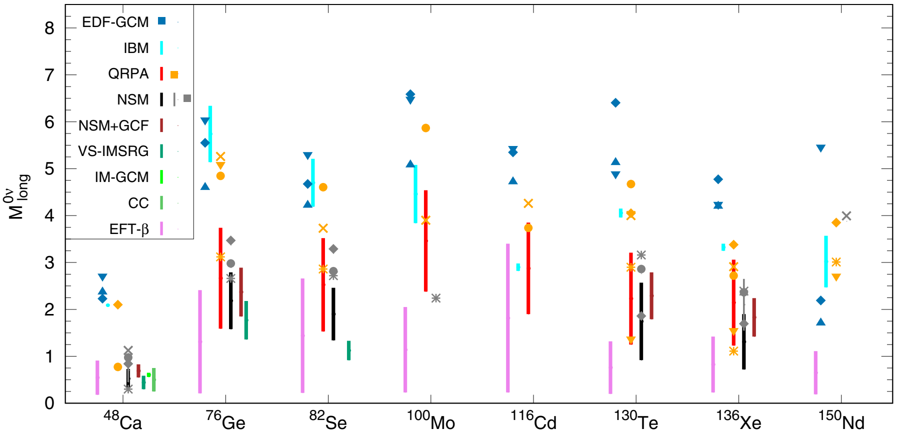

Fig. 15 Comparison of the long-range part of the $\beta\beta0\nu$-decay NME for the light-neutrino exchange mechanism, calculated by different many-body methods. For the same method, different symbols indicate results obtained by different groups with different assumptions. Results obtained with energy-density functional theory plus the GCM [159–161] (EDF-GCM, dark blue symbols), the interacting boson model [148, 162] (IBM, cyan bars), the QRPA [141, 163–169] (orange symbols and red bars), the nuclear shell model [121–125, 141, 170–172] (NSM, gray bars and symbols and black bars), the NSM complemented with the generalized contact formalism [173] (NSM+GCM, brown bars), the IM-GCM [129], and VS-IMSRG [131] (dark- and light-green bars, respectively), the coupled clusters' method [130] (CC, green bar), and an EFT of β decay [174] (EFT-β, violet bars). See the text for the differences between the calculations and for an explanation of the error bars of each method

functionals [165]. The QRPA NME uncertainty has been explored with systematic calculations varying the proton–neutron pairing interaction and using the $\beta\beta0\nu$–$\beta\beta2\nu$ NME correlation [141] (red bars in Fig. 15). The corresponding NME range is smaller than other QRPA values (orange symbols) because of including normal-ordered two-body currents.

Energy-density functional theory combined with the GCM is the other workhorse of nuclear structure studies, especially for heavy nuclei or high-energy excitations [180, 181]. Different calculations use non-relativistic [159, 160] or relativistic [161] functionals (dark blue symbols in Fig. 15).

The interacting boson model is an algebraic approach assuming nuclei formed by bosons [182] coupled to different angular momenta. Boson degrees of freedom are then mapped to fermions. For NMEs, the uncertainties explored comprise two interacting boson model Hamiltonians fitted to different properties of the initial and final nuclei [148, 162] (cyan bars in Fig. 15).

Finally, $\beta\beta0\nu$ decay can be studied by a nuclear effective theory for β and $\beta\beta$ decays, which considers spherical nuclei with nucleon particles or holes attached [174, 183]. The coupling of the EFT is fitted using the shell-model $\beta\beta0\nu$–$\beta\beta2\nu$ NME correlation [137], as the EFT can predict $\beta\beta2\nu$ NMEs. The theoretical uncertainties are predicted by the EFT, with the violet bars in Fig. 15 showing leading-order uncertainties.

4.3 Nuclear matrix elements with theoretical uncertainties

Figure 15 compares predictions for the long-range part of the $\beta\beta0\nu$-decay NME from all nuclear many-body methods discussed in Sects. 4.2.2 and 4.2.3. These sections also explain in detail the meaning of the error bars in Fig. 15 for each many-body calculation. We note that all theoretical uncertainties are underestimated, being the one for the EFT for β decay the one closer to the complete error—however, these NMEs are also based on shell-model NME correlations; see Sect. 4.2.3.

Most predicted NME values cluster around $M^{0\nu}_{\rm long} \sim 1-3$ for the majority of isotopes. These are similar as, or even smaller values than, the lower end NMEs available a decade ago [184], which roughly correspond to the shell-model results in Fig. 15 (gray symbols and bars). *This reduction in the NME values appears, because many of the recent calculations address, at least partly, the causes of the g_A quenching in β decays.* Therefore, a significant part of the reduction of the NME values due to this issue is expected to be already captured in the NMEs shown in Fig. 15 which can thus be combined with the bare g_A value to predict $\beta\beta0\nu$ rates.

That is, modern calculations that bring additional aspects, in the form of ab initio NME results (green bars with three different tones), short-range correlations introduced by the generalized contact formalism (brown bars), normal-ordered two-nucleon currents (black and red bars), and the EFT for β decay (violet bars) all suggest relatively small NME values. This is especially clear for the ^{48}Ca long-range NME, where the three different ab initio and several other methods agree within uncertainties. Only energy-density functional GCM and interacting boson results (dark blue symbols and cyan bars) point to relatively large NME values, for ^{48}Ca and for other isotopes. The latter results, however, may be overestimated because of not including explicit proton–neutron pairing correlations or high-seniority components [185–187]. Some QRPA NMEs without two-nucleon currents (orange symbols) also prefer larger NME values than most many-body methods.

However, Eq. (40) indicates that the NMEs shown in Fig. 15 are only a part of the total NMEs for $\beta\beta0\nu$ decay mediated by the light-neutrino exchange. More complete calculations, therefore, must take into account the short-range part of the NMEs as well. Figure 16 compares the predictions for the total NMEs of the few many-body methods which so far have performed dedicated short-range NME calculations. Like in Fig. 15, the total NMEs in Fig. 16 include part of the causes responsible for the g_A quenching in β decays, especially the additional correlations introduced by ab initio methods or the two-nucleon currents included into the shell model and QRPA results. Therefore, the bare g_A value can be used to obtain the corresponding $\beta\beta0\nu$ rates.

Light- and dark-green bars in Fig. 16 show ab initio IM-GCM and VS-IMSRG NMEs, which include nuclear correlations key to reproduce β-decay data. The small IM-GCM uncertainty bar in ^{48}Ca only takes into account the error due to the short-range coupling $g_\nu^{\rm NN}$, while the larger VS-IMSRG bars in heavy nuclei are dominated by the uncertainties due to three nuclear Hamiltonians used. The better estimated theoretical uncertainty corresponds to the ab initio result for ^{76}Ge [189], which explores a very comprehensive set of nuclear Hamiltonians. Two of the other results in Fig. 16 incorporate missing aspects to standard shell-model calculations, either short-range

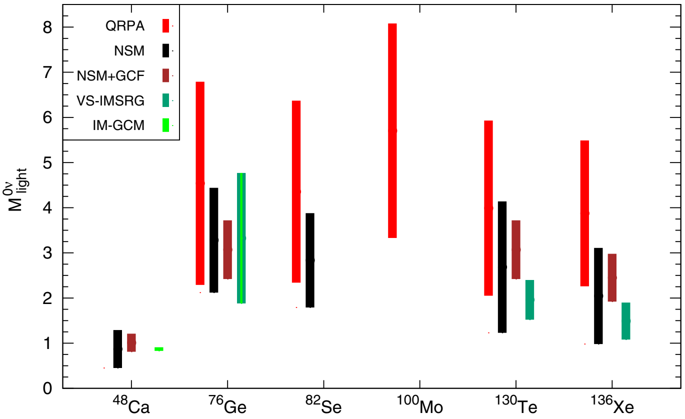

Fig. 16 Comparison of the full $\beta\beta0\nu$-decay NME for the light-neutrino exchange mechanism, calculated with different many-body methods: the QRPA [141] (red bars), nuclear shell model (NSM, black bars) [141], NSM with generalized contact formalism [173] (NSM+GCF, brown bars), VS-IMSRG [188, 189] (dark-green bars), and IM-GCM [189, 190] (light-green bar). The light–dark-green bar for ^{76}Ge covers results from the VS-IMSRG and IM-GCM. The color code is the same as in Fig. 15. See the text for the differences between calculations and for an explanation of the error bars of each method

physics via the generalized contact formalism (brown bars) or with normal-ordered two-nucleon currents (black bars). The latter approach has wider uncertainties, because it considers $g_\nu^{\rm NN}$ values from various nuclear Hamiltonians—this strategy has larger uncertainty than the one used by ab initio methods—and also because it is based on systematic calculations to gauge statistical shell-model uncertainties. These four kinds of calculations give consistent NME values for all available isotopes. The QRPA NMEs (red bars) are the only ones available for all isotopes relevant for next-generation experiments shown in Fig. 16. While generally consistent with other results, the QRPA NMEs extend to larger values in comparison to other approaches, including the ab initio results for ^{76}Ge, suggesting that the lower parts of the QRPA NME bands may be more reliable. Also, the QRPA results present larger uncertainties. Like in the shell model, these are dominated by systematic calculations to estimate statistical uncertainties and the value of $g_\nu^{\rm NN}$.

5 Ingredients for $\beta\beta0\nu$-decay experiments

Consider the radioactive decay law in the approximation $T_{1/2} \gg t$, where t is the exposure time. Assuming a hypothetical $\beta\beta0\nu$ process with a half-life $T^{0\nu}_{1/2}$, the expected number of $\beta\beta0\nu$ events in an experiment is given by

$$N_{\beta\beta0\nu} = \log 2 \, \frac{M_{\beta\beta} \cdot N_A}{W_{\beta\beta}} \, \frac{t}{T^{0\nu}_{1/2}}, \tag{44}$$

where $M_{\beta\beta}$ is the mass of the $\beta\beta$ emitting isotope,[23] N_A is the Avogadro constant and $W_{\beta\beta}$ is the molar mass of the $\beta\beta$ isotope.

Take ^{136}Xe as an example, and suppose that $T^{0\nu}_{1/2} \sim 10^{27}$ year. Assume an ideal apparatus with detection efficiency $\varepsilon = 1$ and perfect energy resolution (i.e., all $\beta\beta0\nu$ events pile up in a perfect spike at $Q_{\beta\beta}$). Such a detector has zero expected background, and then, the observation of a single event implies a discovery. Solving Eq. 44 for $N_{\beta\beta0\nu} = 1$ yields $M_{\beta\beta} \cdot t \sim 330$ kg$_{\beta\beta}$ yr. Introducing a realistic efficiency $\varepsilon \sim 0.3$–0.6, one finds $M_{\beta\beta} \cdot t \sim 0.5$–1 ton year. It follows that the first ingredient required for the next generation of $\beta\beta0\nu$ experiments is a large mass of a suitable (and always scarce) $\beta\beta$ isotope to probe in a reasonable time the extremely long half-lives expected.

In the presence of backgrounds, which we discuss in Sects. 5.1 and 5.2, the observation of a single event is not enough to establish a discovery. Imagine now that our ^{136}Xe experiment predicts a background of one event per year. Since the process is Poisson distributed, the probability of observing, say, 9 background events when 1 is expected is $\sim 10^{-6}$. Observing nine events would, therefore, establish a discovery at roughly 5σ, that is, roughly equivalent to observing one event in the absence of background. Thus, a single expected background event per year would translate in the need to increase the mass by, essentially, one order of magnitude with respect to the background-free case. The second major ingredient for $\beta\beta0\nu$ experiments, therefore, is to suppress backgrounds as much as possible, given its enormous impact on the sensitivity.

Several other factors, such as the choice of isotope, detection efficiency, or the scalability to large masses, must be taken into account as well when choosing the experimental technique. In practice, it is not possible to optimize all of these parameters simultaneously. Different choices have led to a variety of experimental approaches. To compare their discovery potential, a figure of merit, the experimental sensitivity to $m_{\beta\beta}$, is normally used. We discuss it in Sect. 5.3.

---

[23] Note that our notation in Eq. (44), and in the rest of this review, differs from the usually adopted one, derived from source-equals-detector experimental configurations. In the source-equals-detector notation, one refers to the total active mass M of the detector, which is related to the mass $M_{\beta\beta}$ of the $\beta\beta$ isotope via the following relationship:

$$M_{\beta\beta} = W_{\beta\beta} \cdot \frac{M}{W} \cdot a \cdot \eta, \tag{45}$$

where W is the molecular weight of the molecule of the active material, a is the isotopic abundance of the candidate $\beta\beta0\nu$ nuclide, and η is the number of $\beta\beta0\nu$ element nuclei per molecule of the active mass. For example, TeO$_2$ bolometric detectors with a natural isotopic abundance in ^{130}Te are characterized by $W_{\beta\beta} = 129.9$ g/mol, $W = 159.6$ g/mol, $a = 0.34167$, and $\eta = 1$, such that $M_{\beta\beta} = 0.278M$. To stress this somewhat unconventional mass notation and to avoid any confusion, we will make use in the following of kg$_{\beta\beta}$ as the mass unit to indicate one kilogram of $\beta\beta$ emitter mass. Notice that, in principle, the best quantity to express the $\beta\beta0\nu$ exposure, and the background rate per unit exposure and unit energy discussed below, is neither kg·year nor kg$_{\beta\beta}$ ·year, but rather $n_{\beta\beta}$·year, where $n_{\beta\beta} = M_{\beta\beta} \cdot N_A/W_{\beta\beta}$ is the number of moles of the $\beta\beta$ nuclide. To avoid an even more "radical" departure from commonly employed units, we stick to kg$_{\beta\beta}$ ·year units in the following.

5.1 Background sources

The background processes that can mimic a $\beta\beta0\nu$ signal are numerous. All the experiments have to deal with an intrinsic background, the $\beta\beta2\nu$ decay, that can only be distinguished by measuring the energy of the emitted electrons, since the neutrinos escape the detector undetected (see Fig. 7). Good energy resolution is, therefore, essential to prevent the $\beta\beta2\nu$ spectrum tail from spreading over the $\beta\beta0\nu$ region of interest, or to cause pileup (in the case of isotopes with a fast $\beta\beta2\nu$ mode such as ^{100}Mo, the probability of detecting two simultaneous $\beta\beta2\nu$ events in a dense crystal is not negligible, and in fact in the case of CUPID a leading cause of background).

Any process generating energy deposits in the detector's active volume of the order of the Q value of the double-beta reaction is a potential background in $\beta\beta0\nu$ searches. The background sources can be categorized by their production mechanism, as follows: radiogenic (produced by natural radioactivity), cosmogenic (produced by the action of cosmic-rays), and heliogenic (produced by the Sun). They can also be classified by their spatial origin: internal or external to the detector.

The natural radioactivity of detector components is often the main background in $\beta\beta0\nu$ experiments. Even though the half-lives of the natural decay chains are comparable to the age of the Universe, they are very short compared to the half-life sensitivity of $\beta\beta0\nu$ experiments. Therefore, even traces of these nuclides can become a significant background. The energy deposits may be produced directly by the α or β particles produced in these decays, as well as from the interactions inside the detector of the nuclear de-excitation γ rays from the daughter nuclei produced in the decay. The decays of ^{208}Tl and ^{214}Bi are particularly pernicious, given the high Q values of these reactions, therefore, polluting the energy region of interest of most $\beta\beta$ emitters. These isotopes are produced as by-products of the natural thorium and uranium decay chains (see Fig. 17), and they are present at some level in all materials. The natural radioactivity from the detector surroundings may also be relevant, if this external activity is sufficiently high. This can be the case of laboratory concrete walls and surrounding rock, for example.

Beyond primordial activity, the action of cosmic-rays on detector targets and materials may also activate isotopes that would otherwise be stable. Cosmogenic activation of materials may occur both on the surface, during production, transportation or storage, or even underground, during detector operations. While activation on the surface is mostly due to the flux of cosmic-ray neutrons reaching sea level, the one underground is due to cosmic-ray muons.[24] In the case of underground activation, cosmic-ray muon interactions can produce nuclear breakup ("spallation"), producing a cascade of fast neutrons and electromagnetic showers as a result. The neutrons eventually thermalize and get captured by other nuclei in/near the detector active volume. The resulting neutron-rich nuclei may be unstable, eventually suffering β decay, producing both electrons and gamma rays. This detector activity may be both prompt ($\lesssim$1 ms time delay) or delayed compared to the original muon interaction.

---

[24] A depth of a few tens of meter water equivalent (m.w.e.) is sufficient to suppress the flux of cosmic-ray nucleons.

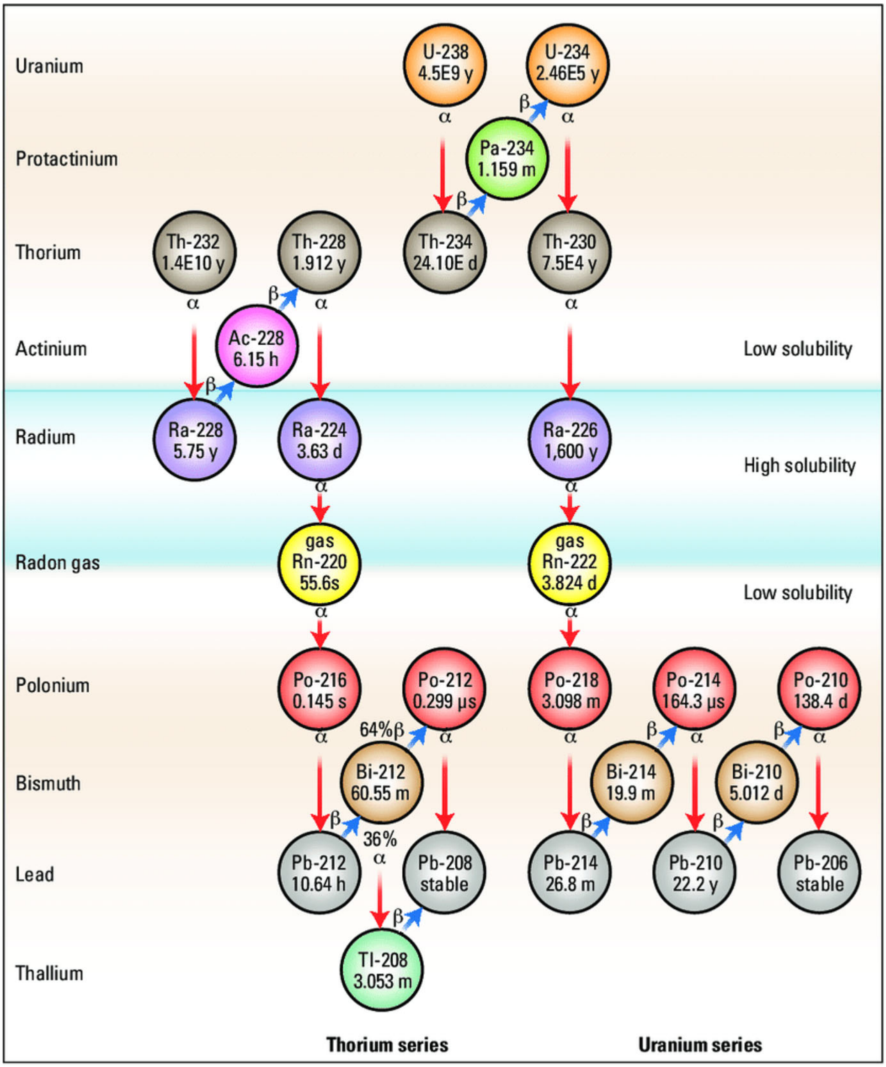
Uranium
Protactinium
Thorium
Actinium
Radium
Radon gas
Polonium
Bismuth
Lead
Thallium
U-238 4.5E9 y
U-234 2.46E5 y
Pa-234 1.159 m
Th-232 1.4E10 y
Th-228 1.912 y
Th-234 24.10E d
Th-230 7.5E4 y
Ac-228 6.15 h
Ra-228 5.75 y
Ra-224 3.63 d
Ra-226 1,600 y
gas Rn-220 55.6s
gas Rn-222 3.824 d
Po-216 0.145 s
Po-212 0.299 μs
Po-218 3.098 m
Po-214 164.3 μs
Po-210 138.4 d
Bi-212 60.55 m
Bi-214 19.9 m
Bi-210 5.012 d
Pb-212 10.64 h
Pb-208 stable
Pb-214 26.8 m
Pb-210 22.2 y
Pb-206 stable
Tl-208 3.053 m
α
β
64%β
36% α
Low solubility
High solubility
Low solubility
Thorium series
Uranium series

Fig. 17 Natural thorium (left) and uranium (right) decay chains. From [191]

At the depths of underground laboratories, the only other surviving radiation beyond cosmic-ray muons are neutrinos. Very massive detectors suffer from an irreducible external background: the solar neutrino flux. Solar neutrinos may elastically scatter (ES) off electrons in the detector medium to create single-site energy deposits in the $\beta\beta0\nu$ energy region of interest. The solar neutrino flux contributes to the background, especially when the isotope is strongly diluted in the active medium, as is the case in $\beta\beta$ isotope-loaded liquid-scintillator calorimeters. The charged-current (CC) interactions of solar neutrinos on $\beta\beta$ nuclei may also produce $\beta\beta0\nu$ backgrounds in two ways [192]. First, the CC interaction itself can produce a prompt signal given by the emitted electron and, if the resulting nucleus is in an excited state, by a number of de-excitation gamma rays. Second, a delayed signal may be produced if the resulting nucleus can undergo beta decay, emitting a single electron and possibly also gamma rays. The topologies produced by such solar neutrino CC interactions, therefore, produce multi-site signatures, generally making them a negligible background contribution compared to the solar neutrino ES interactions.

5.2 Background mitigation

All $\beta\beta0\nu$ experiments must use materials with extremely low amounts of radioactive impurities. Selection, manufacturing, cleaning, and installation of detector materials have to be conducted with extreme care, relying on radio-pure protocols at all times. Material selection is based on extensive radio-purity assays of all detector materials, using both gamma spectroscopy and mass spectrometry techniques. Cleaning of detector components is necessary to remove surface contaminants, such as dust or lubricants, from the manufacturing processes. Cleaning is carried out in detergent and acidic solutions, sometimes using ultrasonic techniques. Dedicated manufacturing processes are used to avoid contamination. Detector installation occurs in clean-room conditions. The most stringent radio-purity requirements apply to the detector active target itself, as well as to other massive detector components (e.g., shielding parts) in proximity to it. The new-generation experiments are being fabricated from amazingly radio-pure components, some with specific activities as low as 1 μBq/kg or less. Specific activities that are that low require ^{232}Th and ^{238}U impurities in the bulk materials that are below the part per trillion (ppt) level in mass, $< 10^{-12}$ g/g. Ultra-pure detector material examples include organic scintillator and xenon fluids through closed-loop re-circulation and purification systems, 2000-year-old Roman shielding lead, and fabrication of ultra-pure shielding copper via electroforming techniques.

Beyond primordial activity from contaminants in the natural decay chains, production inside detector materials of radioactive nuclides by cosmic-rays may also occur. Cosmogenic activation is, of course, more severe on surface. Therefore, for experiments using materials that can get activated (like germanium-based experiments), underground fabrication and storage of the detector components are essential.

Radon gas, particularly ^{222}Rn, is an intermediate by-product of the natural decay chains, that also needs to be suppressed inside and near $\beta\beta0\nu$ experiments. Being gaseous, radon does not stay trapped within detector components and may infiltrate inside detector sensitive regions, hence requiring a separate mitigation strategy. Also, radon daughters tend to be electrically charged and stick to surfaces. Concerning airborne radon, most deep underground laboratories have radon abatement systems capable of suppressing the radon concentration in the air by several orders of magnitude, down to 1 mBq/m^3 concentrations, providing effectively radon-free air in the vicinity of the detectors. The flushing of pure nitrogen gas is an equally effective, although more expensive, alternative to provide a radon-free environment. The radon concentration in the air is monitored in real time at underground locations. Radon may also diffuse inside fluid-based (liquid or gaseous) $\beta\beta0\nu$ detectors, typically via

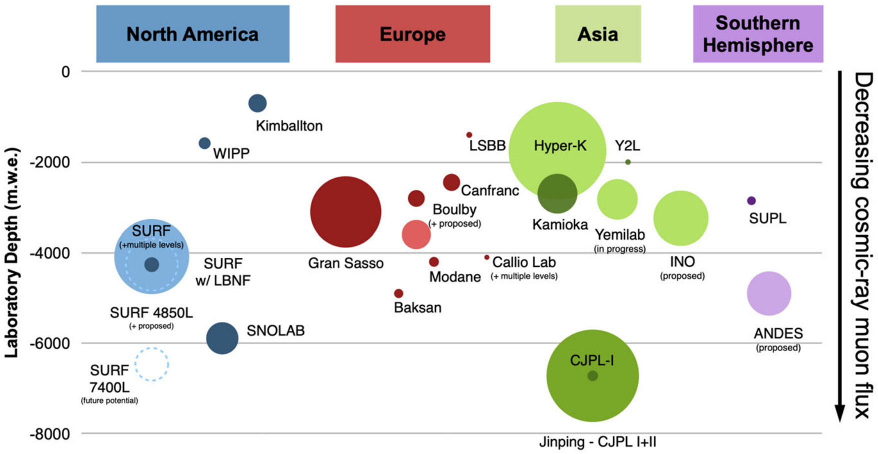

Fig. 18 Overview of underground facilities located around the world. The size (volume of science space) and effective shielding depth (total muon flux) are shown. Some muon flux values are estimated using a recent parameterization [194]. Figure from [195, 196]

emanation from detector materials. Active filtration systems (radon traps) may be used to mitigate this internal radon component.

Concerning external backgrounds originated outside the detectors, the techniques to passively mitigate them involve placing the experiments at deep underground laboratories, and by enclosing them into shielding systems.

Deep underground laboratories are research infrastructures with an overburden typically larger than 1000 ms water equivalent (m.w.e.). In general, the depth requirement for a $\beta\beta0\nu$ experiment varies according to the detector technology. A very efficient shielding and additional detection signatures such as topological information can compensate the benefits of a very deep location. Figure 18 shows the laboratory depth and size of several underground facilities currently available to host physics experiments around the world. In addition to depth, other important factors characterizing the underground sites include the size of the excavated halls available for science, and the services provided to the experiments. The size is an important factor to take into account, especially for experimental proposals at the ton-scale and beyond, given that some of them need large volumes. The most relevant deep underground laboratories for current and future $\beta\beta0\nu$ experiments, listed in order of decreasing depth, are at the moment: the China Jinping Underground Laboratory (CJPL, China), SNOLAB (Canada), the Gran Sasso National Laboratory (LNGS, Italy), the Sanford Underground Research Facility (SURF, USA), the Kamioka Observatory (Japan) and the Canfranc Underground Laboratory (LSC, Spain). For a recent review of the currently available underground facilities around the world, see reference [193].

Shielding systems surrounding the detectors are another very effective technique to passively suppress external backgrounds. As such, they are used ubiquitously in $\beta\beta0\nu$ experiments. In the design of a shielding system against external backgrounds, a *graded shielding* principle is followed: the thickness of a shield component does not need to reduce the flux below the contribution of the next inner component, with the innermost shield component selected to be the radiopurest.

Despite their sizable penetrating power, external neutrons from cosmic-ray interactions and from (α,n) reactions can be shielded with layers of hydrogenous material. On the other hand, the external γ-ray flux produced by radioactive decays in the rock of the underground cavern can be suppressed via dense, high Z, radio-pure materials such as lead and copper.

5.3 Sensitivity of a $\beta\beta0\nu$ experiment

Consider an ideal, background-free, experiment. If, after running for an exposure $M_{\beta\beta} \cdot t$, no events are observed, an upper limit on $m_{\beta\beta}$ could be reported:

$$m_{\beta\beta} = K_1 \sqrt{\frac{1}{\varepsilon \cdot M_{\beta\beta} \cdot t}}, \tag{46}$$

where K_1 is a constant that depends only on the isotope type, and on the details of the statistical method (and the confidence level) chosen to report such limit. In particular, neglecting factors of order unity, K_1 is given by

$$K_1 \simeq \sqrt{\frac{W_{\beta\beta}}{N_A} \cdot \frac{1}{G^{0\nu}|M^{0\nu}|^2}}. \tag{47}$$

Equations (46) and 47 follow directly from Eqs. (29) and (44); see [184] for details.

Consider now the case of an experiment with background in the limit in which the backgrounds are large enough as to follow a normal distribution, and thus, the error associated with background subtraction varies as $\sqrt{b}$. Then

$$m_{\beta\beta} = K_2 \sqrt{\frac{b^{1/2}}{\varepsilon \cdot M_{\beta\beta} \cdot t}}, \tag{48}$$

where $K_2 \simeq K_1$. If the background b is proportional to the exposure $M_{\beta\beta} \cdot t$ and to an energy window ΔE around $Q_{\beta\beta}$

$$b = c \cdot M_{\beta\beta} \cdot t \cdot \Delta E \tag{49}$$

with the background index c expressed in counts/(keV $\cdot$ kg$_{\beta\beta}$ $\cdot$ year), then

$$m_{\beta\beta} = K_2 \sqrt{1/\varepsilon} \left(\frac{c \cdot \Delta E}{M_{\beta\beta} \cdot t}\right)^{1/4} = \left(\frac{\upsilon_1^2 \upsilon_2}{\varepsilon^2}\right)^{1/4}, \tag{50}$$

where

$$\upsilon_1 = \frac{W_{\beta\beta}/N_A}{G^{0\nu}|M^{0\nu}|^2}$$

Table 3 Current best limits on the half-life of $\beta\beta0\nu$ processes for the nine studied isotopes

Isotope	$T^{0\nu}_{1/2}$ (years)	Experiment
^{48}Ca	$> 5.8 \times 10^{22}$	ELEGANT VI [197]
^{76}Ge	$> 1.8 \times 10^{26}$	GERDA [2]
^{82}Se	$> 4.6 \times 10^{24}$	CUPID-0 [8]
^{96}Zr	$> 9.2 \times 10^{21}$	NEMO-3 [54]
^{100}Mo	$> 1.8 \times 10^{24}$	CUPID-Mo [7]
^{116}Cd	$> 2.2 \times 10^{23}$	Aurora [61]
^{128}Te	$> 3.6 \times 10^{24}$	CUORE [198]
^{130}Te	$> 2.2 \times 10^{25}$	CUORE [4]
^{136}Xe	$> 2.3 \times 10^{26}$	KamLAND-Zen [6]
^{150}Nd	$> 2.0 \times 10^{22}$	NEMO-3 [71]

and

$$\upsilon_2 = \frac{c \cdot \Delta E}{M_{\beta\beta} t}.$$

The term υ_1 is related to the physical properties of the isotope (molar mass, NME, and available phase space) and is determined by the choice of the isotope. Instead, υ_2 is related to experimental aspects, such as the energy resolution, the background index, or the total exposure achieved by the experiment. Notice that the background rate per unit time and mass ($c \cdot \Delta E$) compensates exactly the exposure (thus, reducing the background rate by a factor of two is equivalent to doubling the exposure), and that the term υ_2 compensates the detector efficiency squared (thus increasing efficiency by a factor of two is equivalent to increase υ_2 by a factor of four (e.g., increasing the exposure by a factor of four keeping the background rate constant). Last but not least, observe that, in the limit of large backgrounds, the sensitivity scales with the power 1/4. This means that an increase of exposure of a factor of 16 (everything else being the same) needs to be achieved to improve the $m_{\beta\beta}$ sensitivity by a factor of two. Another way to read Eq. 50 is to assert that $\beta\beta0\nu$ experiments can only be scaled if the background level can be kept close to the "background free" regime.

5.3.1 Minimizing υ_1: molar mass, $Q_{\beta\beta}$ and NMEs

In nature, 35 naturally occurring isotopes are $\beta\beta$ emitters, but practical considerations, such as isotope abundance, as well as feasibility of procurement, purification and enrichment, dictate that only a few are suitable for $\beta\beta0\nu$ searches. Table 3 shows the best current $\beta\beta0\nu$ limits for the nine isotopes for which direct $\beta\beta2\nu$ decay direct measurements exist, and includes also a recent limit for ^{128}Te (for which a direct measurement of the two-neutrino mode remains elusive). Notice, however, that practical considerations (isotopic abundance, procurement, purity, enrichment, and cost) make unpractical the use at large scale of some of these (such as ^{48}Ca, ^{96}Zr, ^{116}Cd, and

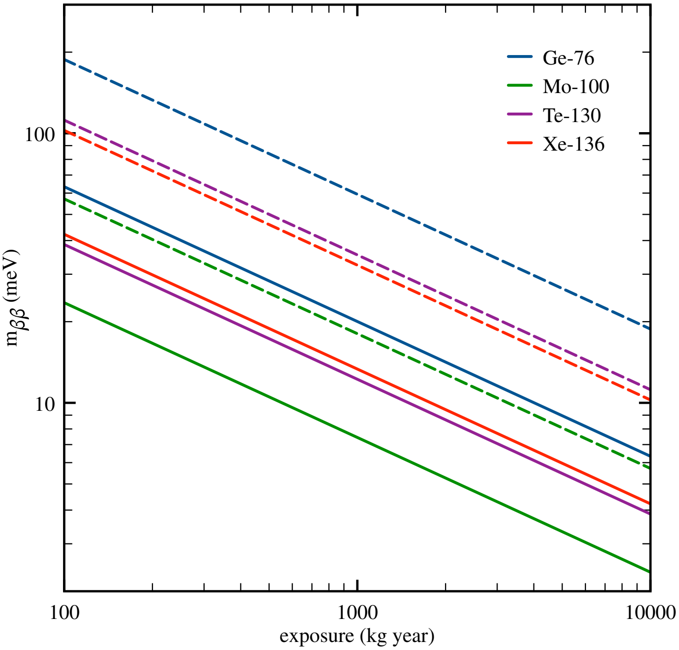

Fig. 19 Sensitivity of ideal experiments at 90% CL for different $\beta\beta$ isotopes. Solid and dashed lines of the same color indicate the limits of the QRPA NME ranges from [141]

^{150}Nd). Of the remaining isotopes, three have been used by current-generation experiments (^{76}Ge, ^{136}Xe and ^{130}Te), which have set limits to $\beta\beta0\nu$ half-lives in excess of $10^{25} - 10^{26}$ year, while ^{100}Mo has been selected for the CUPID experiment. Hereafter, we will refer to this set as Next Generation Set or NGS.

Minimizing υ_1 requires maximizing the product $G^{0\nu}|M^{0\nu}|^2$ and minimizing the molar mass. The two requirements contradict each other, since, for most isotopes, larger $Q_{\beta\beta}$ implies also larger molar mass. On the other hand, since $G^{0\nu} \sim Q^5_{\beta\beta}$ [73], isotopes with large Q-values are strongly favored. The factor $|M^{0\nu}|^2$ in υ_1 also favors strongly isotopes with larger NMEs.

As shown in Fig. 12, ^{76}Ge has the less favorable phase-space factor of the NGS (but the lightest molar mass), while the other three isotopes have similar values. Notice also that the most favorable phase-space factors (^{150}Nd and ^{48}Ca) correspond to isotopes which are not considered feasible for practical reasons. Figure 16, on the other hand, show that the values of nuclear matrix elements are rather similar for the NGS, and in fact, the uncertainty associated with the predictions of the different models is much larger than the variations between isotopes for a given set of NMEs.

Figure 19 shows the sensitivity that a ideal experiments using the four isotopes of the NGS could reach as a function of the exposure. This idealized sensitivity is in fact a measurement of υ_1, and yields similar results (differing in no more than a factor of two) for all the isotopes in the set.

5.3.2 Minimizing υ_2: isotope mass

One way to minimize υ_2 is to maximize the mass of the isotope being deployed. This requires, in turn, candidates that are isotopically abundant (such as ^{130}Te with a 34%, isotopic abundance of the $\beta\beta$ emitter) and/or, easy to enrich and purify (such as ^{136}Xe).[25] It is not surprising, therefore, that the large liquid-scintillator calorimeters have chosen those isotopes (KamLAND-Zen uses ^{136}Xe and SNO+, ^{130}Te), since both permit, with the current technology, to deploy masses in the range of the ton (in fact, the KamLAND-Zen experiment uses almost 800 kg of ^{136}Xe already). Deploying even larger masses, in the range of 10 tons, appears feasible a priori. Xenon TPCs (the future nEXO and NEXT-HD experiments) will also use ^{136}Xe, benefiting of the same advantages of the large calorimeters, e.g, the possibility of deploying large masses at relatively low cost, thanks to the economy of scale.[26]

5.3.3 Minimizing υ_2: energy resolution

Why then, choose ^{76}Ge (LEGEND) or ^{100}Mo (CUPID) for future $\beta\beta0\nu$ experiments, given the fact that the raw material will be more difficult to enrich and purify (thus more expensive, and presumably harder to produce in large quantities)? The answer to this question is energy resolution. The resolution of both KamLAND-Zen and SNO+ is of the order of 10%[27] dominated by fluctuations in the light collection of their PMTs. EXO measured a resolution of about 3 %, and nEXO expects $\simeq$2 %, while NEXT-White has measured 1% and NEXT-100, as well as NEXT-HD, expects to improve that number to 0.5−0.7 %. Instead, GERDA measured a spectacular resolution of 0.16% (3.3 ± 0.4 keV at 2039 keV [2]) and the crystals constituting the bulk of the LEGEND-200 experiment feature an even better energy resolution of 0.14% (2.9 ± 0.1 keV) (FWHM). CUPID, on the other side, will deploy crystals of lithium molybdate (LMO, $\mathrm{Li}_2^{100}\mathrm{MoO}_4$), for which the measured resolution is 0.25% (7.6 ± 0.7 keV at 3034 keV [199]). In both cases, therefore, the experiments have prioritized energy resolution over mass. Notice that both factors compensate each other in υ_2.

5.3.4 Minimizing υ_2: background index

Minimizing the background index, c, in υ_2, is the main business of $\beta\beta0\nu$ experiments. In addition to passive techniques, discussed in 5.2, active techniques, which involve detector information, are used to achieve the lowest possible background rate.

External to the detectors themselves, experiments make extensive use of active veto systems, such as liquid shields in the form of water tanks, LAr-filled cryostats, or liquid-scintillator buffers. Such shields are instrumented with Cherenkov/scintillation light detectors to tag the passage of charged particles. Plastic scintillator detectors are also often used as active veto systems against external backgrounds. Such anti-coincidence techniques, between an inner detector containing the $\beta\beta0\nu$ target and outer detectors, constitute a powerful active background mitigation technique.

---

[25] The World production of both Xenon and Tellurium is also relatively high, in the range of few hundred tons/year.

[26] The large liquid-scintillator calorimeters, as well as the xenon TPCs, are all monolithic detectors, in which the volume, and therefore the mass, scales with the cubic power of the detector effective radius, while some—but not all—of the backgrounds scale with the detector surface, which is proportional to the radius squared.

[27] Unless otherwise stated, all resolutions in this review are FWHM.

In addition to anti-coincidence requirements in space, delayed coincidences in time are also used to suppress backgrounds. This is the case for sequential radioactive decays with relatively short-lived isotopes. A prime example is ^{214}Bi-induced background suppression via the delayed ^{214}Po tag, where the ^{214}Po α decay has a 164.3 μs half-life.

Signal and background events have also different spatial distributions. Signal events are typically distributed uniformly in the detector volume. External backgrounds accumulate on, or enter from, detector surfaces. This is also exploited to suppress backgrounds via detector fiducialization.

The topological information of the energy deposits in the active volume is also used. Gamma-ray background interactions producing multi-site energy deposits, typically via multi-Compton interactions, may be readily vetoed in segmented or imaging detectors. Pulse shape analysis in individual Ge detectors is an alternative way to identify and suppress multi-site backgrounds. Low-density detectors, such as xenon gas TPCs where MeV-scale particles produce extended tracks, provide even more detailed topological information. In this case, information from the reconstructed dE/dx energy loss profiles along the track can distinguish single-electron background events from double-electron signal events.

Particle identification is another powerful background suppression handle. A notable example is α/β discrimination in scintillating bolometers. As the light yield for energy depositions induced by α and β particles of the same energy is different, the simultaneous detection of light and heat leads to an effective rejection of the α background.

Finally, a powerful handle used by both liquid-scintillator detectors (KamLAND-Zen, SNO+) and LXe TPCs (nEXO) is *self-shielding*.

The lowest background indices (c term in Eq. 49, expressed in terms of background events per unit energy, $\beta\beta$ isotope mass and exposure time) in a $\beta\beta0\nu$ experiment so far were achieved by the KamLAND-Zen (see Sect. 6.4) and GERDA (Sect. 6.1) experiments. Perhaps not surprisingly, given the importance of background suppression in $\beta\beta0\nu$ experiments, these are also the two experiments with the most stringent $\beta\beta0\nu$ half-life upper limits to date. KamLAND-Zen has achieved a background index of 1.3×10^{-4} counts/(keV $\cdot$ kg$_{\beta\beta}$ $\cdot$ year) [6], thanks to its outstanding radio-purity, self-shielding and anti-coincidence techniques. On the other hand, GERDA Phase II has achieved 6.0×10^{-4} counts/(keV $\cdot$ kg$_{\beta\beta}$ $\cdot$ year) [2], thanks to its ultra-pure crystals and pulse shape discrimination techniques.

It is interesting to compare υ_2 for both experiments. In the case of KamLAND-Zen, $M_{\beta\beta} \cdot t = 970$ kg$_{\beta\beta}$ $\cdot$year, while for GERDA $M_{\beta\beta} \cdot t \sim 127$ kg$_{\beta\beta}$ $\cdot$year. Thus, the product $c/(M_{\beta\beta} \cdot t)$ yields a factor of $(6/1.3) \cdot (970/127) = 35$ in favor of KamLAND-Zen, which is more than compensated with the ratio of resolutions $10/0.16 = 62.5$. Indeed, in spite of its relatively modest exposure, GERDA combines an excellent background index and superb resolution to obtain the best value of the figure of merit υ_2.

5.3.5 Detection efficiency

Minimizing $m_{\beta\beta}$ requires, according to Eq. (50), maximizing the detector efficiency ϵ. Notice that, when compared with the terms in υ_2, the efficiency enters as ϵ^2. To obtain the same increase in $m_{\beta\beta}$ sensitivity obtained by doubling the efficiency, the mass would have to be increased by a factor of 4, or the factor $c \cdot \Delta E$ decreased by a factor of 4.

In general, the simpler the detection scheme, the higher the detection efficiency. Homogeneous detectors, and in particular pure calorimetric approaches such as germanium diodes or bolometers, tend to have the highest total signal efficiencies, and values in excess of 75% have been obtained. Large liquid scintillators may also have relatively high efficiencies. This is especially the case when the $\beta\beta$ source is enclosed in a inner balloon surrounded by a scintillator buffer region, as in the KamLAND-Zen experiment. Also, Liquid xenon TPCs share the same advantages of the other dense, homogeneous, detectors. However, both the large liquid-scintillator calorimeters and the LXe TPCs, use a large fraction of their active mass as self-shielding. This implies, either giving away a substantial fraction of the mass (for example performing the analysis in a reduced volume close to the center of the detector in KamLAND-Zen, SNO+ or nEXO), or weighting the events in the outer shells of the detector to take into account the increased background. In both cases, one has to be careful with the definition of efficiency. Self-shielding does not come for free.

Unlike LXeTPCs, HPXeTPCs such as those being developed by NEXT do not rely on self-shielding for background reduction, but use instead particle tracking, which also comes at the expenses of a significant efficiency loss.

6 The past, present, and future of $\beta\beta 0\nu$-decay searches

The search for double-beta decay has a long history, approaching now a full century. Initially, and for decades, the field was dominated by geochemical measurements (e.g., [38]), which looked for evidence of $\beta\beta$-decay products in geologically old ($\sim 10^9$ years) minerals rich in the parent isotope. An excess of the daughter isotope over its natural concentration was interpreted as evidence for $\beta\beta$ decay (either $\beta\beta 2\nu$ or $\beta\beta 0\nu$, as the method cannot distinguish between them).

It was not until 1987 that the $\beta\beta 2\nu$ mode was directly observed in the laboratory [39, 40]. The detector employed was a fairly large (~ 1 m^3) time projection chamber with a $\beta\beta$ source (14 g of enriched ^{82}Se) deposited on a thin foil that formed the central electrode of the chamber. The trajectories of the electrons emitted from the source foil were recorded by the TPC and then analyzed to infer their energy and kinematic features. Since this initial detection, the two-neutrino mode has been directly observed for eight other isotopes in several experiments (see Table 2 for further details).

By contrast, no evidence of $\beta\beta 0\nu$ decay has been found so far. Nevertheless, the progress made in the last 2 decades in the development of ultra-low-background detection technologies has been extraordinary. The experimental goal for the next generation of experiments is the exploration of the region of half-lives up to 10^{28} year. This will, ultimately, require exposures well beyond 1 ton year and background rates lower than 1 count ton^{-1} yr^{-1}.

In this section, we review the most promising technologies for the next generation of experiments (see Table 4), summarizing the results of past experiments, their current status, and future plans. This discussion does not pretend to be exhaustive; the reader is referred to the cited publications for more details.

6.1 High-purity germanium detectors

Germanium can be enriched in the $\beta\beta$ isotope ^{76}Ge and transformed into high-purity germanium (HPGe) detectors, devices characterized by superb energy resolution and high efficiency.

HPGe detectors have a long-standing record in neutrinoless double beta decay searches, going back to the late 1960s [209, 210]. In the 1990s, the two most sensitive experiments used this technology: HEIDELBERG- MOSCOW (HM) ran in the Laboratori Nazionali del Gran Sasso (LNGS) and set a lower limit on the $\beta\beta0\nu$ half-life of ^{76}Ge of 1.9×10^{25} years (90% C.L.) [211]. However, a subset of the HM collaboration published a controversial claim of evidence for $\beta\beta0\nu$ decay [212, 213], which sparked at the time an intense debate in the community (see, for example, [214]). The International Germanium Experiment (IGEX) operated in the Homestake Mine (USA), the Laboratorio Subterráneo de Canfranc (Spain), and the Baksan Neutrino Observatory (Russia), setting a slightly worse limit than HM, $T^{0\nu}_{1/2}(^{76}\text{Ge}) \geq 1.6 \times 10^{25}$ years (90% C.L.) [215], and hence insufficient to discard the HM claim, which remained an open question for many years.

HM and IGEX were succeeded by two new experiments, the GERmanium Detector Array (GERDA) [2] and the MAJORANA DEMONSTRATOR [3], which employed novel types of HPGe devices with improved energy resolution and pulse-shape identification that offered detailed information about the topology of events through the time structure of the recorded charge signal.

GERDA, located at LNGS, operated bare HPGe detectors in a high-purity instrumented liquid argon (LAr) cryostat, which provided not only the cooling for the HPGe devices, but also served as active shielding and veto against external and internal background events. With a background index of 5.2×10^{-4} counts/(keV · kg · year) and an energy resolution of ~ 3 keV (FWHM) at $Q_{\beta\beta} = 2039$ keV [2], GERDA has been the first $\beta\beta0\nu$-decay experiment to operate in the "background-free regime" (i.e., less than one expected background count in the signal window). With a total published exposure of 127.2 $\text{kg}_{\beta\beta}$ yr, the derived lower limit on the $\beta\beta0\nu$ half-life of ^{76}Ge is 1.8×10^{26} yr (90% C.L.) [2].

The MAJORANA DEMONSTRATOR operated its HPGe detectors at the Sanford Underground Research Facility (SURF) in a high-purity shield built with electroformed copper produced deep underground. With a world-leading energy resolution of 2.52 keV (FWHM) at $Q_{\beta\beta}$ and after accumulating an exposure of 64.5 kg yr, the experiment set a half-life lower limit of 8.3×10^{25} yr (90% C.L.) [3].

Building on the success of GERDA and the MAJORANA DEMONSTRATOR, the LEGEND [200] collaboration is developing a staged $\beta\beta0\nu$-decay experimental program

Table 4 Sensitivity of the main upcoming and future $\beta\beta0\nu$-decay experiments

	Experiment	Isotope	Mass (kg$_{\beta\beta}$)	Live time (years)	Half-life (10^{28} years)	$m_{\beta\beta}$ (meV)	References
HPGe	LEGEND-200	^{76}Ge	140	5	0.100	30–89	[200]
	LEGEND-1000	^{76}Ge	910	10	1.400	8–24	[200]
Bolometers	CUORE	^{130}Te	206	5	0.095	46–132	[4]
	CUPID	^{100}Mo	253	10	0.150	8–19	[201]
	CUPID-1T	^{100}Mo	1000	10	0.910	3–8	[202]
	AMoRE-II	^{100}Mo	100	5	1.100	9–23	[203]
Xe TPCs	nEXO	^{136}Xe	4550	10	1.340	4–10	[204]
	NEXT-100	^{136}Xe	91	3	0.006	61–148	[205]
	NEXT-HD	^{136}Xe	1109	4.5	0.140	13–31	[206]
LScint	KamLAND-Zen	^{136}Xe	678	1.4	0.200	33–81	[6]
	KamLAND2-Zen	^{136}Xe	910	5	0.200	11–26	[207]
	SNO+	^{130}Te	1300	5	0.021	31–89	[208]

See main text for their description. The half-life sensitivities (at 90% C.L.) are the predictions published by the experimental collaborations for the exposure (isotope mass times live time) listed. The $m_{\beta\beta}$ sensitivities are obtained using Eq. (30), the phase-space factors from [98], and the QRPA NME ranges from [141]

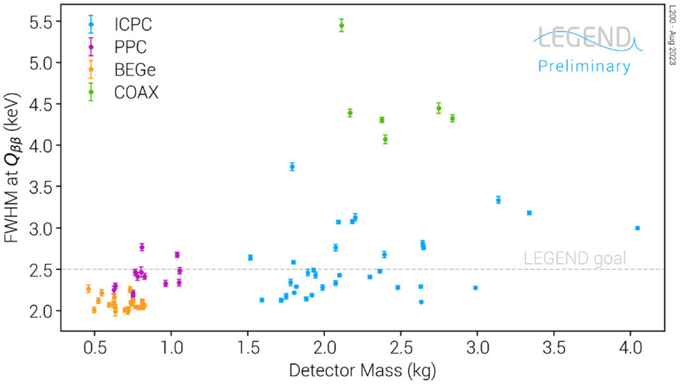

Fig. 20 Preliminary FWHM energy resolution at the ^{76}Ge Q-value for the ~ 100 HPGe detectors currently deployed in LEGEND-200. The different colors indicate different HPGe detector types. Figure from [216]

aiming at an ultimate sensitivity to the ^{76}Ge half-life beyond 10^{28} years. LEGEND will make use of new inverted-coaxial point-contact (ICPC) HPGe detectors with exceptional energy resolution (0.12% FWHM at 2039 keV) and more than a factor of two greater mass per crystal over previous experiments. As done in GERDA, the HPGe detectors will be operated immersed in LAr.

LEGEND-200, the first phase of the experiment, is operating 200 kg of germanium detectors—the existing 70 kg of enriched detectors from the MAJORANA DEMONSTRATOR and GERDA, plus an additional 130 kg of newly produced ICPC detectors—in an upgrade of the GERDA infrastructures at LNGS incorporating technologies from the MAJORANA DEMONSTRATOR. First, LEGEND-200 results related to its outstanding energy resolution are shown in Fig. 20. A reduction by a factor of 2.5 with respect to the GERDA background rate is expected, aiming at a sensitivity to the $\beta\beta0\nu$ half-life of about 10^{27} yr for an exposure of 1 ton yr. The second phase of the experiment, LEGEND-1000, has a background goal of less than 10^{-5} counts/(keV · kg · year), a 20-fold reduction with respect to LEGEND-200 expected to come from the use of underground-sourced argon (which does not contain the radioactive isotopes ^{42}Ar and its daughter ^{42}K), improvements in the radio-purity of materials and the exclusive use of ICPC HPGe detectors.

6.2 Bolometers

A bolometer for $\beta\beta0\nu$-decay searches consists of a dielectric crystal, which contains the isotope of interest, coupled to a temperature sensor. When the bolometer is cooled to very low temperatures ($<$ 20 mK for crystals with masses in the 0.1–1 kg range), the energy deposited in the crystal by interacting particles can be measured with high precision as a rise in temperature. This technique, originally proposed for rare-event searches in the early 1980s [217], can provide an energy resolution at the few per-mil level (FWHM) at 3 MeV and a total efficiency at the 70–90% level. Bolometer-based detectors—at very different scales and maturity levels—have been used to search for

$\beta\beta0\nu$ in six different nuclides (^{48}Ca, ^{82}Se, ^{100}Mo, ^{116}Cd, ^{124}Sn, and ^{130}Te) since the 1990s.

The MiDBD experiment [67] at LNGS was the first bolometric array with large-mass crystals. It consisted of 20 TeO_2 bolometers of 340 g each ($3 \times 3 \times 6$ cm^3 crystals). MiDBD proved that an energy resolution of 5 keV at the Q value was within reach, and achieved a background index of less than 1 counts/(keV · kg · year) in the region of interest around $Q_{\beta\beta}$. With a total exposure of 4.25 kg yr, MiDBD set the limit $T_{1/2}^{0\nu}(^{130}\mathrm{Te}) > 2.1 \times 10^{23}$ years at 90% CL.

CUORICINO [218], an array of 62 TeO_2 crystals, improved on the MiDBD results after running between 2003 and 2008 at LNGS, accumulating a total exposure of 19.75 kg yr. It set a lower bound on the ^{130}Te half-life of 2.8×10^{24} years at 90% CL.

The latest step in this long series of TeO_2 bolometric detectors is CUORE [4], currently taking data at LNGS and consisting of 988 bolometers with a mass of about 750 g each, corresponding to about 200 kg of ^{130}Te. So far, the experiment has set a lower limit of 2.2×10^{25} years on the half-life of ^{130}Te for an exposure of 288.8 kg yr. The background index, $(1.49 \pm 0.04) \times 10^{-2}$ counts/(keV · kg · year), is dominated by energy-degraded α particles generated by surface contamination. CUORE will continue to take data until it reaches its design ^{130}Te exposure of 1 ton yr.

Scintillating bolometers could bring an additional handle for the discrimination between signal and background [219]. In these devices, the crystal containing the isotope of interest is a scintillator, and a second auxiliary bolometer is operated close to it to register the emitted scintillation light. The simultaneous detection of heat and scintillation allows one to distinguish α particles from electrons or γ rays thanks to their different light yield and signal shape, eliminating the dominant background source observed in CUORE. This and other background reduction techniques are the subject of an intense, world-wide R&D program; for more details, see, for example, [220, 221] and references therein.

The CUPID (CUORE Upgrade with Particle IDentification) [201] project aims to improve the half-life sensitivity of CUORE by two orders of magnitude increasing the source mass and reducing the background using scintillating bolometers based on lithium molybdate (Li_2MoO_4, or LMO) crystals highly enriched in ^{100}Mo. The particle identification performance of the first CUPID detector module, exploiting the light-to-heat ratio, is shown in Fig. 21. CUPID-Mo [7], a demonstrator experiment consisting of an array of 20 Li_2MoO_4 enriched in ^{100}Mo to about 97%, was installed at the Laboratoire Souterrain de Modane (LSM), France, and collected a total exposure of 1.48 kg yr between 2019 and 2020. The scintillation light signal allowed a complete rejection of α particles, while an energy resolution of 7.7 ± 0.4 keV (FWHM) was measured at 3034 keV. This performance led to a lower limit on the $\beta\beta0\nu$ half-life of ^{100}Mo of 1.8×10^{24} years at 90% CL.

The AMoRE [203] (Advanced Mo-based Rare process Experiment) project is also searching for the $\beta\beta0\nu$ of ^{100}Mo, but using scintillating bolometers of ^{100}Mo-enriched and ^{48}Ca-depleted calcium molybdate crystals. Tests have demonstrated that $CaMoO_4$ crystals produce the brightest scintillation light among all the molybdate crystals, both at room and at cryogenic temperatures. The AMORE-pilot experiment, carried out between 2016 and 2018 utilizing six crystals with a total mass of 1.9 kg, achieved a half-life sensitivity of 3.43×10^{23} yr at 90% CL and demonstrated the fundamentals

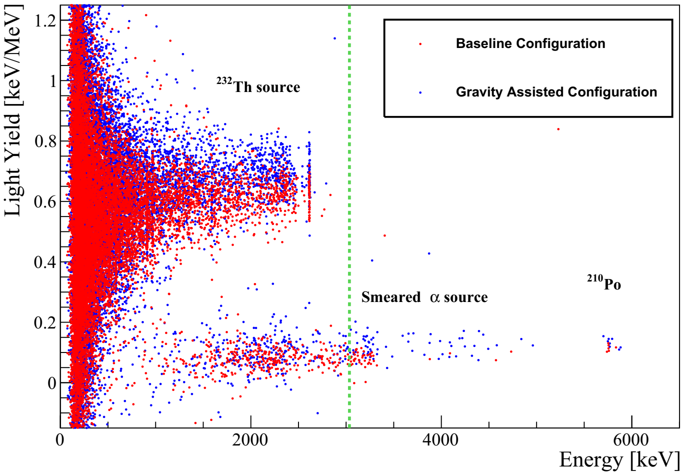

Fig. 21 Light yield per unit energy as a function of the energy deposited in the LMO crystal, for two different configurations under study as part of the CUPID detector optimization process. The green vertical line indicates the Q-value of ^{100}Mo. Taken from [222]

of the technology. The current phase of the experiment, AMoRE-I, has been running at the Yangyang Underground Laboratory (Y2L) with a 6.2 kg array of 13 Ca^{100}MoO$_4$ and five Li$_2^{100}$MoO$_4$ crystals. AMoRE-I aims at a background level of the order of 0.01 counts keV^{-1} kg^{-1} year^{-1} and a half-life sensitivity of 10^{24} years. The next phase of the experiment, AMoRE-II, will make use of a total mass of approximately 100 kg of ^{100}Mo.

6.3 Xenon time projection chambers

Two naturally occurring isotopes of xenon, ^{134}Xe and ^{136}Xe, can undergo $\beta\beta$ decay. The latter, with a higher Q value (2458 keV), is preferred for $\beta\beta 0\nu$ decay searches. It constitutes only 8.86% of natural xenon, but the enrichment process is relatively simple and cheap compared to that of other $\beta\beta$ isotopes. The two-neutrino decay mode of ^{136}Xe is slow, 2.2×10^{21} years (see Table 2), and hence, the experimental requirement for energy resolution is less severe than for other $\beta\beta$ sources. Furthermore, xenon is a suitable detection medium with strong scintillation and ionization primary signals in both its gaseous and liquid phase.

The Milano experiment [223], running at LNGS in the late 1980s, made use of a multiwire proportional chamber (MWPC) filled with 4.4 kg of xenon gas (enriched to 64% in ^{136}Xe) at a pressure of 9.5 bars. Its detection efficiency was $\sim$ 35%, the energy resolution was 4.5% FWHM at 2.5 MeV, and the background index in the energy region of interest was 11 counts/(keV · kg · year). After accumulating almost 2 kg yr of exposure, the experiment set a lower limit to the half-life of ^{136}Xe of 2.0×10^{22} years (90% CL).

The Gotthard TPC [224, 225] operated at the St. Gotthard road tunnel, Switzerland, in the 1990s. The detector was filled at a pressure of 5 atm with a 96:4 mixture of

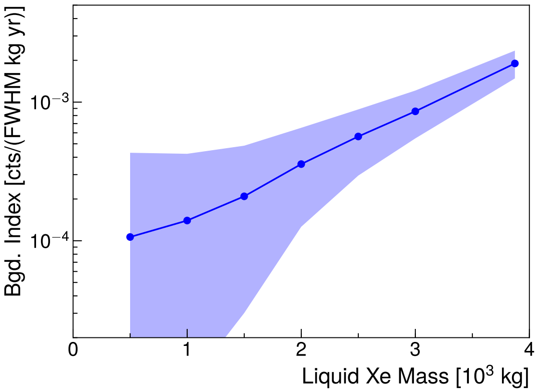

Fig. 22 Expected background index (nEXO simulation) as a function of the active mass of LXe. The plot illustrates the tradeoff in self-shielding calorimeters between background reduction and active mass. The line and the band correspond to the median background and to the 95% confidence belt of the distribution of background counts at each fiducial mass value, respectively, from toy-MC simulations with random draws of background activities and for a detector live time of 10 years. Figure from [226]

enriched xenon gas and methane; the active volume of the detector, of about 180 ls, contained 3.3 kg of ^{136}Xe. The TPC was read out with a MWPC located at the anode. The key idea of the experiment was the use of the tracking capabilities of the TPC to discriminate between signal and background events using their energy deposition pattern ($\mathrm{d}E/\mathrm{d}x$), achieving a background rejection efficiency above 98% and a background index in the region of interest of about 0.01 counts/(keV · $\mathrm{kg}_{\beta\beta}$ · year). The measured energy resolution, 6.5% FWHM at 2500 keV, was rather modest for xenon. The following limit to the $\beta\beta0\nu$-decay half-life was reported: $T^{0\nu}_{1/2} > 4.4 \times 10^{23}$ years at 90% CL.

More recently, the Enriched Xenon Observatory (EXO) searched for $\beta\beta0\nu$ using a cylindrical TPC, EXO-200, filled with about 110 kg of liquid xenon (LXe) enriched to 80.6% in ^{136}Xe [5]. The TPC consisted of two drift regions, each with a radius of 18 cm and a drift length of 20 cm, separated by a central cathode. Energy depositions in LXe produce both scintillation light and ionization. In EXO-200, the ionization charge was read out at each anode by crossed-wire planes, while the scintillation light was collected by arrays of avalanche photodiodes (APDs) located behind the wire planes. The total energy deposited was determined from the combination of the charge and light signals. The TPC was housed in a thin-walled copper vessel, and surrounded by several layers of passive and active shielding, including 50 cm of cryofluid and 25 cm of lead. A plastic scintillator muon veto surrounded the experiment on four sides. The detector operated at the Waste Isolation Pilot Plant (WIPP), in New Mexico, United Stated. The signal detection efficiency was above 96%, the energy resolution at the Q value of ^{136}Xe was 2.7% FWHM, and the measured background index in the ROI was approximately 2×10^{-3} keV^{-1} kg^{-1} yr^{-1}. After accumulating a total exposure of 234.1 kg yr, EXO-200 set a lower limit on the $\beta\beta0\nu$ half-life of ^{136}Xe of 3.5×10^{25} years at 90% CL.

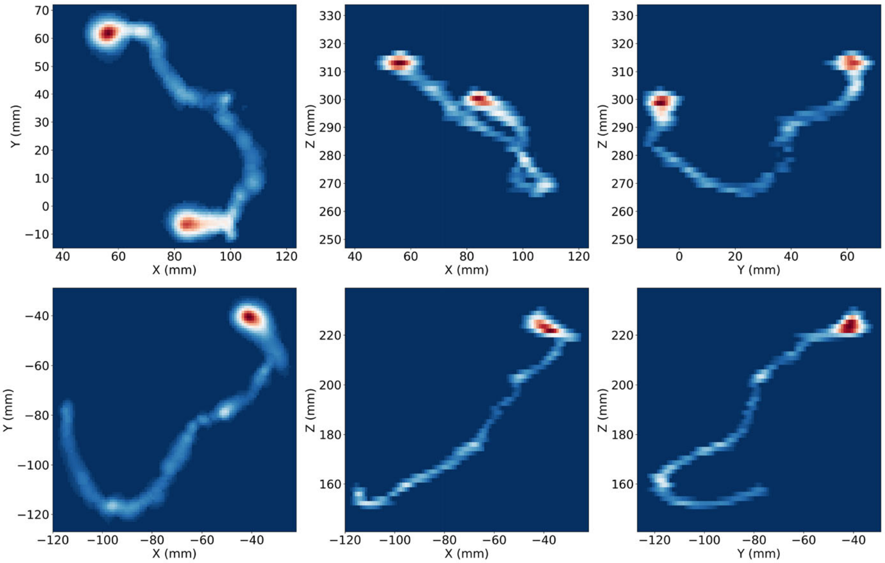

Fig. 23 Reconstruction of the trajectories of double electrons (upper row) and single electrons (lower row) produced at the ^{208}Tl double escape peak, with energies of 1.6 MeV, recorded in NEXT-White data. Two-electrons deposit energy at the end of each extreme of the track, while single electrons are characterized by a single energy blob. This feature provides a reduction in the background rate of almost two orders of magnitude. Figure from [228]

nEXO [204, 227], a follow-on to EXO-200, is a proposed next-generation experiment with an LXe TPC of 5000 kg of isotopically enriched xenon. It will consist of a single-drift cylindrical TPC 113 cm in diameter and 118 cm in length, holding an active mass of xenon close to 3650 kg. Charge will be collected at the anode with long crossed electrode strips, while a barrel of VUV-sensitive silicon photomultipliers (SiPMs) surrounding the active volume will detect the LXe scintillation light. The TPC vessel, made of copper, will be surrounded by 33 tons of cryogenic fluid, which serves as both thermal bath and radiation shield. nEXO plans to reduce the background rate achieved in EXO-200 to 7×10^{-5} counts/(FWHM · kg · yr) taking advantage of the relatively short attenuation length in LXe of γ rays of 2.5 MeV, about 8.7 cm, selecting only events occurring in the innermost 2000 kg of the TPC (see Fig. 22). The expected energy resolution of the detector is 1.9% FWHM at 2.5 MeV. This performance results in a projected half-life sensitivity of 1.35×10^{28} years at 90%CL.

NEXT [205, 206] is an international effort dedicated to the search for $\beta\beta0\nu$ decay in ^{136}Xe using high-pressure xenon gas time projection chambers (HPXeTPC) with amplification of the ionization signal by electroluminescence (EL). This detector technology takes advantage of the inherently low fluctuations in the production of ionization pairs (i.e., small Fano factor) in xenon gas to achieve an energy resolution better than 1% FWHM at $Q_{\beta\beta}$, significantly better than that of other ^{136}Xe-based double-beta decay experiments [229]. Moreover, the tracks left in gaseous xenon by $\beta\beta0\nu$ events have distinct features that can be used for background rejection (see Fig. 23). Over the last decade, the NEXT Collaboration has proven the performance of the HPXeTPC technology in the key parameters required for the observation of $\beta\beta0\nu$ decay, with the underground operation at the Laboratorio Subterráneo de Canfranc of NEXT-WHITE, an asymmetric, radio-pure HPXeTPC containing approximately 5 kg of xenon at 10 bar pressure. The NEXT-100 detector, scheduled to start operation in 2023, constitutes the next phase of the program. It is an asymmetric HPXeTPC containing about 100 kg of xenon (enriched at $\sim 90\%$ in ^{136}Xe) at 15 bar. NEXT-100 will reach a sensitivity of about 6×10^{25} year after a run of 3 effective years, for a predicted background index of at most 4×10^{-4} counts/(keV $\cdot$ kg $\cdot$ year). A scaled-up version of this technology, dubbed NEXT-HD, with about 1 ton of enriched xenon, could reach in less than 5 years of operation a sensitivity to the half-life of $\beta\beta0\nu$ decay better than 10^{27} years, significantly improving over current limits.

Xenon TPCs can, potentially, detect ("tag") the daughter Ba^{2+} cation emitted in the $\beta\beta0\nu$ decay of ^{136}Xe, in (delayed) coincidence with the two beta electrons, leaving the $\beta\beta2\nu$ mode as the only potential background. The possibility of barium tagging in a xenon TPC was proposed in 1991 [230] and relied on Ba^{+} fluorescence imaging using two atomic excitation levels in very low density gas. Recently, the nEXO collaboration has demonstrated the imaging and counting of individual barium atoms in solid xenon by scanning a focused laser across a solid xenon matrix deposited on a sapphire window [231]. This is a promising step for barium tagging in liquid xenon, where recombination is frequent, and the barium daughters are distributed across charge states from 0 to 2^{+} [232], with sizeable populations of neutral Ba and Ba^{+}.

In high-pressure gas, on the other hand, recombination is minimal [233], and Ba^{2+} dominates. In 2015, a promising technique to detect Ba^{2+} in a HPXeTPC, using a layer of molecular indicators was proposed [234]. The concept was further developed in [235] and spanned a vigorous R&D program within the NEXT collaboration [236, 237]. Daughter ion tagging is undoubtedly very challenging from the technical point of view, but the payoff—the potential to operate in the "background free" limit, if the $\beta\beta2\nu$ mode can be kept under control with high-energy resolution—for future $\beta\beta0\nu$ experiments aiming at sensitivities of 10^{28} year and beyond would be huge.

6.4 Loaded liquid scintillator

Large liquid-scintillator detectors, such as SNO [13], KamLAND [238], or Borexino [239], have a successful track record in low-background searches in neutrino physics. Loading them with large amounts of $\beta\beta$ isotopes represents a cost-effective way to search for neutrinoless double-beta decay. Two collaborations are pursuing this approach: KamLAND-Zen and SNO+. Both experiments are reusing the existing detector infrastructure from previous reactor and solar neutrino experiments.

The KamLAND-Zen experiment [6] is searching for the $\beta\beta0\nu$-decay of ^{136}Xe using enriched xenon dissolved in liquid scintillator, a technique first proposed in 1994 [240]. The experiment reuses the neutrino KamLAND detector, located at the Kamioka Observatory, Japan. The KamLAND-Zen detector is composed of two concentric transparent balloons. The inner one, 3.8 m diameter and fabricated from nylon film, contains 13 tons of liquid scintillator loaded with 745 kg of enriched xenon. The outer balloon, 13 m in diameter, contains 1 kiloton of pure liquid scintillator, and serves as an active shield for external gamma background as well as a detector for internal radiation from the inner balloon. Buffer oil between the outer balloon and an 18 m-diameter spherical stainless-steel containment tank shields the detector from external radiation. Scintillation light is recorded by 1325 17-in and 554 20-in photomultiplier tubes mounted on the stainless-steel tank, providing 34% solid-angle coverage. The containment tank is surrounded by a 3.2-kt water-Cherenkov outer detector. KamLAND-Zen, which has been collecting physics data since late 2011, has published a measurement of the half-life of the $\beta\beta2\nu$ decay of ^{136}Xe, 2.38 ± 0.02 (stat) $\pm\, 0.14$ (syst) $\times\, 10^{21}$ years [241], and a limit to the half-life of the $\beta\beta0\nu$ decay, 2.3×10^{26} years (90% CL) [6]. The energy resolution of the detector is 9.9% FWHM at the Q value of ^{136}Xe. The achieved background index in the region of interest is approximately 1.4×10^{-4} counts/(keV · kg · year), thanks to a tight selection cut in the fiducial volume and the identification of ^{214}Bi events via Bi-Po tagging. The collaboration is planning a future upgrade, KamLAND2-Zen, to increase the photocathode coverage and improve light collection, which would allow them to reach energy resolutions close to 5% (FWHM) at the $Q_{\beta\beta}$ value and improve their half-life sensitivity by one order of magnitude.

SNO+ [], the follow-up of the *Sudbury Neutrino Observatory* (SNO), is a multipurpose liquid-scintillator experiment housed in SNOLAB (Ontario, Canada). The detector reuses many of the components of its predecessor, replacing the heavy water by 780 tons of liquid scintillator to obtain a lower energy threshold. The detector consists of a 12 m-diameter acrylic vessel surrounded by about 9500 8-in photomultiplier tubes that provide a 54% effective photocathode coverage. The acrylic vessel is immersed in a bath of ultra-pure water that fills the remaining extent of the underground cavern, attenuating the background from external media such as the PMTs and surrounding rock. The density of the liquid scintillator (0.86 g/cm^3) being lower than that of the surrounding water leads to a large buoyant force on the acrylic vessel. To keep it in place, a hold-down rope net has been installed over the detector and anchored to the cavity floor. The ultimate physics goal of the SNO+ experiment is to conduct a search for $\beta\beta0\nu$ in ^{130}Te, which will be loaded into the liquid scintillator in the form of (non-enriched) telluric acid. A loading of 0.5%, equivalent to 1.3 tons of ^{130}Te, is planned for the first phase of the experiment. The energy resolution of the SNO+ detector is expected to be 10.5% FWHM at the Q value of ^{130}Te. Consequently, the $\beta\beta2\nu$ spectrum will be an important source of background. The expected levels of uranium and thorium in the liquid scintillator can also result in substantial activity near the $\beta\beta0\nu$ endpoint, mostly from the decays of ^{214}Bi and ^{212}Bi. Nevertheless, these can be, in principle, actively suppressed via Bi-Po α tagging. External backgrounds (not originating in the liquid scintillator) can be suppressed with a tight fiducial volume selection.

7 Conclusions

The experimental exploration of $\beta\beta0\nu$ decay has a long history (see Fig. 24). The first direct search was performed in 1948, where the half-life for $\beta\beta0\nu$ decay in ^{124}Sn was constrained to be longer than 3×10^{15} years [242]. Half a century later, in 2001,

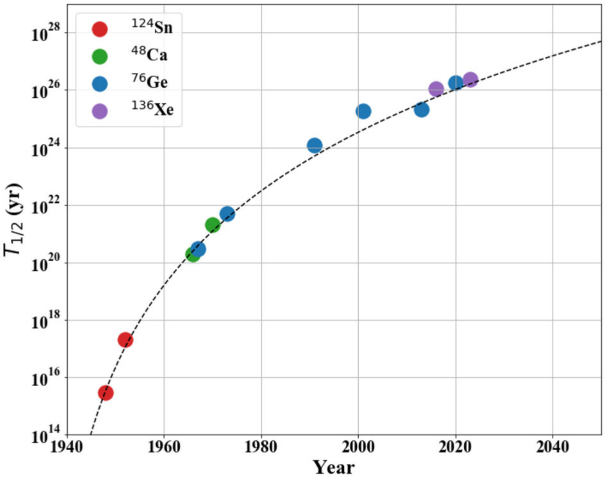

Fig. 24 Seventy-five years of direct $\beta\beta0\nu$-decay searches (1948–2023) in perspective. The plot shows the world's best half-life lower limit as a function of publication year. The different colors indicate the $\beta\beta$ emitters exploited for each limit. The dashed curve, obtained from a fit to those limits, is an attempt to forecast the sensitivity improvements of future experiments

the Heidelberg–Moscow Collaboration reported a half-life limit about ten orders of magnitude more stringent, using ^{76}Ge as $\beta\beta$ emitter: $T_{1/2}^{0\nu} > 1.9 \times 10^{25}$ years [211]. Along this history, frequent claimed discoveries have been made (see, for example, [243]) that have been later disproved by subsequent experiments. This observation alone reflects how difficult it is to search for $\beta\beta0\nu$ decay.

There is at present a diverse and healthy competition among a variety of experimental techniques to establish themselves as the best approach for $\beta\beta0\nu$ searches. The field is now witnessing a *golden age* in terms of experimental efforts. Why is that? Some reasons have been present all along during the era of $\beta\beta0\nu$-decay exploration:

- We have a fairly good idea of what to look for. While several mechanisms have been proposed to drive $\beta\beta0\nu$ decay, in most of them, the two decay electrons are the only light particles emitted, therefore carrying most of the available energy. This can be contrasted with proton decay searches, where it is less clear which decay mode should be the focus of experimental investigation.
- It is common belief that there is still ample room for improvement with respect to the most sensitive $\beta\beta0\nu$-decay searches performed to date, as can be guessed by the trend in Fig. 24.

There are, however, additional reasons that are applicable to the present era:

- Probably, the most important reason has to do with the discovery of neutrino oscillations over the past 2 decades, implying that neutrinos are massive particles. If one assumes, as it is customarily done, that light Majorana neutrino exchange is the dominant contribution to $\beta\beta0\nu$ decay, there is a direct link between a measurable $\beta\beta0\nu$ rate on the one hand, and the absolute scale of neutrino masses scale and neutrino oscillations phenomenology on the other. In this context, one can also study what is the actual value of neutrino masses, and whether the neutrino mass spectrum exhibits some particular features (such as a hierarchical or a quasi-degenerate structure), via $\beta\beta0\nu$ decay.

- Searching for $\beta\beta0\nu$ decay is well motivated on theoretical grounds. On the one hand, there is no fundamental reason why total lepton number should be conserved. On the other hand, Majorana neutrinos provide natural explanations for both the smallness of neutrino masses and the baryon asymmetry of the universe. As a consequence, theoretical prejudice in favor of Majorana neutrinos has gained widespread consensus.

The mapping of observed $\beta\beta0\nu$ rates into neutrino mass constraints not only requires assuming the standard $\beta\beta0\nu$-decay interpretation in terms of light Majorana neutrino exchange. It also requires precise nuclear physics knowledge, which can be factorized into the so-called nuclear matrix elements (NMEs). These NMEs cannot be measured directly, and need to be separately calculated for each $\beta\beta$-emitting isotope under consideration. Several calculations exist. State-of-the-art calculations give consistent results within the theoretical uncertainties estimated for each method, and somewhat lower NME values than in the past.

In this review, the different experimental aspects affecting $\beta\beta0\nu$-decay searches were extensively discussed. The requirements are often conflicting, and no new-generation experimental proposal is capable of optimizing all of them. Most likely, several experiments, using different approaches and isotopes, will set sail to explore the still huge *terra incognita* of the Majorana landscape.

Acknowledgements The authors would like to thank Stefano Gariazzo and Lotta Jonimiemi for providing us with Figs. 4 and 14, respectively. The authors acknowledge support from the European Research Council (ERC) under Grant Agreement No. 951281-BOLD; the European Union's Framework Programme for Research and Innovation Horizon 2020 (2014–2020) under Grant Agreement No. 957202-HIDDEN; the MCIN/AEI/10.13039/501100011033 of Spain, ERDF A way of making Europe and the EU (Next GenerationEU/PRTR) under Grant PID2020-118758GB-I00, Grant PID2021-125475NB, "Ramón y Cajal" Grant Nos. RYC-2017-22781 and RYC2021-033265-I, Severo Ochoa Program Grant CEX2018-000867-S and María de Maeztu Program Grant CEX2019-000918-M; the Generalitat Valenciana of Spain under Grant Nos. PROMETEO/2021/087 and CIDEGENT/2019/049. The authors would also like to thank Alessandro Bettini for useful discussions and comments on the manuscript.

Author contributions All authors contributed to the conception, drafting, critical revision and literature search for this review article.

Funding The authors acknowledge support from the European Research Council (ERC) under Grant Agreement No. 951281-BOLD; the European Union's Framework Programme for Research and Innovation Horizon 2020 (2014–2020) under Grant Agreement No. 957202-HIDDEN; the MCIN/AEI/10.13039/501100011033 of Spain, ERDF A way of making Europe and the EU (Next GenerationEU/ PRTR) under grant PID2020-118758GB-I00, Grant PID2021-125475NB, "Ramón y Cajal" grants RYC-2017-22781 and RYC2021-033265-I, Severo Ochoa Program Grant CEX2018-000867-S and María de Maeztu Program Grant CEX2019-000918-M; the Generalitat Valenciana of Spain under Grants PROMETEO/2021/087 and CIDEGENT/2019/049.

Data availability This review article contains no original research data. For reused research data, readers should refer to the publications cited throughout the text.

Declarations

Competing interests The authors have no relevant financial or non-financial interests to disclose.

Open Access This article is licensed under a Creative Commons Attribution 4.0 International License, which permits use, sharing, adaptation, distribution and reproduction in any medium or format, as long as you give appropriate credit to the original author(s) and the source, provide a link to the Creative Commons licence, and indicate if changes were made. The images or other third party material in this article are included in the article's Creative Commons licence, unless indicated otherwise in a credit line to the material. If material is not included in the article's Creative Commons licence and your intended use is not permitted by statutory regulation or exceeds the permitted use, you will need to obtain permission directly from the copyright holder. To view a copy of this licence, visit http://creativecommons.org/licenses/by/4.0/.

References

1. D. Wang, L. Kong, P. Fan, H. Chen, S. Zhu, W. Liu, L. Cao, Y. Sun, S. Du, J. Schneeloch et al., Evidence for majorana bound states in an iron-based superconductor. Science **362**(6412), 333–335 (2018)
2. M. Agostini et al., Final results of GERDA on the search for neutrinoless double-β decay. Phys. Rev. Lett. **125**(25), 252502 (2020). https://doi.org/10.1103/PhysRevLett.125.252502. arXiv:2009.06079 [nucl-ex]
3. I.J. Arnquist et al., Final result of the Majorana demonstrator's search for neutrinoless double-β decay in Ge76. Phys. Rev. Lett. **130**(6), 062501 (2023). https://doi.org/10.1103/PhysRevLett.130.062501. arXiv:2207.07638 [nucl-ex]
4. D.Q. Adams et al., Search for Majorana neutrinos exploiting millikelvin cryogenics with CUORE. Nature **604**(7904), 53–58 (2022). https://doi.org/10.1038/s41586-022-04497-4. arXiv:2104.06906 [nucl-ex]
5. G. Anton et al., Search for neutrinoless double-β decay with the complete EXO-200 dataset. Phys. Rev. Lett. **123**(16), 161802 (2019). https://doi.org/10.1103/PhysRevLett.123.161802. arXiv:1906.02723 [hep-ex]
6. S. Abe et al., Search for the Majorana nature of neutrinos in the inverted mass ordering region with KamLAND-Zen. Phys. Rev. Lett. **130**(5), 051801 (2023). https://doi.org/10.1103/PhysRevLett.130.051801. arXiv:2203.02139 [hep-ex]
7. C. Augier et al., Final results on the $0\nu\beta\beta$ decay half-life limit of ^{100}Mo from the CUPID-Mo experiment. Eur. Phys. J. C **82**(11), 1033 (2022). https://doi.org/10.1140/epjc/s10052-022-10942-5. arXiv:2202.08716 [nucl-ex]
8. O. Azzolini et al., Final result on the Neutrinoless double beta decay of ^{82}Se with CUPID-0. Phys. Rev. Lett. **129**(11), 111801 (2022). https://doi.org/10.1103/PhysRevLett.129.111801. arXiv:2206.05130 [hep-ex]
9. C. Adams et al., Demonstration of neutrinoless double beta decay searches in gaseous xenon with NEXT (2023) arXiv:2305.09435 [nucl-ex]
10. S. Dell'Oro, S. Marcocci, M. Viel, F. Vissani, Neutrinoless double beta decay: 2015 review. Adv. High Energy Phys. **2016**, 1–37 (2016). https://doi.org/10.1155/2016/2162659
11. Y. Fukuda et al., Evidence for oscillation of atmospheric neutrinos. Phys. Rev. Lett. **81**, 1562–1567 (1998). https://doi.org/10.1103/PhysRevLett.81.1562. arXiv:hep-ex/9807003
12. Q.R. Ahmad et al., Measurement of the rate of $\nu_e + d \rightarrow p + p + e^-$ interactions produced by ^{8}B solar neutrinos at the Sudbury Neutrino Observatory. Phys. Rev. Lett. **87**, 071301 (2001). https://doi.org/10.1103/PhysRevLett.87.071301. arXiv:nucl-ex/0106015
13. Q.R. Ahmad et al., Direct evidence for neutrino flavor transformation from neutral current interactions in the Sudbury Neutrino Observatory. Phys. Rev. Lett. **89**, 011301 (2002). https://doi.org/10.1103/PhysRevLett.89.011301. arXiv:nucl-ex/0204008
14. I. Esteban, M.C. Gonzalez-Garcia, M. Maltoni, T. Schwetz, A. Zhou, The fate of hints: updated global analysis of three-flavor neutrino oscillations. JHEP **09**, 178 (2020). https://doi.org/10.1007/JHEP09(2020)178. arXiv:2007.14792 [hep-ph]

15. P.F. de Salas, D.V. Forero, S. Gariazzo, P. Martínez-Miravé, O. Mena, C.A. Ternes, M. Tórtola, J.W.F. Valle, 2020 global reassessment of the neutrino oscillation picture. JHEP **02**, 071 (2021). https://doi.org/10.1007/JHEP02(2021)071. arXiv:2006.11237 [hep-ph]
16. F. Capozzi, E. Di Valentino, E. Lisi, A. Marrone, A. Melchiorri, A. Palazzo, Unfinished fabric of the three neutrino paradigm. Phys. Rev. D **104**(8), 083031 (2021). https://doi.org/10.1103/PhysRevD.104.083031. arXiv:2107.00532 [hep-ph]
17. R.L. Workman et al., Review of particle physics. PTEP **2022**, 083–01 (2022). https://doi.org/10.1093/ptep/ptac097
18. P.F. De Salas, S. Gariazzo, O. Mena, C.A. Ternes, M. Tórtola, Neutrino mass ordering from oscillations and beyond: 2018 status and future prospects. Front. Astron. Space Sci. **5**, 36 (2018). https://doi.org/10.3389/fspas.2018.00036. arXiv:1806.11051 [hep-ph]
19. J. Lesgourgues, S. Pastor, Massive neutrinos and cosmology. Phys. Rept. **429**, 307–379 (2006). https://doi.org/10.1016/j.physrep.2006.04.001. arXiv:astro-ph/0603494
20. N. Aghanim et al., Planck 2018 results. VI. Cosmological parameters. Astron. Astrophys. 641, 6 (2020). https://doi.org/10.1051/0004-6361/201833910, arXiv:1807.06209 [astro-ph.CO] [Erratum: Astron. Astrophys. 652, C4 (2021)]
21. S. Alam et al., Completed SDSS-IV extended baryon oscillation spectroscopic survey: cosmological implications from two decades of spectroscopic surveys at the apache point observatory. Phys. Rev. D **103**(8), 083533 (2021). https://doi.org/10.1103/PhysRevD.103.083533. arXiv:2007.08991 [astro-ph.CO]
22. M. Aker et al., Direct neutrino-mass measurement with sub-electronvolt sensitivity. Nat. Phys. **18**(2), 160–166 (2022). https://doi.org/10.1038/s41567-021-01463-1. arXiv:2105.08533 [hep-ex]
23. E.W. Otten, C. Weinheimer, Neutrino mass limit from tritium beta decay. Rept. Prog. Phys. **71**, 086201 (2008). https://doi.org/10.1088/0034-4885/71/8/086201. arXiv:0909.2104 [hep-ex]
24. P. Hernandez, Neutrino Physics (2010). arXiv:1010.4131 [hep-ph]
25. C. Giunti, M. Laveder, Neutrino mixing (2003). arXiv:hep-ph/0310238
26. E. Majorana, Teoria simmetrica dell'elettrone e del positrone. Nuovo Cim. **14**, 171–184 (1937). https://doi.org/10.1007/BF02961314
27. S.J. Parke, Neutrino physics today, important issues and the future. Nucl. Phys. B. Proc. Suppl. **229–232**, 14–20 (2012). https://doi.org/10.1016/j.nuclphysbps.2012.09.003
28. B. Kayser, Neutrino mass, mixing, and flavor change, 1–24 (2002). arXiv:hep-ph/0211134
29. S. Weinberg, Universal neutrino degeneracy. Phys. Rev. **128**, 1457–1473 (1962). https://doi.org/10.1103/PhysRev.128.1457
30. M.G. Betti et al., Neutrino physics with the PTOLEMY project: active neutrino properties and the light sterile case. JCAP **07**, 047 (2019). https://doi.org/10.1088/1475-7516/2019/07/047. arXiv:1902.05508 [astro-ph.CO]
31. A.J. Long, C. Lunardini, E. Sabancilar, Detecting non-relativistic cosmic neutrinos by capture on tritium: phenomenology and physics potential. JCAP **08**, 038 (2014). https://doi.org/10.1088/1475-7516/2014/08/038. arXiv:1405.7654 [hep-ph]
32. M.-C. Chen, TASI 2006 Lectures on Leptogenesis. In: Theoretical advanced study institute elementary particle physics: exploring new frontiers using colliders and neutrinos, pp. 123–176 (2007)
33. S. Davidson, E. Nardi, Y. Nir, Leptogenesis. Phys. Rept. **466**, 105–177 (2008). https://doi.org/10.1016/j.physrep.2008.06.002. arXiv:0802.2962 [hep-ph]
34. A.D. Sakharov, Violation of CP invariance, c asymmetry, and baryon asymmetry of the universe. Pisma Zh. Eksp. Teor. Fiz. **5**, 32–35 (1967). https://doi.org/10.1070/PU1991v034n05ABEH002497
35. S. Davidson, A. Ibarra, A Lower bound on the right-handed neutrino mass from leptogenesis. Phys. Lett. B **535**, 25–32 (2002). https://doi.org/10.1016/S0370-2693(02)01735-5. arXiv:hep-ph/0202239
36. A. Atre, V. Barger, T. Han, Upper bounds on lepton-number violating processes. Phys. Rev. D **71**, 113014 (2005). https://doi.org/10.1103/PhysRevD.71.113014. arXiv:hep-ph/0502163
37. M. Goeppert-Mayer, Double beta-disintegration. Phys. Rev. **48**, 512–516 (1935). https://doi.org/10.1103/PhysRev.48.512
38. M.G. Inghram, J.H. Reynolds, Double beta-decay of Te-130. Phys. Rev. **78**, 822–823 (1950). https://doi.org/10.1103/PhysRev.78.822.2
39. S.R. Elliott, A.A. Hahn, M.K. Moe, Direct evidence for two neutrino double beta decay in ^{82}Se. Phys. Rev. Lett. **59**, 2020–2023 (1987). https://doi.org/10.1103/PhysRevLett.59.2020
40. M. Moe, The first direct observation of double-beta decay. Ann. Rev. Nucl. Part. Sci. **64**, 247–267 (2014). https://doi.org/10.1146/annurev-nucl-102313-025411

41. E. Aprile et al., Observation of two-neutrino double electron capture in ^{124}Xe with XENON1T. Nature **568**(7753), 532–535 (2019). https://doi.org/10.1038/s41586-019-1124-4. arXiv:1904.11002 [nucl-ex]
42. A. Barabash, Precise half-life values for two-neutrino double-β decay: 2020 review. Universe **6**(10), 159 (2020). https://doi.org/10.3390/universe6100159. arXiv:2009.14451 [nucl-ex]
43. N. Ackerman et al., Observation of two-neutrino double-beta decay in ^{136}Xe with EXO-200. Phys. Rev. Lett. **107**, 212501 (2011). https://doi.org/10.1103/PhysRevLett.107.212501. arXiv:1108.4193 [nucl-ex]
44. A. Balysh, A.S. De Silva, V.I. Lebedev, K. Lou, M.K. Moe, M.A. Nelson, A. Piepke, A. Pronsky, M.A. Vient, P. Vogel, Double beta decay of Ca-48. Phys. Rev. Lett. **77**, 5186–5189 (1996). https://doi.org/10.1103/PhysRevLett.77.5186. arXiv:nucl-ex/9608001
45. V.B. Brudanin et al., Search for double beta decay of Ca-48 in the TGV experiment. Phys. Lett. B **495**, 63–68 (2000). https://doi.org/10.1016/S0370-2693(00)01244-2
46. R. Arnold et al., Measurement of the double-beta decay half-life and search for the neutrinoless double-beta decay of ^{48}Ca with the NEMO-3 detector. Phys. Rev. D **93**(11), 112008 (2016). https://doi.org/10.1103/PhysRevD.93.112008. arXiv:1604.01710 [hep-ex]
47. C. Dorr, H.V. Klapdor-Kleingrothaus, New Monte-Carlo simulation of the HEIDELBERG-MOSCOW double beta decay experiment. Nucl. Instrum. Meth. A **513**, 596–621 (2003). https://doi.org/10.1016/j.nima.2003.07.018
48. M. Agostini et al., Results on $\beta\beta$ decay with emission of two neutrinos or Majorons in^{76} Ge from GERDA Phase I. Eur. Phys. J. C **75**(9), 416 (2015). https://doi.org/10.1140/epjc/s10052-015-3627-y. arXiv:1501.02345 [nucl-ex]
49. R. Arnold et al., Final results on ^{82}Se double beta decay to the ground state of ^{82}Kr from the NEMO-3 experiment. Eur. Phys. J. C **78**(10), 821 (2018). https://doi.org/10.1140/epjc/s10052-018-6295-x. arXiv:1806.05553 [hep-ex]
50. O. Azzolini et al., Evidence of single state dominance in the two-neutrino double-β Decay of ^{82}Se with CUPID-0. Phys. Rev. Lett. **123**(26), 262501 (2019). https://doi.org/10.1103/PhysRevLett.123.262501. arXiv:1909.03397 [nucl-ex]
51. S.R. Elliott, A.A. Hahn, M.K. Moe, M.A. Nelson, M.A. Vient, Double beta decay of Se-82. Phys. Rev. C **46**, 1535–1537 (1992). https://doi.org/10.1103/PhysRevC.46.1535
52. R. Arnold et al., Double beta decay of Se-82. Nucl. Phys. A **636**, 209–223 (1998). https://doi.org/10.1016/S0375-9474(98)00208-5
53. R. Arnold et al., Double beta decay of Zr-96. Nucl. Phys. A **658**, 299–312 (1999). https://doi.org/10.1016/S0375-9474(99)00374-7
54. J. Argyriades et al., Measurement of the two neutrino double beta decay half-life of Zr-96 with the NEMO-3 detector. Nucl. Phys. A **847**, 168–179 (2010). https://doi.org/10.1016/j.nuclphysa.2010.07.009. arXiv:0906.2694 [nucl-ex]
55. R. Arnold et al., Detailed studies of ^{100}Mo two-neutrino double beta decay in NEMO-3. Eur. Phys. J. C **79**(5), 440 (2019). https://doi.org/10.1140/epjc/s10052-019-6948-4. arXiv:1903.08084 [nucl-ex]
56. E. Armengaud et al., Precise measurement of $2\nu\beta\beta$ decay of ^{100}Mo with the CUPID-Mo detection technology. Eur. Phys. J. C **80**(7), 674 (2020). https://doi.org/10.1140/epjc/s10052-020-8203-4. arXiv:1912.07272 [nucl-ex]
57. D. Dassie et al., Two neutrino double beta decay measurement of Mo-100. Phys. Rev. D **51**, 2090–2100 (1995). https://doi.org/10.1103/PhysRevD.51.2090
58. A.S. De Silva, M.K. Moe, M.A. Nelson, M.A. Vient, Double beta decays of Mo-100 and Nd-150. Phys. Rev. C **56**, 2451–2467 (1997). https://doi.org/10.1103/PhysRevC.56.2451. arXiv:nucl-ex/9706005
59. L. Cardani et al., First bolometric measurement of the two neutrino double beta decay of ^{100}Mo with a $ZnMoO_4$ crystals array. J. Phys. G **41**, 075204 (2014). https://doi.org/10.1088/0954-3899/41/7/075204. arXiv:1312.4680 [nucl-ex]
60. R. Arnold et al., Measurement of the $2\nu\beta\beta$ decay half-life and search for the $0\nu\beta\beta$ Decay of ^{116}Cd with the NEMO-3 detector. Phys. Rev. D **95**(1), 012007 (2017). https://doi.org/10.1103/PhysRevD.95.012007. arXiv:1610.03226 [hep-ex]
61. A.S. Barabash et al., Final results of the Aurora experiment to study 2β decay of ^{116}Cd with enriched $^{116}CdWO_4$ crystal scintillators. Phys. Rev. D **98**(9), 092007 (2018). https://doi.org/10.1103/PhysRevD.98.092007. arXiv:1811.06398 [nucl-ex]
62. H. Ejiri et al., Double beta decays of Cd-116. J. Phys. Soc. Jap. **64**, 339–343 (1995). https://doi.org/10.1143/JPSJ.64.339

63. F.A. Danevich et al., Search for 2 beta decay of cadmium and tungsten isotopes: Final results of the Solotvina experiment. Phys. Rev. C **68**, 035501 (2003). https://doi.org/10.1103/PhysRevC.68.035501
64. R. Arnold et al., Double-beta decay of Cd-116. Z. Phys. C **72**, 239–247 (1996). https://doi.org/10.1007/s002880050241
65. C. Alduino et al., Measurement of the two-neutrino double-beta decay half-life of^{130} Te with the CUORE-0 experiment. Eur. Phys. J. C **77**(1), 13 (2017). https://doi.org/10.1140/epjc/s10052-016-4498-6. arXiv:1609.01666 [nucl-ex]
66. I. Nutini et al., The CUORE detector and results. J. Low Temp. Phys. **199**(1–2), 519–528 (2020). https://doi.org/10.1007/s10909-020-02402-9
67. C. Arnaboldi et al., A calorimetric search on double beta decay of Te-130. Phys. Lett. B **557**, 167–175 (2003). https://doi.org/10.1016/S0370-2693(03)00212-0. arXiv:hep-ex/0211071
68. R. Arnold et al., Measurement of the double beta decay half-life of ^{130}Te with the NEMO-3 detector. Phys. Rev. Lett. **107**, 062504 (2011). https://doi.org/10.1103/PhysRevLett.107.062504. arXiv:1104.3716 [nucl-ex]
69. J.B. Albert et al., Improved measurement of the $2\nu\beta\beta$ half-life of ^{136}Xe with the EXO-200 detector. Phys. Rev. C **89**(1), 015502 (2014). https://doi.org/10.1103/PhysRevC.89.015502. arXiv:1306.6106 [nucl-ex]
70. A. Gando et al., Search for Majorana neutrinos near the inverted mass hierarchy region with KamLAND-Zen. Phys. Rev. Lett. **117**(8), 082503 (2016). https://doi.org/10.1103/PhysRevLett.117.082503, arXiv:1605.02889 [hep-ex]. [Addendum: Phys. Rev. Lett. 117, 109903 (2016)]
71. R. Arnold et al., Measurement of the $2\nu\beta\beta$ decay half-life of ^{150}Nd and a search for $0\nu\beta\beta$ decay processes with the full exposure from the NEMO-3 detector. Phys. Rev. D **94**(7), 072003 (2016). https://doi.org/10.1103/PhysRevD.94.072003. arXiv:1606.08494 [hep-ex]
72. W.H. Furry, On transition probabilities in double beta-disintegration. Phys. Rev. **56**, 1184–1193 (1939). https://doi.org/10.1103/PhysRev.56.1184
73. P. Vogel, Nuclear physics aspects of double beta decay. Proc. Int. Sch. Phys. Fermi **170**, 49–103 (2009). https://doi.org/10.3254/978-1-60750-038-4-49. arXiv:0807.2457 [hep-ph]
74. A.S. Barabash et al., Two neutrino double beta decay of Mo-100 to the first excited 0+ state in Ru-100. Phys. Lett. B **345**, 408–413 (1995). https://doi.org/10.1016/0370-2693(94)01657-X
75. A.S. Barabash, V.I. Umatov, R. Gurriaran, F. Hubert, P. Hubert, 2nu beta beta decay of Mo-100 to the first 0+ excited state in Ru-100. Phys. Atom. Nucl. **62**, 2039–2043 (1999)
76. M.F. Kidd, J.H. Esterline, W. Tornow, A.S. Barabash, V.I. Umatov, New results for double-beta decay of Mo-100 to excited final states of Ru-100 using the TUNL-ITEP apparatus. Nucl. Phys. A **821**, 251–261 (2009). https://doi.org/10.1016/j.nuclphysa.2009.01.082. arXiv:0902.4418 [nucl-ex]
77. R. Arnold et al., Measurement of double beta decay of Mo-100 to excited states in the NEMO 3 experiment. Nucl. Phys. A **781**, 209–226 (2007). https://doi.org/10.1016/j.nuclphysa.2006.09.021. arXiv:hep-ex/0609058
78. P. Belli et al., New observation of 2beta 2nu decay of Mo-100 to the 0+(1) level of Ru-100 in the ARMONIA experiment. Nucl. Phys. A **846**, 143–156 (2010). https://doi.org/10.1016/j.nuclphysa.2010.06.010
79. R. Arnold et al., Investigation of double beta decay of ^{100}Mo to excited states of ^{100}Ru. Nucl. Phys. A **925**, 25–36 (2014). https://doi.org/10.1016/j.nuclphysa.2014.01.008. arXiv:1402.7196 [nucl-ex]
80. C. Augier et al., New measurement of double-β decays of Mo100 to excited states of Ru100 with the CUPID-Mo experiment. Phys. Rev. C **107**(2), 025503 (2023). https://doi.org/10.1103/PhysRevC.107.025503. arXiv:2207.09577 [nucl-ex]
81. A.S. Barabash, P. Hubert, A. Nachab, V.I. Umatov, Investigation of beta beta decay in (150)Nd and (148)Nd to the excited states of daughter nuclei. Phys. Rev. C **79**, 045501 (2009). https://doi.org/10.1103/PhysRevC.79.045501. arXiv:0904.1924 [nucl-ex]
82. M.F. Kidd, J.H. Esterline, S.W. Finch, W. Tornow, Two-neutrino double-β decay of ^{150}Nd to excited final states in ^{150}Sm. Phys. Rev. C **90**(5), 055501 (2014). https://doi.org/10.1103/PhysRevC.90.055501. arXiv:1411.3755 [nucl-ex]
83. O.G. Polischuk et al., Double beta decay of ^{150}Nd to the first 0^+ excited level of ^{150}Sm. Phys. Scr. **96**(8), 085302 (2021). https://doi.org/10.1088/1402-4896/ac00a5
84. S. Eliseev et al., Resonant enhancement of neutrinoless double-electron capture in Gd-152. Phys. Rev. Lett. **106**, 052504 (2011). https://doi.org/10.1103/PhysRevLett.106.052504

85. J. Schechter, J.W.F. Valle, Neutrinoless double beta decay in SU(2) x U(1) theories. Phys. Rev. D **25**, 2951 (1982). https://doi.org/10.1103/PhysRevD.25.2951
86. M. Duerr, M. Lindner, A. Merle, On the quantitative impact of the Schechter–Valle theorem. JHEP **06**, 091 (2011). https://doi.org/10.1007/JHEP06(2011)091. arXiv:1105.0901 [hep-ph]
87. W. Rodejohann, Neutrino-less double beta decay and particle physics. Int. J. Mod. Phys. E **20**, 1833–1930 (2011). https://doi.org/10.1142/S0218301311020186. arXiv:1106.1334 [hep-ph]
88. M. Doi, T. Kotani, E. Takasugi, Double beta Decay and Majorana neutrino. Prog. Theor. Phys. Suppl. **83**, 1 (1985). https://doi.org/10.1143/PTPS.83.1
89. F. Vissani, Signal of neutrinoless double beta decay, neutrino spectrum and oscillation scenarios. JHEP **06**, 022 (1999). https://doi.org/10.1088/1126-6708/1999/06/022. arXiv:hep-ph/9906525
90. F.T. Avignone III., S.R. Elliott, J. Engel, Double beta decay, Majorana neutrinos, and neutrino mass. Rev. Mod. Phys. **80**, 481–516 (2008). https://doi.org/10.1103/RevModPhys.80.481. arXiv:0708.1033 [nucl-ex]
91. R.N. Mohapatra, Limits on the mass of the right-handed Majorana neutrino. Phys. Rev. D **34**, 909 (1986). https://doi.org/10.1103/PhysRevD.34.909
92. R.N. Mohapatra, New contributions to neutrinoless double beta decay in supersymmetric theories. Phys. Rev. D **34**, 3457–3461 (1986). https://doi.org/10.1103/PhysRevD.34.3457
93. H.M. Georgi, S.L. Glashow, S. Nussinov, Unconventional model of neutrino masses. Nucl. Phys. B **193**, 297–316 (1981). https://doi.org/10.1016/0550-3213(81)90336-9
94. R. Arnold et al., Probing new physics models of neutrinoless double beta decay with SuperNEMO. Eur. Phys. J. C **70**, 927–943 (2010). https://doi.org/10.1140/epjc/s10052-010-1481-5. arXiv:1005.1241 [hep-ex]
95. J. Engel, J. Menéndez, Status and future of nuclear matrix elements for neutrinoless double-beta decay: a review. Rept. Prog. Phys. **80**(4), 046301 (2017). https://doi.org/10.1088/1361-6633/aa5bc5. arXiv:1610.06548 [nucl-th]
96. M. Agostini, G. Benato, J.A. Detwiler, J. Menéndez, F. Vissani, Toward the discovery of matter creation with neutrinoless $\beta\beta$ decay. Rev. Mod. Phys. **95**(2), 025002 (2023). https://doi.org/10.1103/RevModPhys.95.025002. arXiv:2202.01787 [hep-ex]
97. M. Agostini, G. Benato, J.A. Detwiler, J. Menéndez, F. Vissani, Testing the inverted neutrino mass ordering with neutrinoless double-β decay. Phys. Rev. C **104**(4), 042501 (2021). https://doi.org/10.1103/PhysRevC.104.L042501. arXiv:2107.09104 [hep-ph]
98. J. Kotila, F. Iachello, Phase space factors for double-β decay. Phys. Rev. C **85**, 034316 (2012). https://doi.org/10.1103/PhysRevC.85.034316. arXiv:1209.5722 [nucl-th]
99. S. Stoica, M. Mirea, New calculations for phase space factors involved in double-β decay. Phys. Rev. C **88**(3), 037303 (2013). https://doi.org/10.1103/PhysRevC.88.037303. arXiv:1307.0290 [nucl-th]
100. T. Tomoda, Double beta decay. Rept. Prog. Phys. **54**, 53–126 (1991). https://doi.org/10.1088/0034-4885/54/1/002
101. B.A. Brown, B.H. Wildenthal, Empirically optimum M1 operator for SD-shell nuclei. Nucl. Phys. A **474**, 290–306 (1987). https://doi.org/10.1016/0375-9474(87)90619-1
102. I.S. Towner, Quenching of spin matrix elements in nuclei. Phys. Rept. **155**, 263–377 (1987). https://doi.org/10.1016/0370-1573(87)90138-4
103. E. Epelbaum, H.-W. Hammer, U.-G. Meissner, Modern theory of nuclear forces. Rev. Mod. Phys. **81**, 1773–1825 (2009). https://doi.org/10.1103/RevModPhys.81.1773. arXiv:0811.1338 [nucl-th]
104. R. Machleidt, D.R. Entem, Chiral effective field theory and nuclear forces. Phys. Rept. **503**, 1–75 (2011). https://doi.org/10.1016/j.physrep.2011.02.001. arXiv:1105.2919 [nucl-th]
105. H.-W. Hammer, A. Nogga, A. Schwenk, Three-body forces: From cold atoms to nuclei. Rev. Mod. Phys. **85**, 197 (2013). https://doi.org/10.1103/RevModPhys.85.197. arXiv:1210.4273 [nucl-th]
106. T.S. Park, L.E. Marcucci, R. Schiavilla, M. Viviani, A. Kievsky, S. Rosati, K. Kubodera, D.P. Min, M. Rho, Parameter free effective field theory calculation for the solar proton fusion and hep processes. Phys. Rev. C **67**, 055206 (2003). https://doi.org/10.1103/PhysRevC.67.055206. arXiv:nucl-th/0208055
107. H. Krebs, E. Epelbaum, U.-G. Meißner, Nuclear axial current operators to fourth order in chiral effective field theory. Ann. Phys. **378**, 317–395 (2017). https://doi.org/10.1016/j.aop.2017.01.021. arXiv:1610.03569 [nucl-th]
108. A. Baroni, L. Girlanda, S. Pastore, R. Schiavilla, M. Viviani, Nuclear axial currents in chiral effective field theory. Phys. Rev. C **93**(1), 015501 (2016). https://doi.org/10.1103/PhysRevC.93.049902.

arXiv:1509.07039 [nucl-th]. [Erratum: Phys. Rev. C 93, 049902 (2016), Erratum: Phys. Rev. C 95, 059901 (2017)]

109. P. Gysbers et al., Discrepancy between experimental and theoretical β-decay rates resolved from first principles. Nat. Phys. **15**(5), 428–431 (2019). https://doi.org/10.1038/s41567-019-0450-7. arXiv:1903.00047 [nucl-th]
110. J. Menendez, D. Gazit, A. Schwenk, Chiral two-body currents in nuclei: Gamow–Teller transitions and neutrinoless double-beta decay. Phys. Rev. Lett. **107**, 062501 (2011). https://doi.org/10.1103/PhysRevLett.107.062501. arXiv:1103.3622 [nucl-th]
111. M. Hoferichter, J. Menéndez, A. Schwenk, Coherent elastic neutrino-nucleus scattering: EFT analysis and nuclear responses. Phys. Rev. D **102**(7), 074018 (2020). https://doi.org/10.1103/PhysRevD.102.074018. arXiv:2007.08529 [hep-ph]
112. V. Cirigliano, W. Dekens, J. De Vries, M.L. Graesser, E. Mereghetti, S. Pastore, U. Van Kolck, New leading contribution to neutrinoless double-β decay. Phys. Rev. Lett. **120**(20), 202001 (2018). https://doi.org/10.1103/PhysRevLett.120.202001. arXiv:1802.10097 [hep-ph]
113. V. Cirigliano, W. Dekens, J. De Vries, M.L. Graesser, E. Mereghetti, S. Pastore, M. Piarulli, U. Van Kolck, R.B. Wiringa, Renormalized approach to neutrinoless double- β decay. Phys. Rev. C **100**(5), 055504 (2019). https://doi.org/10.1103/PhysRevC.100.055504. arXiv:1907.11254 [nucl-th]
114. Z. Davoudi, S.V. Kadam, Path from lattice QCD to the short-distance contribution to $0\nu\beta\beta$ decay with a light majorana neutrino. Phys. Rev. Lett. **126**(15), 152003 (2021). https://doi.org/10.1103/PhysRevLett.126.152003. arXiv:2012.02083 [hep-lat]
115. Z. Davoudi, S.V. Kadam, Extraction of low-energy constants of single- and double-β decays from lattice QCD: a sensitivity analysis. Phys. Rev. D **105**(9), 094502 (2022). https://doi.org/10.1103/PhysRevD.105.094502. arXiv:2111.11599 [hep-lat]
116. V. Cirigliano, W. Dekens, J. de Vries, M. Hoferichter, E. Mereghetti, Toward complete leading-order predictions for neutrinoless double β decay. Phys. Rev. Lett. **126**(17), 172002 (2021). https://doi.org/10.1103/PhysRevLett.126.172002. arXiv:2012.11602 [nucl-th]
117. V. Cirigliano, W. Dekens, J. de Vries, M. Hoferichter, E. Mereghetti, Determining the leading-order contact term in neutrinoless double β decay. JHEP **05**, 289 (2021). https://doi.org/10.1007/JHEP05(2021)289. arXiv:2102.03371 [nucl-th]
118. T.R. Richardson, M.R. Schindler, S. Pastore, R.P. Springer, Large-N_c analysis of two-nucleon neutrinoless double-β decay and charge-independence-breaking contact terms. Phys. Rev. C **103**(5), 055501 (2021). https://doi.org/10.1103/PhysRevC.103.055501. arXiv:2102.02184 [nucl-th]
119. L. Jokiniemi, P. Soriano, J. Menéndez, Impact of the leading-order short-range nuclear matrix element on the neutrinoless double-beta decay of medium-mass and heavy nuclei. Phys. Lett. B **823**, 136720 (2021). https://doi.org/10.1016/j.physletb.2021.136720. arXiv:2107.13354 [nucl-th]
120. J. Menendez, A. Poves, E. Caurier, F. Nowacki, The Occupancies of individual orbits and the nuclear matrix element of the Ge-76 neutrinoless beta beta decay. Phys. Rev. C **80**, 048501 (2009). https://doi.org/10.1103/PhysRevC.80.048501. arXiv:0906.0179 [nucl-th]
121. M. Horoi, A. Neacsu, Shell model predictions for ^{124}Sn double-β decay. Phys. Rev. C **93**(2), 024308 (2016). https://doi.org/10.1103/PhysRevC.93.024308. arXiv:1511.03711 [nucl-th]
122. Y. Iwata, N. Shimizu, T. Otsuka, Y. Utsuno, J. Menéndez, M. Honma, T. Abe, Large-scale shell-model analysis of the neutrinoless $\beta\beta$ decay of ^{48}Ca. Phys. Rev. Lett. **116**(11), 112502 (2016). https://doi.org/10.1103/PhysRevLett.117.179902. arXiv:1602.07822 [nucl-th]. [Erratum: Phys. Rev. Lett. 117, 179902 (2016)]
123. L. Coraggio, A. Gargano, N. Itaco, R. Mancino, F. Nowacki, Calculation of the neutrinoless double-β decay matrix element within the realistic shell model. Phys. Rev. C **101**(4), 044315 (2020). https://doi.org/10.1103/PhysRevC.101.044315. arXiv:2001.00890 [nucl-th]
124. L. Coraggio, N. Itaco, G. De Gregorio, A. Gargano, R. Mancino, F. Nowacki, Shell-model calculation of ^{100}Mo double-β decay. Phys. Rev. C **105**(3), 034312 (2022). https://doi.org/10.1103/PhysRevC.105.034312. arXiv:2203.01013 [nucl-th]
125. Y. Tsunoda, N. Shimizu, T. Otsuka, Shape transition of Nd and Sm isotopes and neutrinoless double-beta decay nuclear matrix element of ^{150}Nd, (2023) arXiv:2304.11780 [nucl-th]
126. J.M. Yao, J. Meng, Y.F. Niu, P. Ring, Beyond-mean-field approaches for nuclear neutrinoless double beta decay in the standard mechanism. Prog. Part. Nucl. Phys. **126**, 103965 (2022). https://doi.org/10.1016/j.ppnp.2022.103965. arXiv:2111.15543 [nucl-th]

127. J. Kotila, J. Barea, Occupation probabilities of single particle levels using the microscopic interacting boson model: application to some nuclei of interest in neutrinoless double-β decay. Phys. Rev. C **94**(3), 034320 (2016). https://doi.org/10.1103/PhysRevC.94.034320
128. P. Gimeno, L. Jokiniemi, J. Kotila, M. Ramalho, J. Suhonen, Ordinary muon capture on ^{136}Ba: comparative study using the shell model and pnQRPA. Universe **9**(6), 270 (2023). https://doi.org/10.3390/universe9060270
129. J.M. Yao, A. Belley, R. Wirth, T. Miyagi, C.G. Payne, S.R. Stroberg, H. Hergert, J.D. Holt, *Abinitio* benchmarks of neutrinoless double-β decay in light nuclei with a chiral Hamiltonian. Phys. Rev. C **103**(1), 014315 (2021). https://doi.org/10.1103/PhysRevC.103.014315. arXiv:2010.08609 [nucl-th]
130. S. Novario, P. Gysbers, J. Engel, G. Hagen, G.R. Jansen, T.D. Morris, P. Navrátil, T. Papenbrock, S. Quaglioni, Coupled-cluster calculations of neutrinoless double-β decay in ^{48}Ca. Phys. Rev. Lett. **126**(18), 182502 (2021). https://doi.org/10.1103/PhysRevLett.126.182502. arXiv:2008.09696 [nucl-th]
131. A. Belley, C.G. Payne, S.R. Stroberg, T. Miyagi, J.D. Holt, Ab initio neutrinoless double-beta decay matrix elements for ^{48}Ca, ^{76}Ge, and ^{82}Se. Phys. Rev. Lett. **126**(4), 042502 (2021). https://doi.org/10.1103/PhysRevLett.126.042502. arXiv:2008.06588 [nucl-th]
132. S.J. Freeman, J.P. Schiffer, Constraining the $0\nu2\beta$ matrix elements by nuclear structure observables. J. Phys. G **39**, 124004 (2012). https://doi.org/10.1088/0954-3899/39/12/124004. arXiv:1207.4290 [nucl-ex]
133. S.J. Freeman et al., Experimental study of the rearrangements of valence protons and neutrons amongst single-particle orbits during double-β decay in ^{100}Mo. Phys. Rev. C **96**(5), 054325 (2017). https://doi.org/10.1103/PhysRevC.96.054325. arXiv:1710.10817 [nucl-ex]
134. S.V. Szwec et al., Rearrangement of valence neutrons in the neutrinoless double-β decay of ^{136}Xe. Phys. Rev. C **94**(5), 054314 (2016). https://doi.org/10.1103/PhysRevC.94.054314. arXiv:1611.05107 [nucl-ex]
135. D. Frekers, M. Alanssari, Charge-exchange reactions and the quest for resolution. Eur. Phys. J. A **54**(10), 177 (2018). https://doi.org/10.1140/epja/i2018-12612-5
136. B.M. Rebeiro et al., Ba138(d,α) study of states in Cs136: implications for new physics searches with xenon detectors. Phys. Rev. Lett. **131**(5), 052501 (2023). https://doi.org/10.1103/PhysRevLett.131.052501. arXiv:2301.11371 [nucl-ex]
137. N. Shimizu, J. Menéndez, K. Yako, Double Gamow–Teller transitions and its relation to neutrinoless $\beta\beta$ decay. Phys. Rev. Lett. **120**(14), 142502 (2018). https://doi.org/10.1103/PhysRevLett.120.142502. arXiv:1709.01088 [nucl-th]
138. J.M. Yao, I. Ginnett, A. Belley, T. Miyagi, R. Wirth, S. Bogner, J. Engel, H. Hergert, J.D. Holt, S.R. Stroberg, Ab initio studies of the double-Gamow–Teller transition and its correlation with neutrinoless double-β decay. Phys. Rev. C **106**(1), 014315 (2022). https://doi.org/10.1103/PhysRevC.106.014315. arXiv:2204.12971 [nucl-th]
139. L. Jokiniemi, J. Menéndez, Correlations between neutrinoless double-β, double Gamow–Teller, and double-magnetic decays in the proton–neutron quasiparticle random-phase approximation framework. Phys. Rev. C **107**(4), 044316 (2023). https://doi.org/10.1103/PhysRevC.107.044316. arXiv:2302.05399 [nucl-th]
140. B. Romeo, J. Menéndez, C. Peña Garay, $\gamma\gamma$ decay as a probe of neutrinoless $\beta\beta$ decay nuclear matrix elements. Phys. Lett. B **827**, 136965 (2022). https://doi.org/10.1016/j.physletb.2022.136965. arXiv:2102.11101 [nucl-th]
141. L. Jokiniemi, B. Romeo, P. Soriano, J. Menéndez, Neutrinoless $\beta\beta$-decay nuclear matrix elements from two-neutrino $\beta\beta$-decay data. Phys. Rev. C **107**(4), 044305 (2023). https://doi.org/10.1103/PhysRevC.107.044305. arXiv:2207.05108 [nucl-th]
142. W.-T. Chou, E.K. Warburton, B.A. Brown, Gamow–Teller beta-decay rates for A <= 18 nuclei. Phys. Rev. C **47**, 163–177 (1993). https://doi.org/10.1103/PhysRevC.47.163
143. B.H. Wildenthal, M.S. Curtin, B.A. Brown, Predicted features of the beta decay of neutron-rich SD-shell nuclei. Phys. Rev. C **28**, 1343–1366 (1983). https://doi.org/10.1103/PhysRevC.28.1343
144. G. Martínez-Pinedo, A. Poves, E. Caurier, A.P. Zuker, Effective g_A in the pf shell. Phys. Rev. C **53**(6), 2602 (1996). https://doi.org/10.1103/PhysRevC.53.R2602. arXiv:nucl-th/9603039
145. E. Caurier, A.P. Zuker, A. Poves, A Full 0 h-bar omega description of the 2 neutrino beta beta decay of Ca-48. Phys. Lett. B **252**, 13–17 (1990). https://doi.org/10.1016/0370-2693(90)91071-I
146. A. Poves, R.P. Bahukutumbi, K. Langanke, P. Vogel, Double beta decay of Ca-48 revisited. Phys. Lett. B **361**, 1–4 (1995). https://doi.org/10.1016/0370-2693(95)01134-C

147. E.A. Coello Pérez, J. Menéndez, A. Schwenk, Two-neutrino double electron capture on ^{124}Xe based on an effective theory and the nuclear shell model. Phys. Lett. B **797**, 134885 (2019). https://doi.org/10.1016/j.physletb.2019.134885. arXiv:1809.04443 [nucl-th]
148. J. Barea, J. Kotila, F. Iachello, $0\nu\beta\beta$ and $2\nu\beta\beta$ nuclear matrix elements in the interacting boson model with isospin restoration. Phys. Rev. C **91**(3), 034304 (2015). https://doi.org/10.1103/PhysRevC.91.034304. arXiv:1506.08530 [nucl-th]
149. P. Pirinen, J. Suhonen, Systematic approach to β and $2\nu\beta\beta$ decays of mass $A = 100$–136 nuclei. Phys. Rev. C **91**(5), 054309 (2015). https://doi.org/10.1103/PhysRevC.91.054309
150. S. Pastore, A. Baroni, J. Carlson, S. Gandolfi, S.C. Pieper, R. Schiavilla, R.B. Wiringa, Quantum Monte Carlo calculations of weak transitions in $A = 6 - 10$ nuclei. Phys. Rev. C **97**(2), 022501 (2018). https://doi.org/10.1103/PhysRevC.97.022501. arXiv:1709.03592 [nucl-th]
151. G.B. King, L. Andreoli, S. Pastore, M. Piarulli, R. Schiavilla, R.B. Wiringa, J. Carlson, S. Gandolfi, Chiral effective field theory calculations of weak transitions in light nuclei. Phys. Rev. C **102**(2), 025501 (2020). https://doi.org/10.1103/PhysRevC.102.025501. arXiv:2004.05263 [nucl-th]
152. H. Hergert, A guided tour of *ab initio* nuclear many-body theory. Front. Phys. **8**, 379 (2020). https://doi.org/10.3389/fphy.2020.00379. arXiv:2008.05061 [nucl-th]
153. A. Ekström, C. Forssén, G. Hagen, G.R. Jansen, W. Jiang, T. Papenbrock, What is ab initio in nuclear theory? Front. Phys. **11**, 1129094 (2023). https://doi.org/10.3389/fphy.2023.1129094. arXiv:2212.11064 [nucl-th]
154. S. Pastore, J. Carlson, V. Cirigliano, W. Dekens, E. Mereghetti, R.B. Wiringa, Neutrinoless double-β decay matrix elements in light nuclei. Phys. Rev. C **97**(1), 014606 (2018). https://doi.org/10.1103/PhysRevC.97.014606. arXiv:1710.05026 [nucl-th]
155. R.A.M. Basili, J.M. Yao, J. Engel, H. Hergert, M. Lockner, P. Maris, J.P. Vary, Benchmark neutrinoless double-β decay matrix elements in a light nucleus. Phys. Rev. C **102**(1), 014302 (2020). https://doi.org/10.1103/PhysRevC.102.014302. arXiv:1909.06501 [nucl-th]
156. H. Hergert, S.K. Bogner, T.D. Morris, A. Schwenk, K. Tsukiyama, The in-medium similarity renormalization group: a novel ab initio method for nuclei. Phys. Rept. **621**, 165–222 (2016). https://doi.org/10.1016/j.physrep.2015.12.007. arXiv:1512.06956 [nucl-th]
157. S.R. Stroberg, S.K. Bogner, H. Hergert, J.D. Holt, Nonempirical interactions for the nuclear shell model: an update. Ann. Rev. Nucl. Part. Sci. **69**, 307–362 (2019). https://doi.org/10.1146/annurev-nucl-101917-021120. arXiv:1902.06154 [nucl-th]
158. G. Hagen, T. Papenbrock, M. Hjorth-Jensen, D.J. Dean, Coupled-cluster computations of atomic nuclei. Rept. Prog. Phys. **77**(9), 096302 (2014). https://doi.org/10.1088/0034-4885/77/9/096302. arXiv:1312.7872 [nucl-th]
159. T.R. Rodriguez, G. Martinez-Pinedo, Energy density functional study of nuclear matrix elements for neutrinoless $\beta\beta$ decay. Phys. Rev. Lett. **105**, 252503 (2010). https://doi.org/10.1103/PhysRevLett.105.252503. arXiv:1008.5260 [nucl-th]
160. N. López Vaquero, T.R. Rodríguez, J.L. Egido, Shape and pairing fluctuations effects on neutrinoless double beta decay nuclear matrix elements. Phys. Rev. Lett. **111**(14), 142501 (2013). https://doi.org/10.1103/PhysRevLett.111.142501. arXiv:1401.0650 [nucl-th]
161. J.M. Yao, L.S. Song, K. Hagino, P. Ring, J. Meng, Systematic study of nuclear matrix elements in neutrinoless double-β decay with a beyond-mean-field covariant density functional theory. Phys. Rev. C **91**(2), 024316 (2015). https://doi.org/10.1103/PhysRevC.91.024316. arXiv:1410.6326 [nucl-th]
162. F.F. Deppisch, L. Graf, F. Iachello, J. Kotila, Analysis of light neutrino exchange and short-range mechanisms in $0\nu\beta\beta$ decay. Phys. Rev. D **102**(9), 095016 (2020). https://doi.org/10.1103/PhysRevD.102.095016. arXiv:2009.10119 [hep-ph]
163. J. Hyvärinen, J. Suhonen, Nuclear matrix elements for $0\nu\beta\beta$ decays with light or heavy Majorana-neutrino exchange. Phys. Rev. C **91**(2), 024613 (2015). https://doi.org/10.1103/PhysRevC.91.024613
164. F. Šimkovic, A. Smetana, P. Vogel, $0\nu\beta\beta$ nuclear matrix elements, neutrino potentials and $SU(4)$ symmetry. Phys. Rev. C **98**(6), 064325 (2018). https://doi.org/10.1103/PhysRevC.98.064325. arXiv:1808.05016 [nucl-th]
165. M.T. Mustonen, J. Engel, Large-scale calculations of the double-β decay of ^{76}Ge, ^{130}Te, ^{136}Xe, and ^{150}Nd in the deformed self-consistent Skyrme quasiparticle random-phase approximation. Phys. Rev. C **87**(6), 064302 (2013). https://doi.org/10.1103/PhysRevC.87.064302. arXiv:1301.6997 [nucl-th]
166. D.-L. Fang, A. Faessler, F. Simkovic, $0\nu\beta\beta$ -decay nuclear matrix element for light and heavy neutrino mass mechanisms from deformed quasiparticle random-phase approximation calculations for ^{76}Ge,

^{82}Se, ^{130}Te, ^{136}Xe, and ^{150}Nd with isospin restoration. Phys. Rev. C **97**(4), 045503 (2018). https://doi.org/10.1103/PhysRevC.97.045503. arXiv:1803.09195 [nucl-th]

167. J. Terasaki, Many-body correlations of quasiparticle random-phase approximation in nuclear matrix elements of neutrinoless double-β decay. Phys. Rev. C **91**(3), 034318 (2015). https://doi.org/10.1103/PhysRevC.91.034318. arXiv:1408.1545 [nucl-th]
168. J. Terasaki, Y. Iwata, Isoscalar pairing interaction for the quasiparticle random-phase approximation approach to double-β and β decays. Phys. Rev. C **100**(3), 034325 (2019). https://doi.org/10.1103/PhysRevC.100.034325. arXiv:1901.05165 [nucl-th]
169. J. Terasaki, Strength of the isoscalar pairing interaction determined by a relation between double-charge change and double-pair transfer for double- β decay. Phys. Rev. C **102**(4), 044303 (2020). https://doi.org/10.1103/PhysRevC.102.044303. arXiv:2003.03542 [nucl-th]
170. J. Menéndez, Neutrinoless $\beta\beta$ decay mediated by the exchange of light and heavy neutrinos: the role of nuclear structure correlations. J. Phys. G **45**(1), 014003 (2018). https://doi.org/10.1088/1361-6471/aa9bd4. arXiv:1804.02105 [nucl-th]
171. M. Horoi, A. Neacsu, S. Stoica, Statistical analysis for the neutrinoless double-β-decay matrix element of Ca48. Phys. Rev. C **106**(5), 054302 (2022). https://doi.org/10.1103/PhysRevC.106.054302. arXiv:2203.10577 [nucl-th]
172. M. Horoi, A. Neacsu, S. Stoica, Predicting the neutrinoless double-β-decay matrix element of Xe136 using a statistical approach. Phys. Rev. C **107**(4), 045501 (2023). https://doi.org/10.1103/PhysRevC.107.045501. arXiv:2302.03664 [nucl-th]
173. R. Weiss, P. Soriano, A. Lovato, J. Menendez, R.B. Wiringa, Neutrinoless double-β decay: combining quantum Monte Carlo and the nuclear shell model with the generalized contact formalism. Phys. Rev. C **106**(6), 065501 (2022). https://doi.org/10.1103/PhysRevC.106.065501. arXiv:2112.08146 [nucl-th]
174. C. Brase, J. Menéndez, E.A. Coello Pérez, A. Schwenk, Neutrinoless double-β decay from an effective field theory for heavy nuclei. Phys. Rev. C **106**(3), 034309 (2022). https://doi.org/10.1103/PhysRevC.106.034309. arXiv:2108.11805 [nucl-th]
175. E. Caurier, G. Martinez-Pinedo, F. Nowacki, A. Poves, A.P. Zuker, The shell model as unified view of nuclear structure. Rev. Mod. Phys. **77**, 427–488 (2005). https://doi.org/10.1103/RevModPhys.77.427. arXiv:nucl-th/0402046
176. T. Otsuka, A. Gade, O. Sorlin, T. Suzuki, Y. Utsuno, Evolution of shell structure in exotic nuclei. Rev. Mod. Phys. **92**(1), 015002 (2020). https://doi.org/10.1103/RevModPhys.92.015002. arXiv:1805.06501 [nucl-th]
177. B.A. Brown, The nuclear shell model towards the drip lines. Prog. Part. Nucl. Phys. **47**, 517–599 (2001). https://doi.org/10.1016/S0146-6410(01)00159-4
178. R. Weiss, R. Cruz-Torres, N. Barnea, E. Piasetzky, O. Hen, The nuclear contacts and short range correlations in nuclei. Phys. Lett. B **780**, 211–215 (2018). https://doi.org/10.1016/j.physletb.2018.01.061. arXiv:1612.00923 [nucl-th]
179. F. Simkovic, A. Faessler, H. Muther, V. Rodin, M. Stauf, The 0 nu bb-decay nuclear matrix elements with self-consistent short-range correlations. Phys. Rev. C **79**, 055501 (2009). https://doi.org/10.1103/PhysRevC.79.055501. arXiv:0902.0331 [nucl-th]
180. N. Paar, D. Vretenar, E. Khan, G. Colo, Exotic modes of excitation in atomic nuclei far from stability. Rept. Prog. Phys. **70**, 691–794 (2007). https://doi.org/10.1088/0034-4885/70/5/R02. arXiv:nucl-th/0701081
181. L.M. Robledo, T.R. Rodríguez, R.R. Rodríguez-Guzmán, Mean field and beyond description of nuclear structure with the Gogny force: a review. J. Phys. G **46**(1), 013001 (2019). https://doi.org/10.1088/1361-6471/aadebd. arXiv:1807.02518 [nucl-th]
182. F. Iachello, A. Arima, *The Interacting Boson Model. Cambridge Monographs on Mathematical Physics* (Cambridge University Press, Cambridge, 2006). https://doi.org/10.1017/CBO9780511895517
183. E.A. Coello Pérez, J. Menéndez, A. Schwenk, Gamow–Teller and double-β decays of heavy nuclei within an effective theory. Phys. Rev. C **98**(4), 045501 (2018). https://doi.org/10.1103/PhysRevC.98.045501. arXiv:1708.06140 [nucl-th]
184. J.J. Gomez-Cadenas, J. Martin-Albo, M. Sorel, P. Ferrario, F. Monrabal, J. Munoz-Vidal, P. Novella, A. Poves, Sense and sensitivity of double beta decay experiments. JCAP **06**, 007 (2011). https://doi.org/10.1088/1475-7516/2011/06/007. arXiv:1010.5112 [hep-ex]

185. J. Menéndez, T.R. Rodríguez, G. Martínez-Pinedo, A. Poves, Correlations and neutrinoless $\beta\beta$ decay nuclear matrix elements of pf-shell nuclei. Phys. Rev. C **90**(2), 024311 (2014). https://doi.org/10.1103/PhysRevC.90.024311. arXiv:1401.0651 [nucl-th]
186. N. Hinohara, J. Engel, Proton–neutron pairing amplitude as a generator coordinate for double-beta decay. Phys. Rev. C **90**(3), 031301 (2014). https://doi.org/10.1103/PhysRevC.90.031301. arXiv:1406.0560 [nucl-th]
187. J. Menéndez, N. Hinohara, J. Engel, G. Martínez-Pinedo, T.R. Rodríguez, Testing the importance of collective correlations in neutrinoless $\beta\beta$ decay. Phys. Rev. C **93**(1), 014305 (2016). https://doi.org/10.1103/PhysRevC.93.014305. arXiv:1510.06824 [nucl-th]
188. A. Belley, T. Miyagi, S.R. Stroberg, J.D. Holt, Ab initio calculations of neutrinoless $\beta\beta$ decay refine neutrino mass limits (2023). arXiv:2307.15156 [nucl-th]
189. A. Belley et al., Ab initio uncertainty quantification of neutrinoless double-beta decay in ^{76}Ge (2023) arXiv:2308.15634 [nucl-th]
190. R. Wirth, J.M. Yao, H. Hergert, Ab initio calculation of the contact operator contribution in the standard mechanism for neutrinoless double beta decay. Phys. Rev. Lett. **127**(24), 242502 (2021). https://doi.org/10.1103/PhysRevLett.127.242502. arXiv:2105.05415 [nucl-th]
191. A. Nelson, E. Eitrheim, A. Knight, D. May, M. Mehrhoff, R. Shannon, R. Litman, W. Burnett, T. Forbes, M. Schultz, Understanding the radioactive ingrowth and decay of naturally occurring radioactive materials in the environment: an analysis of produced fluids from the Marcellus shale. Environm. Health Perspect. (2015). https://doi.org/10.1289/ehp.1408855
192. S.R. Elliott, H. Ejiri, Solar neutrinos as background to neutrinoless double-beta decay experiments. AIP Conf. Proc. **1894**(1), 020008 (2017). https://doi.org/10.1063/1.5007633. arXiv:1708.00927 [nucl-ex]
193. A. Ianni, Underground laboratories. SciPost Phys. Proc. **12**, 007 (2023). https://doi.org/10.21468/SciPostPhysProc.12.007
194. Z. Guo et al., Muon flux measurement at China Jinping Underground Laboratory. Chin. Phys. C **45**(2), 025001 (2021). https://doi.org/10.1088/1674-1137/abccae. arXiv:2007.15925 [physics.ins-det]
195. L. Baudis, J. Hall, K.T. Lesko, J.L. Orrell, Snowmass 2021 underground facilities and infrastructure overview topical report (2022). arXiv:2212.07037 [hep-ex]
196. J. Heise, The Sanford underground research facility. In: Snowmass 2021 (2022)
197. S. Umehara et al., Neutrino-less double-beta decay of Ca-48 studied by Ca F(2)(Eu) scintillators. Phys. Rev. C **78**, 058501 (2008). https://doi.org/10.1103/PhysRevC.78.058501. arXiv:0810.4746 [nucl-ex]
198. D.Q. Adams et al., New direct limit on neutrinoless double beta decay half-life of Te128 with CUORE. Phys. Rev. Lett. **129**(22), 222501 (2022). https://doi.org/10.1103/PhysRevLett.129.222501. arXiv:2205.03132 [nucl-ex]
199. E. Armengaud et al., New limit for neutrinoless double-beta decay of ^{100}Mo from the CUPID-Mo experiment. Phys. Rev. Lett. **126**(18), 181802 (2021). https://doi.org/10.1103/PhysRevLett.126.181802. arXiv:2011.13243 [nucl-ex]
200. N. Abgrall et al., The large enriched germanium experiment for neutrinoless $\beta\beta$ decay: LEGEND-1000 preconceptual design report (2021). arXiv:2107.11462 [physics.ins-det]
201. W.R. Armstrong et al., CUPID pre-CDR (2019). arXiv:1907.09376 [physics.ins-det]
202. A. Armatol et al., Toward CUPID-1T (2022) arXiv:2203.08386 [nucl-ex]
203. H.B. Kim et al., Status and performance of the AMoRE-I experiment on neutrinoless double beta decay. J. Low Temp. Phys. **209**(5–6), 962–970 (2022). https://doi.org/10.1007/s10909-022-02880-z. arXiv:2211.02825 [physics.ins-det]
204. G. Adhikari et al., nEXO: neutrinoless double beta decay search beyond 10^{28} year half-life sensitivity. J. Phys. G **49**(1), 015104 (2022). https://doi.org/10.1088/1361-6471/ac3631. arXiv:2106.16243 [nucl-ex]
205. J. Martín-Albo et al., Sensitivity of NEXT-100 to neutrinoless double beta decay. JHEP **05**, 159 (2016). https://doi.org/10.1007/JHEP05(2016)159. arXiv:1511.09246 [physics.ins-det]
206. C. Adams et al., Sensitivity of a tonne-scale NEXT detector for neutrinoless double beta decay searches. JHEP **2021**(08), 164 (2021). https://doi.org/10.1007/JHEP08(2021)164. arXiv:2005.06467 [physics.ins-det]
207. K. Ichimura, Recent results from KamLAND-Zen. PoS NOW2022, 067 (2023). https://doi.org/10.22323/1.421.0067
208. V. Albanese et al., The SNO+ experiment. JINST **16**(08), 08059 (2021). https://doi.org/10.1088/1748-0221/16/08/P08059. arXiv:2104.11687 [physics.ins-det]

209. E. Fiorini, A. Pullia, G. Bertolini, F. Cappellani, G. Restelli, A search for lepton nonconservation in double beta decay with a germanium detector. Phys. Lett. B **25**, 602–603 (1967). https://doi.org/10.1016/0370-2693(67)90127-X
210. E. Fiorini, A. Pullia, G. Bertolini, F. Cappellani, G. Restelli, An underground experiment on neutrinoless double beta-decay. Lett. Nuovo Cim. **3**, 149–152 (1970). https://doi.org/10.1007/BF02755836
211. H.V. Klapdor-Kleingrothaus et al., Latest results from the Heidelberg–Moscow double beta decay experiment. Eur. Phys. J. A **12**, 147–154 (2001). https://doi.org/10.1007/s100500170022. arXiv:hep-ph/0103062
212. H.V. Klapdor-Kleingrothaus, A. Dietz, H.L. Harney, I.V. Krivosheina, Evidence for neutrinoless double beta decay. Mod. Phys. Lett. A **16**, 2409–2420 (2001). https://doi.org/10.1142/S0217732301005825. arXiv:hep-ph/0201231
213. H.V. Klapdor-Kleingrothaus, I.V. Krivosheina, The evidence for the observation of 0nu beta beta decay: the identification of 0nu beta beta events from the full spectra. Mod. Phys. Lett. A **21**, 1547–1566 (2006). https://doi.org/10.1142/S0217732306020937
214. C.E. Aalseth et al., Comment on 'Evidence for neutrinoless double beta decay'. Mod. Phys. Lett. A **17**, 1475–1478 (2002). https://doi.org/10.1142/S0217732302007715. arXiv:hep-ex/0202018
215. C.E. Aalseth et al., The IGEX Ge-76 neutrinoless double beta decay experiment: prospects for next generation experiments. Phys. Rev. D **65**, 092007 (2002). https://doi.org/10.1103/PhysRevD.65.092007. arXiv:hep-ex/0202026
216. M. Willers, LEGEND-200: From Construction to Physics Data Taking. XVIII International Conference on Topics in Astoparticle and Underground Physics (TAUP2023) (2023). https://indico.cern.ch/event/1199289/contributions/5447116/
217. E. Fiorini, T.O. Niinikoski, Low temperature calorimetry for rare decays. Nucl. Instrum. Methods A **224**, 83 (1984). https://doi.org/10.1016/0167-5087(84)90449-6
218. E. Andreotti et al., 130Te Neutrinoless double-beta decay with CUORICINO. Astropart. Phys. **34**, 822–831 (2011). https://doi.org/10.1016/j.astropartphys.2011.02.002. arXiv:1012.3266 [nucl-ex]
219. S. Pirro, S. Capelli, M. Pavan, E. Previtali, J.W. Beeman, P. Gorla, Scintillating double beta decay bolometers. Phys. Atom. Nucl. **69**, 2109–2116 (2006). https://doi.org/10.1134/S1063778806120155. arXiv:nucl-ex/0510074
220. A. Zolotarova, Bolometric double beta decay experiments: review and prospects. Symmetry **13**(12), 2255 (2021). https://doi.org/10.3390/sym13122255
221. D. Poda, Scintillation in low-temperature particle detectors. MDPI Phys. **3**(3), 473–535 (2021). https://doi.org/10.3390/physics3030032
222. K. Alfonso et al., Optimization of the first CUPID detector module. Eur. Phys. J. C **82**(9), 810 (2022). https://doi.org/10.1140/epjc/s10052-022-10720-3. arXiv:2202.06279 [physics.ins-det]
223. L. Zanotti, E. Bellotti, O. Cremonesi, E. Fiorini, G. Gervasio, S. Ragazzi, L. Rossi, J. Szarka, P.P. Sverzellati, T. Tabarelli, The Milano experiment on double beta decay of Xe-136. J. Phys. G **17**, 231–241 (1991). https://doi.org/10.1088/0954-3899/17/S/025
224. R. Luscher et al., Search for beta beta decay in Xe-136: new results from the Gotthard experiment. Phys. Lett. B **434**, 407–414 (1998). https://doi.org/10.1016/S0370-2693(98)00906-X
225. J.C. Vuilleumier et al., Search for neutrinoless double beta decay in Xe-136 with a time projection chamber. Phys. Rev. D **48**, 1009–1020 (1993). https://doi.org/10.1103/PhysRevD.48.1009
226. J.B. Albert et al., Sensitivity and discovery potential of nEXO to neutrinoless double beta decay. Phys. Rev. C **97**(6), 065503 (2018). https://doi.org/10.1103/PhysRevC.97.065503. arXiv:1710.05075 [nucl-ex]
227. S.A. Kharusi et al. nEXO Pre-Conceptual Design Report (2018) arXiv:1805.11142 [physics.ins-det]
228. M. Kekic et al., Demonstration of background rejection using deep convolutional neural networks in the NEXT experiment. JHEP **01**, 189 (2021). https://doi.org/10.1007/JHEP01(2021)189. arXiv:2009.10783 [physics.ins-det]
229. D. Nygren, High-pressure xenon gas electroluminescent TPC for 0nu beta beta-decay search. Nucl. Instrum. Methods A **603**, 337–348 (2009). https://doi.org/10.1016/j.nima.2009.01.222
230. M.K. Moe, New approach to the detection of neutrinoless double beta decay. Phys. Rev. **C44**, 931–934 (1991). https://doi.org/10.1103/PhysRevC.44.931
231. C. Chambers et al., Imaging individual barium atoms in solid xenon for barium tagging in nEXO. Nature **569**(7755), 203–207 (2019). https://doi.org/10.1038/s41586-019-1169-4. arXiv:1806.10694 [physics.ins-det]

232. J.B. Albert et al., Measurements of the ion fraction and mobility of alpha- and beta-decay products in liquid xenon using the Exo-200 detector. Phys. Rev. C **92**, 045504 (2015). https://doi.org/10.1103/PhysRevC.92.045504
233. A. Bolotnikov, B. Ramsey, The spectroscopic properties of high-pressure xenon. Nucl. Instrum. Methods Phys. Res. A **396**, 360–370 (1997). https://doi.org/10.1016/S0168-9002(97)00784-5
234. D.R. Nygren, Detecting the barium daughter in ^{136}Xe 0-$\nu\beta\beta$ decay using single-molecule fluorescence imaging techniques. J. Phys.: Conf. Ser. **650**(1), 012002 (2015). https://doi.org/10.1088/1742-6596/650/1/012002
235. B.J.P. Jones, A.D. McDonald, D.R. Nygren, Single molecule fluorescence imaging as a technique for barium tagging in neutrinoless double beta decay. JINST **11**(12), 12011 (2016). https://doi.org/10.1088/1748-0221/11/12/P12011. arXiv:1609.04019
236. A.D. McDonald et al., Demonstration of single barium ion sensitivity for neutrinoless double beta decay using single molecule fluorescence imaging. Phys. Rev. Lett. **120**(13), 132504 (2018). https://doi.org/10.1103/PhysRevLett.120.132504. arXiv:1711.04782 [physics.ins-det]
237. I. Rivilla et al., Fluorescent bicolour sensor for low-background neutrinoless double β decay experiments. Nature **583**(7814), 48–54 (2020). https://doi.org/10.1038/s41586-020-2431-5
238. K. Eguchi et al., First results from KamLAND: evidence for reactor anti-neutrino disappearance. Phys. Rev. Lett. **90**, 021802 (2003). https://doi.org/10.1103/PhysRevLett.90.021802. arXiv:hep-ex/0212021
239. G. Alimonti et al., The Borexino detector at the Laboratori Nazionali del Gran Sasso. Nucl. Instrum. Methods A **600**, 568–593 (2009). https://doi.org/10.1016/j.nima.2008.11.076. arXiv:0806.2400 [physics.ins-det]
240. R.S. Raghavan, New approach to the search for neutrinoless double beta decay. Phys. Rev. Lett. **72**, 1411–1414 (1994). https://doi.org/10.1103/PhysRevLett.72.1411
241. A. Gando et al., Measurement of the double-β decay half-life of ^{136}Xe with the KamLAND-Zen experiment. Phys. Rev. C **85**, 045504 (2012). https://doi.org/10.1103/PhysRevC.85.045504. arXiv:1201.4664 [hep-ex]
242. A.S. Barabash, Double beta decay: historical review of 75 years of research. Phys. Atom. Nucl. **74**, 603–613 (2011). https://doi.org/10.1134/S1063778811030070. arXiv:1104.2714 [nucl-ex]
243. V.I. Tretyak, False starts in history of searches for 2β decay, or Discoverless double beta decay. AIP Conf. Proc. **1417**(1), 129–133 (2011). https://doi.org/10.1063/1.3671051. arXiv:1112.4183 [nucl-ex]

Authors and Affiliations

Juan José Gómez-Cadenas[1,2] · Justo Martín-Albo[3] · Javier Menéndez[4,5] · Mauro Mezzetto[6] · Francesc Monrabal[1,2] · Michel Sorel[3]

Justo Martín-Albo
justo.martin-albo@ific.uv.es

Javier Menéndez
menendez@fqa.ub.edu

Mauro Mezzetto
mauro.mezzetto@pd.infn.it

Francesc Monrabal
francesc.monrabal@dipc.org

Michel Sorel
sorel@ific.uv.es

[1] Donostia International Physics Center, ERC Basque Excellence Research Centre, 20018 San Sebastián/Donostia, Spain

[2] Ikerbasque (Basque Foundation for Science), 48009 Bilbao, Spain

[3] Instituto de Física Corpuscular (IFIC), CSIC & Universitat de València, 46980 Paterna, Spain
[4] Departament de Física Quàntica i Astrofísica, Universitat de Barcelona, 08028 Barcelona, Spain
[5] Institut de Ciències del Cosmos, Universitat de Barcelona, 08028 Barcelona, Spain
[6] Sezione di Padova, INFN, 35131 Padova, Italy